Interplay Of Charge, Orbital And Spin In Correlated Transition Metal Oxides

Thesis submitted for the degree of
Doctor of Philosophy (Science)

in

Physics (Theoretical)

by

Santu Baidya

Department of Physics
University of Calcutta
August 2014

To my Father and Mother

Acknowledgments

I take this opportunity to express my profound gratitude and deep regards to my supervisor (Professor Tanusri Saha-Dasgupta) for her exemplary guidance, monitoring and constant encouragement throughout the course of this thesis. Her help, affection and sometimes admonitions were mother-like, which gave me strength, understanding and comfortable atmosphere to work under her supervision, and thus the task of research work never turned sombre. The blessing and advice given by her time to time shall carry me a long way in the journey of life on which I am about to embark.

I would like to express my gratitude to all those people who made this dissertation possible. I would like to give my regards and express my gratitude to my seniors Hena di, Swastika di, Soumyajit da, Sudipta da, Swarnakaml da for their help during my research work in this group. I would like to express my heartiest respect to Hena di who always helped me as elder sister in this group. I would also like to express my regards to Swastika di who helped me to attain skill in presenting my work. I would also like to thank Soumyajit da for his cooperation in learning computational techniques. Also I thank Soumyajit da for giving me thesis latex package which helped me to write my thesis comfortably. Thanks Sudipta da for your friendship that has always given me pleasure. I would also like to express my pleasure for working with my new group-mates Kartik, Hrishid, Abir, Poulami, Dhani and would like to give them heartful wish for their future achievements. A special thank to Rajiv Chauhan ji and A.P. Jena ji for their help solving computer related problems which helped me to work on my computer comfortably. I also thank Prashant singh ji for valuable academic discussion.

It has been a comfortable and peaceful journey at S N Bose Centre which I shall remember forever due to love and respect from all my friends in the institute. I must thank my beloved friends Saikat, Bivas, Debasis, Bipul, Sumit, Kaloni for their friendship that I shall remember forever. I must thank Shinde for his friendship that has given me lots of *support* and *knowledge* both *inside and outside academics*. During my computational study I have faced problems in computation from many technical issues. I must thank our system administrator Abhijit Ghosh for providing me helpful support in solving problems regarding computation.

Who above all have always been with me are my mother and father. Their love has been giving me support and strength. If I am here completing my thesis is only because of their blessings and love. I must express my heart-felt gratitude to my parents, *meso*, *masi* and my sister.

Finally, I appreciate all support provided by S N Bose Centre during my Ph.D. and I would like to thank everybody who has contributed anyway in completing my thesis successfully.

Santu Baidya
Kolkata, India
August, 2014

List of Publications

1. **Santu Baidya**, Prabuddha Sanyal, Hena Das, Bertrand Roessli, Tapan Chatterji, and T. Saha-Dasgupta
   Understanding neutron scattering data in YMn_2O_5: An effective spin Hamiltonian
   Phys. Rev. B 84, 054444 (2011) ⋆

2. **Santu Baidya** and T. Saha-Dasgupta
   Electronic structure and phonons in La_2CoMnO_6: A ferromagnetic insulator driven by Coulomb-assisted spin-orbit coupling
   Phys. Rev. B 84, 035131 (2011) ⋆

3. **Santu Baidya** and T. Saha-Dasgupta
   Effect of A Cation on magnetic properties of double perovskite compounds: From ferromagnetic Ca_2CrSbO_6 to antiferromagnetic Sr_2CrSbO_6
   Phys. Rev. B 86, 024440 (2012) ⋆

4. **Santu Baidya**, Soumyajit Sarkar, T. Saha-Dasgupta, and D. D. Sarma
   Interplay of localized and itinerant character of Ru ions: $Tl_2Ru_2O_7$ vs. $Hg_2Ru_2O_7$
   Phys. Rev. B 86, 125117 (2012) ⋆

5. Olga Yakubovich, Galina Kiriukhina, Olga Dimitrova, Anatoli Volkov, Alexey Golovanov, Olga Volkova, Elena Zvereva, **Santu Baidya**, T. Saha-Dasgupta and Alexander Vasiliev
   Crystal structure and magnetic properties of new layered sodium nickel hydroxide phosphate, $Na_2Ni_3(OH)_2(PO_4)_2$
   Dalton Trans. 42, 14718-14725 (2013)

6. Larisa Shvanskaya, Olga Yakubovich, Anna Ivanova, **Santu Baidya**, Tanusri Saha-Dasgupta, Elena Zvereva, Alexey Golovanov, Olga Volkova and Alexander Vasiliev
   Copper rubidium diphosphate, $Rb_2Cu_3(P_2O_7)_2$: synthesis, crystal structure, thermodynamic and resonant properties
   New J. Chem., 37, 2743-2750 (2013)

Publications marked with ⋆ are reported in this thesis.

Contents

List of Figures

List of Tables

Chapter 1

Introduction

The term "oxide materials" is closely connected to "oxide ceramics" which represent a type of material used to decorate pottery. An oxide is a compound in which one of the component is oxygen. Due to the high electronegativity oxygen forms stable chemical bonds with almost all elements to form the corresponding oxides. Metal oxides containing anion oxygen and metal cation, are fascinating group of materials. In this thesis we have focused on studying transition metal oxides (TMO's). Transition metal oxides are those for which metal cations are transition metal cations, the d-block elements in periodic table, characterized by localized nature of d electrons and the associated strong correlation effect.

1.1 Transition metal oxides

TMO's have attracted attention of physicists and chemists due to their wide range of electronic, chemical and metallic properties. Strong correlation effect between TM d-electrons brings in novel and unusual aspect in these properties. Interplay between the charge, spin and orbital degrees of freedom of electrons together with strong correlation produces many

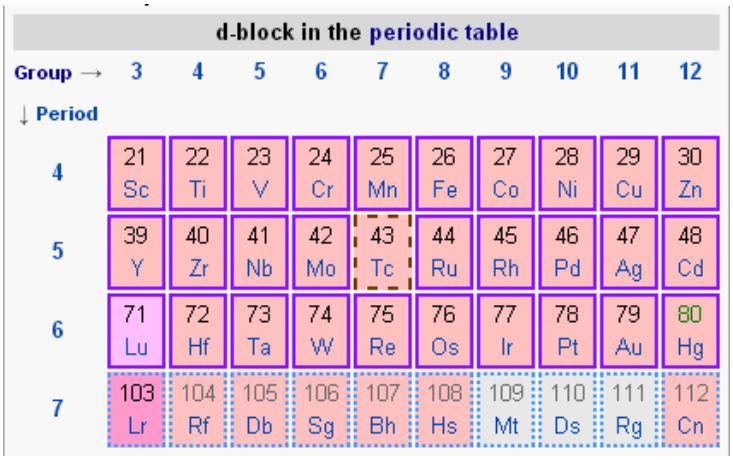

Figure 1.1 Periodic table with d-block elements only (taken from [1]).

complex phenomena like magnetic phase transitions, metal-insulator transition, large magnetoresistance, magnetodielectric effect, multiferroicity etc. In TMO's the Coulomb repulsion between d electrons tries to localize the TM d electrons at lattice sites and hybridization between TM d and oxygen p states tend to delocalize the electrons. The balance between the two makes transition metal-oxides (TMO's) excellent candidates with tunable electronic properties to arrive at a microscopic understanding of influence of various driving forces.

In the present thesis we have used first-principles based density functional theory (DFT) (*this will be discussed in the next chapter*) to study electronic structure of transition metal-oxides. In the first-principles based methods we need the information only about the crystal structure of the compound. Such a parameter free approach is capable of capturing the chemistry of compounds accurately. In this thesis we have studied a few examples in 3d and 4d -TMO's where interplay of spin, charge, orbital degrees of freedom together with correlation effect is found to give rise to interesting effects, e.g., (a) magnetism in a multiferroic spin compound YMn_2O_5, (b) interplay of correlation and spin-orbit coupling in a double perovskite compound La_2CoMnO_6, (c) contrasting magnetic behavior of double perovskite compounds Sr_2CrSbO_6 and Ca_2CrSbO_6, (d) metal-insulator transition in itinerant electron system $Hg_2Ru_2O_7$.

The first three examples belong to the class of 3d TMO's while the last one belongs to the class of 4d TMO's. In the following we briefly discuss the comparison between the 3d TMO's and 4d TMO's.

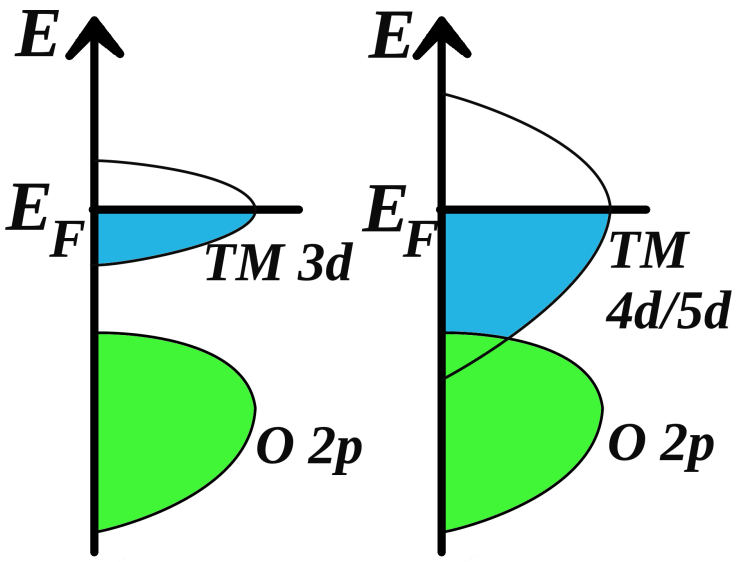

Figure 1.2 Schematic diagram to show comparison of shape of 3d and 4d/5d states in transition metal oxides. While TM 3d has narrow band TM 4d/5d has wider band in TMO's.

1.1.1 3d transition metal oxides

3d transition-metal oxides, like copper based high-temperature superconductors, manganites with colossal magnetoresistive properties, etc., are among the most intensely studied compounds in condensed matter physics [2, 3, 4, 5, 6, 7]. They exhibit a vast range of electrical and magnetic properties like insulating, semiconducting, metallic, superconducting, ferromagnetic, ferrimagnetic and antiferromagnetic [8]. The physical properties are found to be sensitive to the change in external conditions like temperature or pressure. The extend of 3d wavefunctions of TM ions is in general small, leading to small bandwidth of TM d domi-

Table 1.1 The list of various 3d transition metal oxides with various kinds of interesting magnetic and electric properties.

Properties	Compounds	References
Large gap insulators	NiO, $Bi_4Ti_3O_{12}$, La_2CuO_4, MnO	[9], [10], [11], [12]
Metals	V_2O_5, Ti_2O_3, Ba_2FeMoO_6, Sr_2FeMoO_6	[13], [14], [15], [16]
High-T_c superconductors	$YBa_2Cu_3O_7$, $La_{2-x}Sr_xCuO_4$	[17], [18]
Ferromagnetic	$YbTiO_3$, $HoTi_3$, $LaCaMnO_3$	[19], [20]
Antiferromagnetic	NiO, Cr_2O_3, $CaCo_3V_4O_{12}$	[21], [22], [23]
Multiferroics	$Ni_3V_2O_8$, $TbMnO_3$, $CoCr_2O_4$, $MnWO_4$	[24], [25], [26], [27]

nated states which is separated from the O p dominated states in case of compounds with large charge transfer, as shown in left side of Fig. 1.2. The physics is nominally dominated by three energy scales, the charge transfer energy Δ, which is the energy difference between metal d and O p states, the hopping connecting metal and O sites, t_{pd}, and electron-electron correlation within TM d manifold, U_{dd}. Examples of various 3d transition metal oxides with various different ground state properties are given in the table 1.1.

1.1.2 4d/5d transition metal oxides

In case of 4d or 5d TMO's the band widths of TM d states are much wider compared to that of 3d TMO's giving rise to a situation shown in right hand side of Fig. 1.2. The other important difference between 3d and 4d TMO's is the enhanced importance of spin-orbit coupling in 4d TMO's due to the presence of 4d series elements. Fascinating materials displaying new phenomena, including materials with potential technological applications, has recently into the focus of research due to the role of the spin-orbit interaction. In the spin-orbit interaction

there is coupling between the electron's intrinsic spin and its orbital angular momentum. Usually the spin-orbit interaction is taken as weak perturbation because its effect on the electronic properties of materials is minimal, but becomes important for heavy elements. The Hamiltonian describing the spin-orbit effect is written as [28]:

$$H_{SO} = \frac{Z\alpha^2}{2}\frac{1}{r^3}\hat{L}.\hat{S} \tag{1.1}$$

Using the simplified form of Eq.1.1 the expression for energy due to spin-orbit effect can be written as,

$$E_{SO} = \frac{Z^4}{2(137)^2 n^3}\frac{[j(j+1)-l(l+1)-s(s+1)]}{2l(l+1/2)(l+1)} \tag{1.2}$$

where 'Z' is atomic number and 'n' is the principal quantum number. j is total angular momentum quantum number, l is orbital angular momentum quantum number and s is spin angular momentum quantum number. Therefore the spin-orbit coupling effect is proportional to the atomic number but inversely proportional to principal quantum number. This indicates that spin orbit-coupling effect is larger for atoms that are further down a particular column of the periodic table. 4d or 5d transition-metal elements (heavier atoms) are therefore good candidate to show larger spin-orbit effect than 3d transition-metals. Spin-orbit interactions in 4d or 5d TMO's are comparable in strength to the other interactions that determines the electronic properties of matter. The resulting interaction out of competition between such equally strong interactions give rise to new emergent properties of materials in 4d or 5d TMO's. Also, 4d orbitals are more extended than 3d orbitals in TMO's. Therefore, correlation effect is expected to be less important in such systems. Several theoretical studies have introduced new phases of matter of 4d or 5d TMO's like topological insulators ($Pb_{1-x}Sn_xTe$)[29], Weyl semimetals ($Y_2Ir_2O_7$)[30], thermally driven metal-insulator transition[31], quantum spin Hall-effect (Na_2IrO_3)[32] etc. which are of academic as well as of technological interest.

1.2 Brief description of various classes of materials

In this thesis we have studied few transition-metal oxides which unravels the physics of interplay of spin, charge, orbital degrees of freedom of electrons in 3d and 4d transition-metal oxides. We have studied (i) a complex spin system with general formula AMn_2O_5 (A being any rare-earth cation) belonging to the class of multiferroic compounds, (ii) double perovskite oxides which are fascinating group of materials with many interesting and rich physics and (iii) pyrochlore compounds, the lattice of which provides frustration. In the following sections, we introduce various classes of materials studied in the thesis, in terms of their physical properties and general crystal structure.

1.2.1 Multiferroics

The interplay between electricity and magnetism has always fascinated scientists and engineers for centuries. The simultaneous presence of electric polarization and magnetization has been discovered in a class of materials, called multiferroics [33]. The materials show presence of both spontaneous magnetization and polarization. The word "ferroic" refers to a material that adopts a spontaneous, switchable internal alignment of either spins or electric dipole moment or strain. In case of ferromagnetic material there is alignment of spins that can be switched using external magnetic field. In case of ferroelectrics there is alignment of electric dipole moments that can be switched using external electric field. In case of ferroelastics there is alignment of strains that can be switched using external stress. Multiferroics are the materials where more than one ferroic ordering exist in one phase. Usually in multiferroics

both ferroelectricity and ferromagnetism coexist in one phase. The appealing aspect about multiferroics from technological point of view is that magnetization may be controlled by the conjugate field of electric polarization and electric polarization may be controlled by the conjugate field of magnetization, due to the coupling between magnetization and electric polarization, an effect known as "magnetoelectric effect". Multiferroic properties have been found in different classes of materials like, double perovskites (Lu_2MnCoO_6 [34], Bi_2FeMnO_6 [35], Bi_2FeCrO_6 [36]), spinels (FeV_2O_4 [37], CdV_2O_4 [38]), hexagonal perovskites $AMnO_3$ (A= Tb, Dy, Ho, Y)[[25, 39, 40, 41], AMn_2O_5 (A=Tb, Dy, Ho, Y) [[42], [43]]. The origin of magnetoelectric coupling in multiferroic compounds can be various, like, Dzyaloshinski-Moria (DM) interactions as a result of weak spin-orbit coupling effect [25]. The manganite multiferroic materials AMn_2O_5 (A=Y, Tb, Dy, Ho)[42] which will be the focus of our study, are reported to have magnetoelectric coupling mediated by superexchange interaction, rather than by spin-orbit interaction. For these compounds (AMn_2O_5), the magnetization is the primary order parameter while the electric polarization is secondary order parameter. Understanding of magnetism in these materials therefore forms a key role.

AMn_2O_5 compounds have orthorhombic unit cell. A general crystal structure of AMn_2O_5 compounds are shown in the figure 1.3. There are two inequivalent Mn ions with charge disproportionate situation: Mn with square pyramidal environment has oxidation state $3+$ and Mn with octahedral environment has oxidation state $4+$. The octahedra and square-pyramids are connected by corner shared oxygen atoms. The octahedra share edges to form chains along c axis. These materials have been studied since the 1960s because of their complex magnetic structures. Recently, the materials are found to show spontaneous electrical polarization, the onset of which occurs just below the antiferromagnetic (AFM) ordering temperature (T_N) [44, 45, 46, 47]. The magnitude of polarization is not as large as observed in typical ferroelectric materials. Interest comes with the observation that the polarization is coupled to the

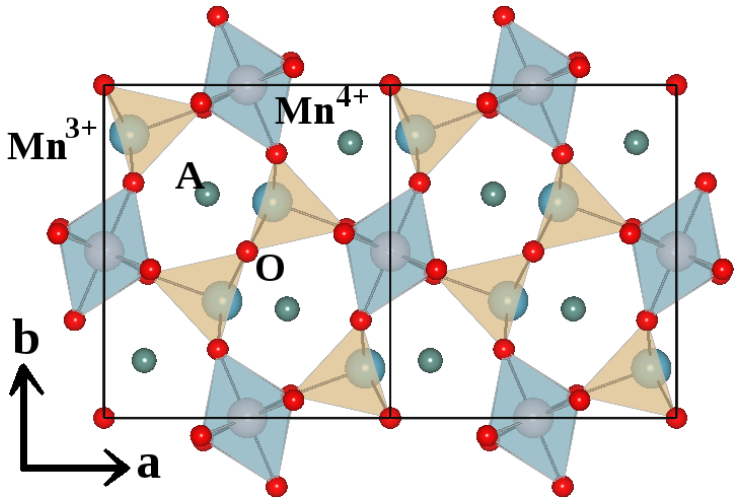

Figure 1.3 General AMn_2O_5 crystal structure with unit cell projected onto ab-plane. The octahedra $Mn^{4+}O_6$ share corner oxygens with $Mn^{3+}O_5$ square pyramid while two $Mn^{3+}O_5$ square pyramids are connected by edge-shared oxygen atoms.

magnetic order in these compounds. Furthermore, these compounds show several phase transitions upon lowering of temperature which is believed to be due to the magnetic frustration in the system. These compounds have been studied to understand the spin-phonon coupling effect [48], coefficient of magnetoelectric coupling [49] and dielectric permittivity [50]. The competing nature of magnetic interactions in these compounds give rise to commensurate and incommensurate magnetic ground states which are energetically comparable. Neutron diffraction study on these compounds revealed stabilization of complex magnetic structure like transverse spiral spin structure propagating along the c-axis [51].

1.2.2 Double Perovskites $AA'BB'O_6$

Perovskites have the general formula ABX_3 where A represents large electropositive ion, B represents small transition metal ion and X is either halide or oxygen ions. The double perovskites have unit cell twice that of the perovskite, with general formula $AA'BB'O_6$, where A, A′ may be similar or dissimilar ions and B, B′ are two transition metal ions. The large

size and valence mismatch between the B and B′ site cations can drive ordering of ions at B sublattice.

The crystallographic structure of a double perovskite compound is governed by the mismatch

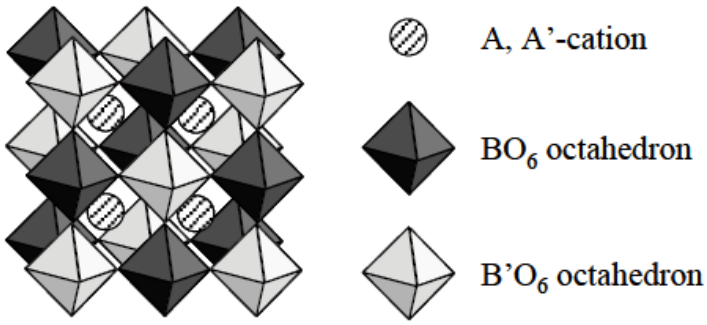

Figure 1.4 Ideal ordered cubic double perovskite structure $AA'BB'O_6$. A, A′ is any rare-earth or alkaline-earth ion and B, B′ are transition metal ions.

between the radius occupied by the A cation and the space left inside the oxygen interstices. Tolerance factor, f, as for perovskites, is used as a measure of such mismatch. The tolerance factor in case of double perovskites involves two possible distances B−O and B′−O, so

$$f \equiv \frac{r_A + r_O}{\sqrt{2}(\langle r_B \rangle + r_O)} \tag{1.3}$$

where r_i is the effective ionic radius of the i^{th} atom (A,B,B′,O), where '$\langle\rangle$' stands for the average of the r_i for B and B′ ions. In case of ordered arrangement of B and B′ ions typically rock-salt arrangement is observed, as shown in Fig. 1.4. It is an arrangement of corner-shared BO_6 and $B'O_6$ octahedra that contains A cations in 12 coordinated sites. However, ordered layered arrangement of B and B′ have been also observed [52]. For small valence and size difference between B and B′ , the arrangement at B sublattice becomes random.

Double perovskites have attracted recent attention due to the interesting properties offered by them. Many of the double perovskites are predicted to be "half-metals". Materials with high spin-polarization of the conducting charge carriers are of great interest for spintronics. An ideal material with 100% spin-polarization is called a half-metal. Interesting, the

Table 1.2 List of double perovskites with various electric and magnetic properties.

Properties	Compounds	References
Ferroelectric	$NaLaMnWO_6$ $CaMnTi_2O6$, Ho_2CuTiO_6, $PbBiZnNbO_6$	[60], [61], [62], [63]
Ferromagnetic	Sr_2FeMoO_6, Ca_2FeReO_6, Sr_2CrReO_6	[16], [64], [65]
Antiferromagnetic	Ba_2PrRuO_6, Ba_2MnWO_6	[66], [67]
Ferrimagnetic	Ba_2MnReO_6, Bi_2FeMoO_6, Bi_2MnMoO_6	[68], [69]
Multiferroic	Lu_2MnCoO_6, Bi_2FeCrO_6	[34], [36]
Superconductivity	Sr_2YRuO_6	[70]

double perovskite series offer half-metallic compounds with transition temperature above the room temperature, (Sr_2FeMoO_6 , Sr_2CrWO_6). Also the magnetodielctric effect [53] (La_2NiMnO_6)[54], colossal magnetoresistance [55] (La_2CoMnO_6 , Sr_2CoMoO_6)[56] etc. have been observed in double perovskite materials. Superconductivity in double perovskites ($Ba_2YRu_{1x}Cu_xO_6$ and $Sr_2YRu_{1x}Cu_xO_6$)[57] has been also reported. The double perovskites which are based on combinations of 3d-4d/5d transition metals are of special relevance to the presence of strong spin-orbit coupling effect, making them suitable for magneto-optic devices. Ir based double perovskite compounds have been studied for spin-orbit driven physical effects [58, 59]. A list of double perovskites with various electrical and magnetic properties is given in the Table1.2.

1.2.3 Pyrochlore compounds $A_2B_2O_6O'$

The $A_2B_2O_6O'$ pyrochlore structure is network of A-O′ and B-O bonds, where A site is occupied by rare earth element and B site may be occupied by 3d, 4d or 5d transition metal element. The O ions occupy two crystallographically nonequivalent positions. The larger

A cation has eight-fold coordination and smaller B cation has six-fold coordination(BO_6 octahedra). Pyrochlore compounds prefer A^{3+} B^{4+} cation combination and sometimes A^{2+} B^{5+} cation combination. Each of the A and B sites form a three dimensional network of corner-sharing tetrahedra. The pyrochlore structure can also be viewed as two isolated, but interpenetrating three-dimensional frameworks of A_2O' atoms and BO_6 octahedra, respectively. The compounds with (3+, 4+) cations ($Tl_2Ru_2O_7$[71], $Bi_2Ru_2O_7$[72]) are mostly reported while there exist compounds with (2+,5+) cations ($Hg_2Ru_2O_7$[73]). Recently (1+,6+) pyrochlore KOs_2O_6[74] have been also reported. This lattice shows geometrical frustration and novel magnetic effects. There are various physical properties found in pyrochlore compounds like electronic insulator $La_2Zr_2O_7$[75], ionic conductors, mixed ionic and electronic conductivity, spin ice system $Dy_2Ti_2O_7$[76], spin glass system $Y_2Mo_2O_7$[77], superconductivity $Cd_2Re_2O_7$[78].

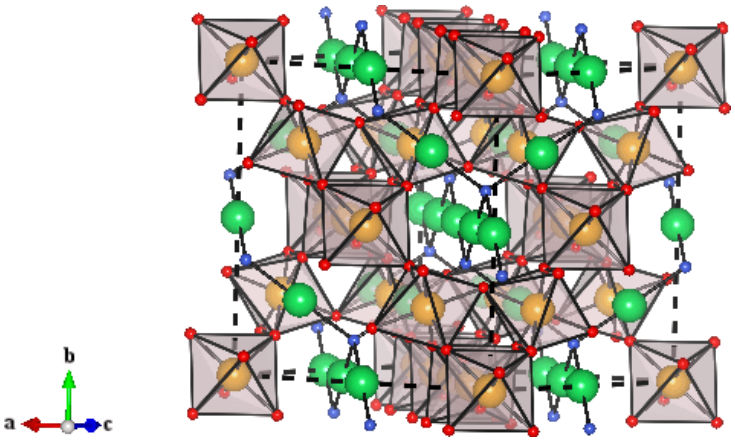

Figure 1.5 Unit cell of a Pyrochlore compound.

1.3 Overview of Present Thesis

From the above discussion it is clear that TMO's occurring in variety of crystal structures exhibit various interesting physical and chemical properties which need microscopic understanding. We have used first-principles based density functional theory to study such interesting properties in TMO's to achieve understanding at the microscopic level. With the advancement in the computational techniques as well computer hardware, first-principles based calculation has become key tool to understand the basic physics of real materials.

In the present thesis we have studied different classes of materials with different interesting properties of TMO's resulting from the interplay of charge, spin and orbital degrees of freedom as well as the correlation effect of TM d electrons. The brief summary of the contents of the various chapters are presented in the following.

Chapter 2 : In this chapter we discuss the theoretical methods which are used in this thesis. This includes brief description of the formulation of first-principles based density functional theory (DFT). Also, we discuss various basis sets to solve the eigenvalue problem posed by DFT. We discuss the beyond DFT correlation effect correction. We also discuss the first-principles based methods to study lattice dynamics such as Density functional perturbation theory (DFPT).

Chapter 3 : In this chapter we present our study on magnetic exchange interactions in a complex spin system, a multiferroic compound (YMn_2O_5). Magnetism is the key player in the compound that drives the ferroelectricity. By the construction of effective spin-Hamiltonian we could successfully reproduce the measured magnon dispersion data. Exact diagonalization method is used to solve the effective spin-Hamiltonian. The magnetic exchange interactions were calculated from information of effective Mn-Mn hopping integrals and energy differences as obtained from first-principles based wannier function description of the Mn d bands. Our study shows the importance of few magnetic exchange interactions in the magnetism of

YMn_2O_5 which were neglected previously.

Chapter 4 : In this chapter, we discuss a double perovskite compound La_2CoMnO_6 which shows unusual insulating state driven by Coulomb assisted spin-orbit coupling. Without correlation and spin-orbit interaction the compound is a metal which is in contradiction with the observed ground state. Our study shows that spin-orbit interaction with the help of Coulomb correlation makes the insulating state possible in this compound. Another important point of this compound is the magnetodielectric effect. We studied the magnetodielectric effect using first-principles based method which uncovered evidence of spin-phonon coupling in the compound.

Chapter 5 : In this chapter, we study the effect of non-magnetic A cation in the magnetism of two double perovskite compounds Sr_2CrSbO_6 and Ca_2CrSbO_6. This study gives rise to unusual concept that a non-magnetic A cation (Sr or Ca) may play an important role in the magnetism of a TMO system. We also studied the origin of stabilization of antiferromagnetism in the frustrated face centered cubic (FCC) lattice of Cr in the Sr_2CrSbO_6 compound.

Chapter 6 : In this chapter, we study the Ru d electron based ruthenate pyrocholre compound $Hg_2Ru_2O_7$ which is similar in crystal structure and magnetic behavior to another ruthenate pyrocholre compound $Tl_2Ru_2O_7$. Both compounds show metal to insulator transition upon lowering of temperature. Our study reveals the contrasting localized and itinerant behavior of Ru 4d electrons in $Tl_2Ru_2O_7$ and $Hg_2Ru_2O_7$, respectively. We provided explanation behind this contrasting behavior which turned out to be differential covalency between Hg-Ru and Tl-Ru. We also studied the insulating state in low temperature phase of $Hg_2Ru_2O_7$.

Bibliography

[1] The image of d-block of the periodic table is taken from "https://www.boundless.com/chemistry/periodic-properties/the-history-of-the-periodic-table/transition-metals" .

[2] J. Rowell, Print edition 44 (1991).

[3] P. W. Anderson, Science 256 (1992).

[4] W. E. Pickett, Rev. Mod. Phys. **61,** 433–512 (1989).

[5] W. E. Pickett, H. Krakauer, R. Cohen, and D. Singh, Science 255 (1992).

[6] J. G. Bednorz and K. A. Müller, Rev. Mod. Phys. **60,** 585–600 (1988).

[7] P. Lindberg, Z.-X. Shen, W. Spicer, and I. Lindau, Surf. Sci. Rep. 11 (1990).

[8] *Earlier and Recent Aspects of Superconductivity*, K. Schwarz, ed., (Springer, 1990).

[9] I. G. Austin and N. F. Mott, Science **168,** 71–77 (1970).

[10] A. V. Postnikov, S. Bartkowski, F. Mersch, M. Neumann, E. Z. Kurmaev, V. M. Cherkashenko, S. N. Nemnonov, and V. R. Galakhov, Phys. Rev. B **52,** 11805–11812 (1995).

[11] H. Das and T. Saha-Dasgupta, Phys. Rev. B **79,** 134522 (2009).

[12] J. van Elp, R. H. Potze, H. Eskes, R. Berger, and G. A. Sawatzky, Phys. Rev. B **44,** 1530–1537 (1991).

[13] V. Eyert and K.-H. Höck, Phys. Rev. B **57,** 12727–12737 (1998).

[14] Y. Guo, S. J. Clark, and J. Robertson, Journal of Physics: Condensed Matter **24,** 325504 (2012).

[15] J.-S. Kang, H. Han, B. W. Lee, C. G. Olson, S. W. Han, K. H. Kim, J. I. Jeong, J. H. Park, and B. I. Min, Phys. Rev. B **64,** 024429 (2001).

[16] M. Moreno, J. Gayone, M. Abbate, A. Caneiro, D. Niebieskikwiat, R. SÃąnchez, A. de Siervo, R. Landers, and G. Zampieri, Physica B: Condensed Matter **320,** 43 – 46 (2002), proceedings of the Fifth Latin American Workshop on Magnetism, Magnetic Materials and their Applications.

[17] S. Massidda, J. Yu, A. Freeman, and D. Koelling, Physics Letters A **122,** 198 – 202 (1987).

[18] K. Okada, Journal of the Physical Society of Japan **78,** 034725 (2009).

[19] Y. Su, Y. Sui, J.-G. Cheng, J.-S. Zhou, X. Wang, Y. Wang, and J. B. Goodenough, Phys. Rev. B **87,** 195102 (2013).

[20] M.-H. Phan, V. Srinivas, S.-C. Yu, and N. H. Hur, Journal of Applied Physics 93 (2003).

[21] J. C. Loudon, Phys. Rev. Lett. **109,** 267204 (2012).

[22] B. N. Brockhouse, The Journal of Chemical Physics 21 (1953).

[23] S. V. Ovsyannikov, Y. G. Zainulin, N. I. Kadyrova, A. P. Tyutyunnik, A. S. Semenova, D. Kasinathan, A. A. Tsirlin, N. Miyajima, and A. E. Karkin, Inorganic Chemistry **52,** 11703–11710 (2013).

[24] I. Cabrera *et al.*, Phys. Rev. Lett. **103,** 087201 (2009).

[25] M. Staruch, D. Violette, and M. Jain, Materials Chemistry and Physics **139,** 897 – 900 (2013).

[26] I. Kim, Y. S. Oh, Y. Liu, S. H. Chun, J.-S. Lee, K.-T. Ko, J.-H. Park, J.-H. Chung, and K. H. Kim, Applied Physics Letters **94,** – (2009).

[27] O. Heyer, N. Hollmann, I. Klassen, S. Jodlauk, L. BohatÃ¡, P. Becker, J. A. Mydosh, T. Lorenz, and D. Khomskii, Journal of Physics: Condensed Matter **18,** L471 (2006).

[28] "Information are taken from North Carolina State University website,", `http://www4.ncsu.edu/~franzen/public_html/CH331/help/so/so.html`.

[29] S.-Y. Xu *et al.*, Nat. Commun. 3 (2012).

[30] X. Wan, A. M. Turner, A. Vishwanath, and S. Y. Savrasov, Phys. Rev. B **83,** 205101 (2011).

[31] I. C. Fulga, A. R. Akhmerov, J. Tworzydło, B. Béri, and C. W. J. Beenakker, Phys. Rev. B **86,** 054505 (2012).

[32] A. Shitade, H. Katsura, J. Kuneš, X.-L. Qi, S.-C. Zhang, and N. Nagaosa, Phys. Rev. Lett. **102,** 256403 (2009).

[33] N. a. Spaldin, S.-w. Cheong, and R. Ramesh, Physics Today **63,** 38 (2010).

[34] S. Yáñez Vilar *et al.*, Phys. Rev. B **84,** 134427 (2011).

[35] Y. Du, Z. X. Cheng, S. X. Dou, X. L. Wang, H. Y. Zhao, and H. Kimura, Applied Physics Letters **97,** – (2010).

[36] L. Sha, J. Miao, S. Wu, X. Xu, Y. Jiang, and L. Qiao, Journal of Alloys and Compounds **554,** 299 – 303 (2013).

[37] G. J. MacDougall, V. O. Garlea, A. A. Aczel, H. D. Zhou, and S. E. Nagler, Phys. Rev. B **86,** 060414 (2012).

[38] G. Giovannetti *et al.*, Phys. Rev. B **83,** 060402 (2011).

[39] C. Lu, S. Dong, Z. Xia, H. Luo, Z. Yan, H. Wang, Z. Tian, S. Yuan, T. Wu, and J. Liu, Sci. Rep. 3 (2013).

[40] P. Rout, S. Pradhan, S. Das, and B. Roul, Physica B: Condensed Matter **407,** 2072 – 2077 (2012).

[41] M. Nakamura, Y. Tokunaga, M. Kawasaki, and Y. Tokura, Applied Physics Letters **98,** – (2011).

[42] A. B. Sushkov, M. Mostovoy, R. V. Aguilar, S.-W. Cheong, and H. D. Drew, Journal of Physics: Condensed Matter **20,** 434210 (2008).

[43] Z. Chen *et al.*, Frontiers of Physics **7,** 429–434 (2012).

[44] I. Kagomiya, K. Kohn, and T. Uchiyama, Ferroelectrics **280,** 131–143 (2002).

[45] A. Inomata and K. Kohn, Journal of Physics: Condensed Matter **8,** 2673 (1996).

[46] S. Kobayashi, T. Osawa, H. Kimura, Y. Noda, I. Kagomiya, and K. Kohn, Journal of the Physical Society of Japan **73,** 1031–1035 (2004).

[47] S. Kobayashi, T. Osawa, H. Kimura, Y. Noda, I. Kagomiya, and K. Kohn, Journal of the Physical Society of Japan **73,** 1593–1596 (2004).

[48] S. Bahoosh, J. Wesselinowa, and S. Trimper, The European Physical Journal B 86 (2013).

[49] A. Sukhov, P. P. Horley, C.-L. Jia, and J. Berakdar, Journal of Applied Physics **113,** – (2013).

[50] A. B. Sushkov, R. V. Aguilar, S. Park, S.-W. Cheong, and H. D. Drew, Phys. Rev. Lett. **98,** 027202 (2007).

[51] H. Kimura, S. Kobayashi, Y. Fukuda, T. Osawa, Y. Kamada, Y. Noda, I. Kagomiya, and K. Kohn, Journal of the Physical Society of Japan **76,** 074706 (2007).

[52] M. T. Anderson, K. B. Greenwood, G. A. Taylor, and K. R. Poeppelmeier, Prog. Solid St. Chem. **22,** 197–233 (1993).

[53] P. Padhan, H. Z. Guo, P. LeClair, and A. Gupta, Applied Physics Letters **92,** – (2008).

[54] P. Padhan, P. LeClair, A. Gupta, M. A. Subramanian, and G. Srinivasan, Journal of Physics: Condensed Matter **21,** 306004 (2009).

[55] A. Georges, G. Kotliar, W. Krauth, and M. J. Rozenberg, Rev. Mod. Phys. **68,** 13–125 (1996).

[56] R. N. Mahato, K. Sethupathi, and V. Sankaranarayanan, Journal of Applied Physics 107 (2010).

[57] S. Rao, J. Srivastava, H. Tang, D. Ling, C. Chung, J. Yang, S. Sheen, and M. Wu, Journal of crystal growth **235,** 271–276 (2002).

[58] G. Chen and L. Balents, Phys. Rev. B **78,** 094403 (2008).

[59] G. Jackeli and G. Khaliullin, Phys. Rev. Lett. **102,** 017205 (2009).

[60] T. Fukushima, A. Stroppa, S. Picozzi, and J. M. Perez-Mato, Phys. Chem. Chem. Phys. **13,** 12186–12190 (2011).

[61] A. Aimi, D. Mori, K.-i. Hiraki, T. Takahashi, Y. J. Shan, Y. Shirako, J. Zhou, and Y. Inaguma, Chemistry of Materials **26,** 2601–2608 (2014).

[62] S. B. Reddy, K. M. Kant, K. P. Rao, M. Opel, R. Gross, and M. R. Rao, Journal of Magnetism and Magnetic Materials **303,** e332 – e334 (2006), the 6th International Symposium on Physics of Magnetic Materials The 6th International Symposium on Physics of Magnetic Materials.

[63] B. K. Choudhary, A. K. Himanshu, U. Kumar, S. K. Bandyopadhayay, P. Sen, S. N. Singh, and T. P. Sinha, AIP Conference Proceedings 1512 (2013).

[64] W. Westerburg, O. Lang, C. Ritter, C. Felser, W. Tremel, and G. Jakob, Solid State Communications **122,** 201 – 206 (2002).

[65] H. Kato, T. Okuda, Y. Okimoto, Y. Tomioka, Y. Takenoya, A. Ohkubo, M. Kawasaki, and Y. Tokura, Applied Physics Letters 81 (2002).

[66] Y. Izumiyama, Y. Doi, M. Wakeshima, Y. Hinatsu, Y. Shimojo, and Y. Morii, Journal of Physics: Condensed Matter **13,** 1303 (2001).

[67] C. Khattak, D. Cox, and F. Wang, Journal of Solid State Chemistry **17,** 323 – 325 (1976).

[68] C. Khattak, D. Cox, and F. Wang, Journal of Solid State Chemistry **13,** 77 – 83 (1975).

[69] S.-D. Li, P. Chen, and B.-G. Liu, AIP Advances **3,** – (2013).

[70] P. Battle and W. Macklin, Journal of Solid State Chemistry **52,** 138 – 145 (1984).

[71] S. Lee *et al.*, Nat. Mater. **5,** 471–476 (2006).

[72] M. Tachibana, Y. Kohama, T. Shimoyama, A. Harada, T. Taniyama, M. Itoh, H. Kawaji, and T. Atake, Phys. Rev. B **73,** 193107 (2006).

[73] W. Klein, R. K. Kremer, and M. Jansen, J. Mater. Chem. **17,** 1356–1360 (2007).

[74] J.-I. Yamaura, S. Yonezawa, Y. Muraoka, and Z. Hiroi, Journal of Solid State Chemistry **179,** 336–340 (2006).

[75] B. Liu, J. Wang, Y. Zhou, T. Liao, and F. Li, Acta Materialia **55,** 2949–2957 (2007).

[76] C. Z. Bi, J. Y. Ma, B. R. Zhao, Z. Tang, D. Yin, C. Z. Li, D. Z. Yao, J. Shi, and X. G. Qiu, Journal of Physics: Condensed Matter **17,** 5225 (2005).

[77] M. Hanawa, Y. Muraoka, T. Tayama, T. Sakakibara, J. Yamaura, and Z. Hiroi, Phys. Rev. Lett. **87,** 187001 (2001).

[78] H. Sakai, K. Yoshimura, H. Ohno, H. Kato, S. Kambe, R. E. Walstedt, T. D. Matsuda, Y. Haga, and Y. Onuki, Journal of Physics: Condensed Matter **13,** L785 (2001).

Chapter 2

Theoretical Background of Electronic Structure Calculations

This chapter deals with the theoretical background of the computational methods used to study various properties of crystalline materials discussed in this thesis.

2.1 Methods of Electronic Structure Calculation

2.1.1 Many-Body Hamiltonian

The behavior of real materials is determined by the fundamental particles - electrons and nuclei. Many of the properties, for example, optical and magnetic properties of materials are determined by the electrons, which makes their study important. The theoretical understanding of the electronic structure of matter is based on the quantum mechanics. So we can start with the many-body Hamiltonian $\hat{H}$ of the system which can be solved to obtain the solutions which give various properties of the material. The most general form of the Hamiltonian of the system of N_e electrons and N_P nuclei (neglecting relativistic effect, magnetic field, and

quantum electrodynamics for simplicity) is given by,

$$\hat{H} = -\frac{\hbar^2}{2m_e}\sum_{i=1}^{N_e}\nabla^2_{\mathbf{r_i}} - \sum_{I=1}^{N_P}\frac{\hbar^2}{2M_I}\nabla^2_{\mathbf{R_I}} - \frac{1}{4\pi\varepsilon_0}\sum_{i,I=1}\frac{Z_I e^2}{|\mathbf{R_I}-\mathbf{r_i}|} + \frac{1}{2}\frac{1}{4\pi\varepsilon_0}\sum_{i>j}\frac{e^2}{|\mathbf{r_i}-\mathbf{r_j}|} + \frac{1}{4\pi\varepsilon_0}\sum_{I>J}\frac{Z_I Z_J e^2}{|\mathbf{R_I}-\mathbf{R_J}|} \tag{2.1}$$

where m_e is the mass of an electron at $\mathbf{r_i}$ and M_I the mass of I^{th} ion at position $\mathbf{R_I}$. Z is the atomic number of an ion. Summation over i, j runs over electrons whereas summation over I,J runs over nuclei of the system.

First term in the Eq.(2.1) is the kinetic energy term which is sum of kinetic energies of individual electrons (e.g.,ith electron at $\mathbf{r_i}$), second term is sum of kinetic energies of individual nuclei (e.g., Ith nucleus at $\mathbf{R_I}$). The fourth term represents potential energy term due to repulsive coulomb interaction among electrons (the factor $\frac{1}{2}$ is included so that every interaction is considered only once) while fourth term is potential energy term due to repulsive coulomb interaction between nuclei. The third term represents potential energy due to attractive coulomb interaction between negatively charged electrons and positively charged nuclei.

2.1.2 Born-Oppenheimer Approximation

Finding exact solution for the Hamiltonian Eq.(2.1) is difficult due to large number of degrees of freedom involved and also coupled nature of various interacting terms. The first important approximation in simplifying the many-body problem is *Born-Oppenheimer approximation* [1]. As the mass M_I of the nuclei are much greater than the mass m_e of electrons, nuclei move much slower compared to electrons and electrons can be considered to be moving in the field of nuclei which are apparently frozen with respect to the time scale of electrons. This approximation is known as *Adiabatic approximation* or *Born-Oppenheimer approximation*. Within

this approximation the second term in Eq.(2.1),kinetic energy of the nuclei, can be neglected (due to the factor $\frac{1}{M_I}$) and the last term in Eq.(2.1), the coulomb repulsion between nuclei, can be taken as a constant. So the remaining terms in the Hamiltonian $\hat{H}$ are electronic terms describing the motion of N_e electrons in the field of N_p nuclei. The resultant electronic Hamiltonian is given by,

$$\hat{H} = -\frac{\hbar^2}{2m_e}\sum_{i=1}^{N_e}\nabla^2_{\mathbf{r_i}} - \frac{1}{4\pi\varepsilon_0}\sum_{i,I=1}\frac{Z_I e^2}{|\mathbf{R_I}-\mathbf{r_i}|} + \frac{1}{2}\frac{1}{4\pi\varepsilon_0}\sum_{i>j}\frac{e^2}{|\mathbf{r_i}-\mathbf{r_j}|} + E_{Madelung} \tag{2.2}$$

Where $E_{Madelung}$ is the constant potential energy term coming from ion-ion interaction.

Even with this simplification solving the eigenvalue problem for the Hamiltonian $\hat{H}$ is an extremely difficult task due to the exchange and correlation among electrons. If two electrons with same spin interchange positions, the wave function $\psi(\mathbf{r_i})$ must change sign. This property is called "exchange". Furthermore, each electron is affected by the motion of other electron which is known as "correlation" property. To solve the many-body systems with complicated interactions among electrons, the next crucial approximation is the single electron approximation where electrons are considered as independent particles moving in the mean field created by the other electrons and the nuclei. The systems where effect of exchange and correlation plays important role such as high T_c superconductors etc. are not suitable to be described by single-particle picture.

The single electron problem can be attacked with two possible approaches, (a) wave function based approach and (b) density based approach.

2.1.3 Single-Electron Picture

2.1.3.1 Wave Function Based Approach

Wave functions based method can be divided into two category; (a) semi-empirical method and (b) ab initio method. In case of ab initio method two basic approaches are considered; (a) "Hartree method" and (b)"Hartree-Fock method".

In Hartree approximation [2, 3, 4] each electron's motion is described by single-electron orbital which does not depend on the instantaneous motion of the other electrons. Assuming that electrons ignore each other the wave function Ψ_{HP} of the system can be written as

$$\Psi_{HP}(\mathbf{r_1}, \mathbf{r_2}, \mathbf{r_3}, ..., \mathbf{r_{N_e}}) = \psi(\mathbf{r_1})\psi(\mathbf{r_2})\psi(\mathbf{r_3})...\psi(\mathbf{r_{N_e}}) \tag{2.3}$$

which is known as *Hartree product* wavefunction with $\psi(\mathbf{r_i})$ being the one-electron wave functions. Hartree approach leads to the one-electron Schrödinger equation for $\psi(\mathbf{r_i})$

$$\left[-\frac{\hbar^2}{2m_e}\nabla^2 + v(\mathbf{r}) + e^2 \sum_{j=1, j\neq i}^{N_e} \int \frac{|\psi_j(\mathbf{r}')|^2}{|\mathbf{r} - \mathbf{r}'|} d\mathbf{r}' \right] \psi_i(\mathbf{r}) = E_i \psi_i(\mathbf{r}) \tag{2.4}$$

For an atom the potential $v(\mathbf{r}) = -\frac{Z}{r}$, where Z is the nuclear charge. In *Hartree approximation* an electron in i^{th} state is under the action of self-consistent field of all other electrons but i^{th} electron.

Although *Hartree approximation* works well for many systems but it has few shortcomings; (a) the total wave-function violates the Pauli exclusion principle, and (b) since the self-consistent potential acting on i^{th} electron depends on $\mathbf{r_i}$, the functions $\psi_i(\mathbf{r_i})$ are non-orthogonal. These shortcomings are eliminated by *Hartree-Fock approximation* [5] where total wave-function is constructed as an *antisymmetrized* (A) product,

$$\Psi_{HF}(\mathbf{r_1}, \mathbf{r_2}, \mathbf{r_3}, ..., \mathbf{r_{N_e}}) = A \prod_{j=1}^{N_e} \psi_i(\mathbf{r_i}) \tag{2.5}$$

which automatically satisfies the *Pauli exclusion principle*. The wave-function can be rewritten in determinant format known as *Slater determinant*,

$$\Psi_{HF}(\mathbf{r_1},\mathbf{r_2},\mathbf{r_3},...,\mathbf{r_{N_e}}) = \frac{1}{\sqrt{N_e!}} \begin{vmatrix} \psi_1(\mathbf{r_1}) & \psi_1(\mathbf{r_2}) & \cdots & \psi_1(\mathbf{r_{N_e}}) \\ \psi_2(\mathbf{r_1}) & \psi_2(\mathbf{r_2}) & \cdots & \psi_2(\mathbf{r_{N_e}}) \\ \vdots & \vdots & \ddots & \vdots \\ \psi_{N_e}(\mathbf{r_1}) & \psi_{N_e}(\mathbf{r_2}) & \cdots & \psi_{N_e}(\mathbf{r_{N_e}}) \end{vmatrix} \tag{2.6}$$

With the variational principle and antisymmetrized wave-function given by Eq.(2.6) resulting *Hartree-Fock* (HF) equations are given by,

$$\hat{H}^{HF}\psi_i(\mathbf{r}) \equiv \left[-\frac{\hbar^2}{2m_e}\nabla^2 + v(\mathbf{r})\right]\psi_i(\mathbf{r}) + e^2\sum_{j=1}^{N_e}\int \frac{d\mathbf{r}'}{|\mathbf{r}-\mathbf{r}'|}\left[|\psi_j(\mathbf{r}')|^2\psi_i(\mathbf{r}) - \psi_j^*(\mathbf{r}')\psi_i(\mathbf{r}')\psi_j(\mathbf{r})\right] = E_i\psi_i(\mathbf{r}) \tag{2.7}$$

These equations are nonlinear in $\psi_i(\mathbf{r})$ which is different from ordinary *Schrödinger equation* and it involves a non-local potential, the second term under the summation on right hand side of Eq.(2.7), called *Fock's potential*.

The fundamental drawback of *Hartree-Fock* formalism is that it ignores the electron-electron correlation that may lead to large deviation from experimental results. A number of approaches have been devised to overcome the problem of missing correlation in HF method, collectively called *post Hartree-Fock* methods [6, 7, 8]. Another important difficulty with HF method is huge computational cost for calculating every single-electron wave-function. For large and complex systems it involves exponential increase in computational cost.

2.1.3.2 Density Based Approach (*Density Functional Theory*)

Another approach to solve problem of interacting electrons, is where instead of taking electronic wave-function as basic variables electron density is considered as basic variable. Solution of electronic structure is a *many-body problem* due to the fact that electrons interact via attractive coulomb force with the stationary nuclei and repulse each other via repulsive coulomb force. Quantum many-body problems are very difficult to solve compared to classical many-body problems. The reason is that system with N_e number of electrons has many-body wave-function which is a function of $3N_e$ variables, $\Psi(\mathbf{r_1}, \mathbf{r_2}..., \mathbf{r_{N_e}})$, where $\mathbf{r}_i$'s are the 3 dimensional variables. So dealing with wave function needs huge computational cost while dealing with electron density require much lower computational cost due to reduction from $3N_e$ to 3 variables. Prior to Hartree (1928) and Hartree-Fock (1930) theories, Thomas and Fermi (1927) [9] proposed the idea of solving many-body problem using density functional approach. They considered the electron density of non-interacting homogeneous electron gas as central variable. But there are several drawbacks; (a) resulting expression for kinetic energy is approximate, (b) other source of error is the exchange energy, and (c) also error comes from complete neglect of electronic correlation. It also failed to predict bonding between atoms.
Later in 1964 Hohenberg and Kohn [10] proposed that it is possible to develop an exact theory, known as *Density Functional Theory (DFT)*, for many-body system considering of single-particle ground state density as basic variable. They proposed two important theorems:
H-K theorem I : There is one-to-one correspondence between the ground state density $\rho(\mathbf{r})$ of N_e electron system and external potential $v_{ext}(\mathbf{r})$ acting on it. It means for any system of interacting particles in an external potential $v_{ext}(\mathbf{r})$, the density is uniquely determined.
H-K theorem II : Out of all possible densities, the density that minimizes the total energy functional with a given potential is the exact ground state density. An universal *functional* for energy can be defined in terms of density.

The mathematical formulation is presented in the following.

The ground state electron density is given by

$$\rho(\mathbf{r}) = N_e \int \Psi^*(\mathbf{r}, \mathbf{r_2}, ..., \mathbf{r_{N_e}}) \Psi(\mathbf{r}, \mathbf{r_2}, ..., \mathbf{r_{N_e}}) d\mathbf{r_2} d\mathbf{r_3} ... d\mathbf{r_{N_e}} \tag{2.8}$$

where $\Psi(\mathbf{r}, \mathbf{r_2}, ..., \mathbf{r_{N_e}})$ is many-electron wave-function. Then single-particle electron-ion interaction can be written as

$$V_{en} = \int d\mathbf{r} V(\mathbf{r}) \rho(\mathbf{r}) \tag{2.9}$$

Two-electron potential term V_{ee} can be written as

$$V_{ee} = \frac{1}{2} \int \frac{d\mathbf{r_1} d\mathbf{r_2} \Gamma(\mathbf{r_1}, \mathbf{r_2})}{|\mathbf{r_1} - \mathbf{r_2}|} \tag{2.10}$$

where $\Gamma(\mathbf{r_1}, \mathbf{r_2})$ is the joint probability of finding one electron in a volume $d\mathbf{r}_1$ at $\mathbf{r}_1$ and another electron in a volume $d\mathbf{r}_2$ at $\mathbf{r}_2$ and is expressed as

$$\Gamma(\mathbf{r_1}, \mathbf{r_2}) = N_e(N_e - 1) \int \Psi^*(\mathbf{r_3}, \mathbf{r_4}, ..., \mathbf{r_{N_e}}) \Psi(\mathbf{r_3}, \mathbf{r_4}, ..., \mathbf{r_{N_e}}) d\mathbf{r_3} d\mathbf{r_4} ... d\mathbf{r_{N_e}} \tag{2.11}$$

The kinetic energy can be written as

$$\begin{aligned} T &= -N_e \frac{\hbar^2}{2m} \int \Psi^*(\mathbf{r}, \mathbf{r_2}, ..., \mathbf{r_{N_e}}) \nabla^2_{\mathbf{r}} \Psi(\mathbf{r}, \mathbf{r_2}, ..., \mathbf{r_{N_e}}) d\mathbf{r} d\mathbf{r_2} ... d\mathbf{r_{N_e}} \\ &= -N_e \frac{\hbar^2}{2m} \int \left[\nabla^2_{\mathbf{r}} \Psi^*(\mathbf{r'}, \mathbf{r_2}, ..., \mathbf{r_{N_e}}) \Psi(\mathbf{r}, \mathbf{r_2}, ..., \mathbf{r_{N_e}}) \right]_{\mathbf{r}=\mathbf{r'}} d\mathbf{r} d\mathbf{r_2} ... d\mathbf{r_{N_e}} \\ &= -\frac{\hbar^2}{2m} \int d\mathbf{r} \left[\nabla^2_{\mathbf{r}} \gamma(\mathbf{r}, \mathbf{r'}) \right]_{\mathbf{r}=\mathbf{r'}} \end{aligned} \tag{2.12}$$

where $\gamma(\mathbf{r}, \mathbf{r'})$ is first order *reduced density matrix* given by,

$$\gamma(\mathbf{r}, \mathbf{r'}) = \int \Psi^*(\mathbf{r'}, \mathbf{r_2}, ..., \mathbf{r_{N_e}}) \Psi(\mathbf{r}, \mathbf{r_2}, ..., \mathbf{r_{N_e}}) d\mathbf{r_2} d\mathbf{r_3} ... d\mathbf{r_{N_e}} \tag{2.13}$$

The density matrix formalism can now be used to express total energy of the system as

$$E[\rho, \gamma, \Gamma] = T[\gamma] + V_{en}[\rho] + V_{ee}[\Gamma] \tag{2.14}$$

Thus many-electron system can be described in terms of density matrices instead of many-electron wave-functions. By minimizing the total energy in terms of density matrices one can obtain ground state properties. However, attempt to minimize energy is complicated due to the fact that the sufficient conditions that γ and Γ must satisfy are not known. This leads to the conclusion that computing total energy using Eq.(2.14) is not possible without evaluating many-body wave-functions. The observation which support density functional theory is we do not require Γ or γ to determine total energy E as *ground state energy is completely determined by the diagonal elements of the single-particle density matrix which is electron charge density*.

Proof of H-K first theorem :

Let us consider two external potentials $v_{ext}^{(1)}(\mathbf{r})$ and $v_{ext}^{(2)}(\mathbf{r})$ which differ from each other by an additive constant and give same ground state density $\rho(\mathbf{r})$. As two different external potentials are different they would belong to different Hamiltonians, say, $H^{(1)}$ and $H^{(2)}$ respectively, which have different wave-functions $\Psi^{(1)}$ and $\Psi^{(2)}$. Variational principle tells that no wave-function can give rise to energy which is less than the energy obtained from $\Psi^{(1)}$ for $H^{(1)}$. So

$$E^{(1)} = \langle \Psi^{(1)} | H^{(1)} | \Psi^{(1)} \rangle < \langle \Psi^{(2)} | H^{(1)} | \Psi^{(2)} \rangle \tag{2.15}$$

We assume here that ground state is nondegenerate. Since we have identical ground state density for both of the Hamiltonians, Eq.(2.15) can be rewritten as

$$E^{(1)} < \langle \Psi^{(2)} | H^{(1)} | \Psi^{(2)} \rangle \quad = \quad \langle \Psi^{(2)} | H^{(2)} | \Psi^{(2)} \rangle + \langle \Psi^{(2)} | H^{(1)} - H^{(2)} | \Psi^{(2)} \rangle \tag{2.16}$$

Hence

$$E^{(1)} < E^{(2)} + \int d\mathbf{r} \rho(\mathbf{r}) \left[v_{ext}^{(1)} - v_{ext}^{(2)} \right] \tag{2.17}$$

If we interchange suffixed in Eq.(2.17) we have

$$E^{(2)} < E^{(1)} + \int d\mathbf{r} \rho(\mathbf{r}) \left[v_{ext}^{(2)} - v_{ext}^{(1)} \right] \tag{2.18}$$

Adding two inequalities Eq.(2.17) and Eq.(2.18) we have

$$E^{(1)} + E^{(2)} < E^{(2)} + E^{(1)} \tag{2.19}$$

which is absurd.

So our starting assumption was wrong and a given $\rho(\mathbf{r})$ can correspond to only one external potential $v_{ext}(\mathbf{r})$. As $v_{ext}(\mathbf{r})$ corresponding to a $\rho(\mathbf{r})$ is fixed, the Hamiltonian is also fixed. So total energy functional is a unique functional of density. It proves *Hohenberg-Kohn first theorem*.

Proof of H-K second theorem :

The external potential is uniquely determined by the density and the potential uniquely determines (except in degenerate situations) the ground state wave-function. So kinetic energy of the system is also uniquely determined. The energy therefore can be written as a functional of the density,

$$E[\rho] = T[\rho] + U_{int}[\rho] + \int v_{ext}\rho(\mathbf{r})d\mathbf{r} \tag{2.20}$$

where $U_{int}[\rho]$ is the potential energy corresponding to electron-electron interactions.
Eq.(2.20) can be written as

$$E[\rho] = F[\rho] + \int v_{ext}\rho(\mathbf{r})d\mathbf{r} \tag{2.21}$$

where F[ρ] is a universal functional whose exact form is not known to us. Ground state energy is uniquely determined by the ground state density $\rho^{(1)}(\mathbf{r})$. So,

$$E^{(1)} = E[\rho^{(1)}] = \langle\Psi^{(1)}|H^{(1)}|\Psi^{(1)}\rangle \tag{2.22}$$

Using variational principle a different density, $\rho^{(2)}$, gives higher energy ,

$$E^{(1)} = E[\rho^{(1)}] = \langle\Psi^{(1)}|H^{(1)}|\Psi^{(1)}\rangle < \langle\Psi^{(2)}|H^{(1)}|\Psi^{(2)}\rangle \tag{2.23}$$

It tells us that if we minimize the total energy *functional* of ρ by density ρ we should obtain ground state energy. The density that minimizes the energy is the ground state density.

Although Hohenberg-Kohn theorem is an "*exact theory*", in principle, for obtaining ground state properties of any system the main disadvantage is we do not know the exact form of the universal functional F[ρ]. If we would know the form of F[ρ] we could solve electronic problems exactly. Another drawback of H-K theorem is that it assumes non-degenerate ground state.

Kohn-Sham approximation :

In the Hohenberg-Kohn formulation nothing has been said about how to calculate, in practice, various quantities and functional forms related to total energy functional. In 1965 Kohn and Sham [11] proposed a formulation that leads to practical implementation of density functional theory based on Hohenberg-Kohn theorem. Kohn and Sham proposed an *idea of mapping interacting many-body system into a non-interacting electron system having the same electron density as in interacting system* (cf. Fig. 2.1).

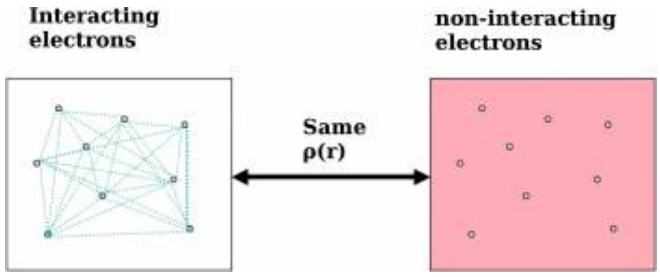

Figure 2.1 Mapping from interacting electron system of density $\rho(\mathbf{r})$ to non-interacting system of same density using Kohn-Sham approximation. Figure is adopted from lecture note by N. M. Harrison [12].

Their formulation lead to a set of self-consistent equations known as Kohn-Sham equations. The theory begins with the non-interacting reference system of N_e non-interacting electrons

moving in the external potential v_s, each in one of the N_e orbitals ψ_i. Then the Hamiltonian of such a system is

$$\hat{H}_{KS} = -\sum_{i}^{N_e} \frac{1}{2}\nabla^2 + \sum_{i}^{N_e} v_s(\mathbf{r_i}) \tag{2.24}$$

Here we have used atomic unit, $\hbar$=m$_e$=1. The Hamiltonian in Eq.(2.20) has the exact eigenfunction which is a single determinant constructed from N_e number of lowest eigen states of the one-electron equations

$$\left[-\frac{1}{2}\nabla^2 + v_s(\mathbf{r})\right]\psi_i = \varepsilon_i \psi_i \tag{2.25}$$

With the requirement that we need stationary ground state density we recall Euler-Lagrange equation whose solutions are the functions for which a given functional is stationary. In our case the Euler-Lagrange equation is

$$\mu = v_s(\mathbf{r}) + \frac{\delta T_0[\rho]}{\delta \rho} \tag{2.26}$$

where μ is Lagrange multiplier which is the chemical potential. The Kinetic energy for our system is given by,

$$T_0[\rho] = \sum_{i}^{N_e} \langle \psi^{(1)}| -\frac{\nabla_i^2}{2}|\psi_i\rangle \tag{2.27}$$

and the electron density is given by

$$\rho(\mathbf{r}) = \sum_{i}^{N_e} \mid \psi_i(\mathbf{r}) \mid^2 \tag{2.28}$$

So the total energy of the system of non-interacting particles is

$$E[\rho] = T_0[\rho] + \int d\mathbf{r} v_s(\mathbf{r})\rho(\mathbf{r}) \tag{2.29}$$

Note that the kinetic energy $T_0[\rho]$ is not the original kinetic energy $T[\rho]$. Kohn-Sham formulation, therefore reformulated the interacting problem so that its kinetic energy T_0 can be determined. The total energy of the system of non-interacting particles is therefore given by,

$$E[\rho] = T_0[\rho] + \int d\mathbf{r} v_s(\mathbf{r})\rho(\mathbf{r}) + J[\rho] + \int d\mathbf{r} v_s(\mathbf{r})\rho(\mathbf{r}) + E_{xc}[\rho] \tag{2.30}$$

where $J[\rho]$ is the coulomb integral expressed in terms of electron density and $E_{xc}[\rho]$ is the exchange-correlation energy. Euler-Lagrange equation now becomes

$$\mu = v_{KS}(\mathbf{r}) + \frac{\delta T_0[\rho]}{\delta \rho} \tag{2.31}$$

where Kohn-Sham effective potential v_{KS} is defined as

$$v_{KS}(\mathbf{r}) = v_s(\mathbf{r}) + \int \frac{\rho(\mathbf{r}')}{|\mathbf{r}-\mathbf{r}'|} d\mathbf{r}' + v_{xc}(\mathbf{r}) \tag{2.32}$$

where the exchange-correlation potential v_{xc} is given by

$$v_{xc}(\mathbf{r}) = \frac{\delta E_{xc}[\rho]}{\delta \rho} \tag{2.33}$$

Kohn and Sham noticed that the equation is the same as that for *non-interacting system under an effective potential* v_{KS}. Therefore exact ground state density can be obtained by solving N_e single-electron equations

$$\left[-\frac{1}{2}\nabla^2 + v_{KS}(\mathbf{r})\right]\psi_i = \varepsilon_i \psi_i \tag{2.34}$$

which are known as *Kohn-Sham equations*. The self-consistent iterative method for solving *Kohn-Sham equations* is shown in the Fig. 2.2

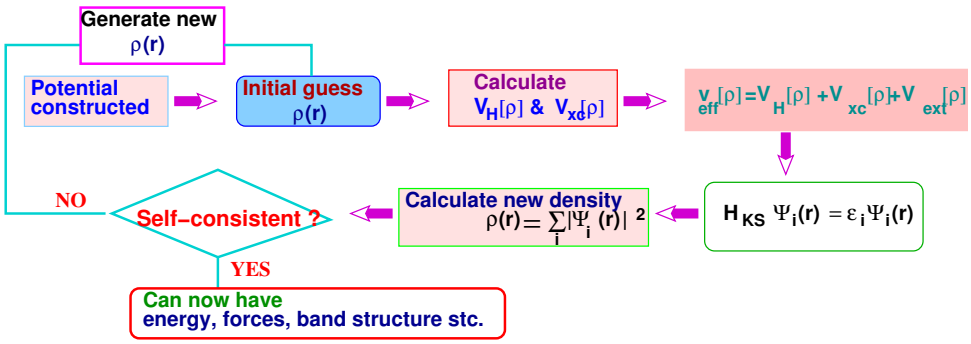

Figure 2.2 Self-consistent loop for solving Kohn-Sham differential equations.

2.1.4 Exchange-Correlation

In the expression for Kohn-Sham energy functional all the terms can be determined exactly except E_{xc} as exact form of v_{xc} is not known to us. The exchange-correlation energy functional $E_{xc} = E_x + E_c$, where E_x is the *exchange* term and E_c is the *correlation* term. As we know that due to Pauli's exclusion principle two parallel spins can not be at the same position in space, but opposite spin can. This interaction is called *exchange*. The exchange term can be calculated exactly as in Hartree-Fock formalism.

Let us discuss the *correlation* term. If $g(\mathbf{r},\mathbf{r}')$ is the two-body correlation function , then two particle density matrix can be written as

$$\Gamma(\mathbf{r},\mathbf{r}') = \frac{1}{2}\rho(\mathbf{r})\rho(\mathbf{r}')g(\mathbf{r},\mathbf{r}') \tag{2.35}$$

which implies

$$\langle\psi|V_{ee}|\psi\rangle = \frac{1}{2}\int\frac{\rho(\mathbf{r})\rho(\mathbf{r}')}{|\mathbf{r}-\mathbf{r}'|}d\mathbf{r}d\mathbf{r}' + \frac{1}{2}\int\frac{\rho(\mathbf{r})\rho(\mathbf{r}')}{|\mathbf{r}-\mathbf{r}'|}\left[g(\mathbf{r},\mathbf{r}')-1\right]d\mathbf{r}d\mathbf{r}' \tag{2.36}$$

The first term in Eq.(2.36) is electron-electron coulomb repulsion and the second term is *correlation effect*. The correlation energy is Coulombic. Since the correlation is probabilistic quantity its exact form is not known. Though exchange term can be determined exactly to compensate the error arising due to lack of exact form for correlation, approximation is used for both exchange and correlation functions. For exchange-correlation energy functional many approximations are available nowadays for the improvement in prediction of ground state properties. Here only two of them are presented.

2.1.4.1 Local Density Approximation

Most widely used approximation for exchange-correlation energy functional is the local density approximation (LDA) for which exchange-correlation energy density $\varepsilon_{xc}(\mathbf{r})$ is taken as

that of a homogeneous electron gas (the nuclei are replaced by uniform positive charge background called *Jellium model*). That means generally inhomogeneous gas is considered locally homogeneous. The approximation was proposed by Kohn and Sham in 1965 though very idea was already given by Thomas, Fermi and Dirac in 1927. Now one can write the exchange-correlation energy as an average of energy density $\varepsilon_{xc}^{LDA}[\rho]$.

$$E_{xc}^{LDA} = \int \rho(\mathbf{r})\varepsilon_{xc}^{LDA}[\rho]d\mathbf{r} \tag{2.37}$$

where $\varepsilon_{xc}[\rho] = \varepsilon_x[\rho] + \varepsilon_c[\rho]$ and the exchange energy $\varepsilon_x[\rho]$ is exactly given by [13, 14]

$$\varepsilon_x^{LDA} = -\frac{3}{4\pi}(3\pi^2 N_e)^{1/3} \tag{2.38}$$

The rest of $\varepsilon_{xc}^{LDA}[\rho]$ is kept in $\varepsilon_c^{LDA}[\rho]$ for which there is no exact analytical formula. But correlation energies are known exactly from quantum Monte Carlo (QMC) calculation by Ceperley and Alder (1980) [15]. The energies were fitted by Vosko, Wilkes and Nussair (VWN) [16] with $\varepsilon_c^{LDA}[\rho]$ and they have obtained accurate results with errors less than 0.05 mRy in $\varepsilon_c^{LDA}[\rho]$. VWN result is given by

$$\varepsilon_c^{LDA}[\rho] \approx \frac{A}{2}[ln\left(\frac{y^2}{Y(y)}\right) + \frac{2b}{Q}tan^{-1}\left(\frac{Q}{2y+b}\right) - \frac{by_0}{Y(y_0)}\left[ln\left(\frac{(y-y_0)^2}{Y(y)}\right) + \frac{2(b+2y_0)}{Q}tan^{-1}\left(\frac{Q}{2y+b}\right)\right]] \tag{2.39}$$

where $y = \sqrt{r_s}$, $Y(y) = y^2 + by + c$, $Q = \sqrt{4c - b^2}$, $y_0 = -0.105, b = 3.727, c = 12.935, A = 0.0622$ and r_s is electron gas parameter which is mean distance (in atomic unit) between atoms. There is another formula for exchange-correlation functions by Perdew and Zunger (1981) [17] which gives the similar result. Later the correlation functional has been parametrized by John P. Perdew and Yue Wang [18].

For magnetic systems the LDA is extended taking into account spin-polarization which is called local spin density approximation (LSDA) [19]. Here $\rho(\mathbf{r})$ split into $\rho_\downarrow(\mathbf{r})$ and $\rho_\uparrow(\mathbf{r})$

and exchange-correlation energy functional is

$$E_{xc}^{LSDA} = \int (\rho_\uparrow + \rho_\downarrow)\varepsilon_{xc}[\rho_\uparrow, \rho_\downarrow]d\mathbf{r} \tag{2.40}$$

LDA, though simple, is surprisingly very successful. The main reason is because the exchange-correlation energy does not depend on shape but the size of the exchange-correlation hole. Also, LDA satisfies the sum rule that means exchange and correlation hole integrates over space exactly to -1 per electron.

2.1.4.2 Generalized Gradient Approximation

The Eq.(2.40) is valid when the spin density varies very slowly over space which is not always true for real atoms, molecules and solids. A correction was made for slowly varying limit with second order gradient expansion approximation (GEA)[20, 18, 21, 22]

$$E_{xc}^{GEA}[\rho_\uparrow, \rho_\downarrow] = E_{xc}^{LSDA} + \sum_{\sigma,\sigma'} \int C_{xc}^{\sigma,\sigma'}(\rho_\uparrow, \rho_\downarrow) \frac{\nabla\rho_\sigma \cdot \nabla\rho_{\sigma'}}{\rho_\sigma^{2/3}\rho_{\sigma'}^{2/3}} d\mathbf{r} \tag{2.41}$$

which is asymptotically valid for system with slowly varying density but inclusion of correlation in second order gives energies less accurate than LSDA [20, 23]. The constant $C_{xc}^{\sigma,\sigma'}(\rho_\uparrow, \rho_\downarrow)$ is determined variationaly for each atom [24]. Then improvement over the approximations LSDA and GEA is needed for the system where density varies rapidly and that is done by introducing Generalized Gradient Approximation (GGA) [25, 26] whose functional form (only upto second order derivative) is given by,

$$E_{xc}^{GGA}[\rho] = \int \rho(\mathbf{r})\varepsilon_{xc}^{GGA}(\rho(\mathbf{r}), |\nabla\rho(\mathbf{r})|, \nabla^2\rho(\mathbf{r}))d\mathbf{r} \tag{2.42}$$

Various GGA functional forms have been proposed [25, 27, 18, 21, 22, 28, 29] for the improvement of results. GGA reduces the bond dissociation energy error and generally improve transition state barrier and gives better magnetic properties, but unlike LDA there is no single universal form. The calculations presented in the thesis are mostly done by the GGA

exchange-correlation functional known as PBE functional proposed by Perdew, Burke and Ernzerhof [30] in 1996.

2.1.5 Basis sets

To solve electronic structure theory we need to solve Schrödinger equation, which means we need basis functions to expand the wave function. Depending on the choice of basis sets various electronic structure methods have been developed. Different basis sets can be primarily put into two categories- (i) fixed basis sets, and (ii) partial wave methods. Each method has its own advantages and disadvantages.

(i) Fixed Basis Set Method

The wave-function is determined as an expansion in some set of fixed basis functions, like linear combination of atomic orbitals (LCAO) [31], plane wave [32], gaussian type orbitals (GTO) [33], slater type orbitals (STO) [34] etc. One has to solve the eigenvalue problem

$$(H - \varepsilon O).a = 0 \tag{2.43}$$

where H is the Hamiltonian and O is the overlap matrix. ε are eigenvalues to be obtained after solving Eq.(2.43) and a is the expansion coefficient matrix that gives eigenvectors. [35]

The main advantage of *fixed basis method* is that it is computationally very simple and faster, while the disadvantage is that the basis set may be large to be reasonably complete. Out of different fixed basis set methods plane wave basis set is most popular.

(ii) Partial Wave Method

In this approach, the wave-function is expanded in a set of energy and potential dependent partial waves like cellular method [36], augmented plane wave method [37], Korringa-Kohn-Rostoker method (KKR) [38, 39]. In partial wave method, one needs to solve the following

set of equations

$$M(\varepsilon).b = 0 \tag{2.44}$$

The above equations have complicated non-linear energy dependence [35].

The partial wave method has many advantages - (a) basis set is minimal that means minimum number of basis functions are needed for each atom, (b) partial waves apply equally well to any atom in the periodic table, (c) offers solutions of arbitrary accuracy for close packed system contrary to fixed basis set method. But the main disadvantage is that partial wave method is computationally heavy. To overcome the complexity of non-linear energy dependence, Andersen (1975) [40] first proposed methods involving linear energy dependence such as Linear Muffin Tin Orbital (LMTO) and Linear Augmented Plane Wave (LAPW) method.

In the present thesis we have used LMTO method as implemented in Stuttgart code [41], LAPW method as implemented in Wien2k code [42, 43] and also pseudopotential method along with plane wave basis as implemented in VASP [44, 45, 46, 47]. We have used these methods for the calculation of total energies and electronic structure analysis. For the calculation of wannier functions we have used N^{th} order Muffin-Tin Orbital (NMTO) downfolding method. In the following subsections we provide brief discussion on each of these methods.

2.1.5.1 Linear Muffin-Tin Orbital Method

Linear Muffin-Tin Orbital (LMTO) method [41] provides minimal basis set for solving Kohn-Sham equations. The method uses *muffin-tin approximation*. In this approximation potential is assumed to be spherically symmetric close to the nuclei- the spherical region is called *muffin-tin sphere* and potential is assumed to be flat in between *muffin-tin spheres*- the region is called

interstitial. Mathematically muffin-tin potential can be defined as

$$\begin{aligned} v(\mathbf{r}-\mathbf{R}) &= v(r_R); \quad r_R \leq s_R \\ &= -v_0; \quad r_R > s_R, \quad r_R = |\mathbf{r}-\mathbf{R}| \end{aligned} \tag{2.45}$$

where $\mathbf{r}$ is any position in the solid and $\mathbf{R}$ is the position of the nuclei. s_R is the muffin-tin radius of the sphere at $\mathbf{R}$.

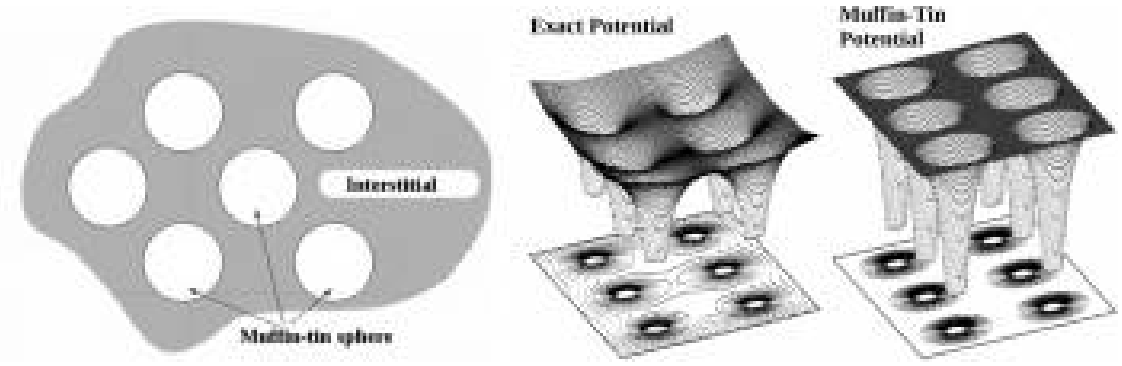

Figure 2.3 Left panel: Muffin-tin spheres and the interstitial region. Comparison between exact potential and muffin-tin potential is shown in the middle and right most panel. Figure adopted from [35].

Inside the Muffin-Tin (MT) sphere the solutions of the Schrödinger's equation are partial waves, as the potential is spherically symmetric, and can be written as $\phi(\mathbf{r_R}) = \phi_{Rl}(r_R,\varepsilon)Y_L(\hat{r}_R)$. The solution $\phi_{Rl}(r_R,\varepsilon)$ satisfies radial Schrödinger's equation

$$\left[\frac{d^2}{dr_R^2} - v(r_R) + \frac{l(l+1)}{r_R^2} - \varepsilon\right] r_R\phi_{Rl}(r_R,\varepsilon) = 0 \tag{2.46}$$

$Y_L(\hat{r}_R)$'s are the spherical harmonics where L represents angular momentum quantum numbers (l,m).

Outside muffin-tin sphere the radial Schrödinger's equation becomes

$$\left[\frac{d^2}{dr_R^2} + \frac{l(l+1)}{r_R^2} - \kappa^2\right] r_R\phi_{Rl}(r_R,\varepsilon) = 0 \tag{2.47}$$

where $\kappa^2 = \varepsilon - v_0$.

Hence the solution of Eq.(2.47) is plane wave which can be expanded in terms of spherical Bessel and Neumann functions,

$$A_{Rl}(\varepsilon,\kappa) j_l(\kappa, r_R) + B_{Rl}(\varepsilon,\kappa)\eta_l(\kappa, r_R) \tag{2.48}$$

The total solution is given by

$$\phi_{Rl}(r_R,\varepsilon) = \begin{cases} N^0_{RL}(\varepsilon,\kappa)\phi_{Rl}(r_R,\varepsilon), & \text{if } r_R \leq s_R \\ \eta_l(\kappa, r_R) + P^0_{RL}(\varepsilon,\kappa) j_l(\kappa, r_R), & \text{if } r_R > s_R \end{cases} \tag{2.49}$$

Where $N^0_{RL}(\varepsilon,\kappa)$ is normalization function and $P^0_{RL}(\varepsilon,\kappa)$ is potential function.

To have a basis such that head contains all information about potential and tail contains information of potential outside the sphere we can rewrite Eq.(2.49) as,

$$\phi_{Rl}(r_R,\varepsilon) = \begin{cases} N^0_{RL}(\varepsilon,\kappa)\phi_{Rl}(r_R,\varepsilon) + P^0_{RL}(\varepsilon,\kappa) j_l(\kappa, r_R), & \text{if } r_R \leq s_R \\ \eta_l(\kappa, r_R), & \text{if } r_R > s_R \end{cases} \tag{2.50}$$

The new basis is well behaved in all space. Considering array of ion cores with intervening interstitials the wave-function of the system can be written as linear combination of the MT orbitals ,

$$\Psi(r,\varepsilon) = \sum_R \sum_L C_{RL}(\varepsilon)\chi_{RL}(r-R,\varepsilon) \tag{2.51}$$

The expression for the tails of the Neumann function $\eta_l(\kappa, r_R)$ outside its own sphere can be written as

$$\eta_l(\kappa, r_R) = -\sum_{l'} S^0_{RL,R'L'}(\kappa) j_{l'}(\kappa, r_{R'}) \tag{2.52}$$

$S^0_{RL,R'L'}(\kappa)$ are canonical structure constants depending on the R and R' and independent of ion-core potentials.

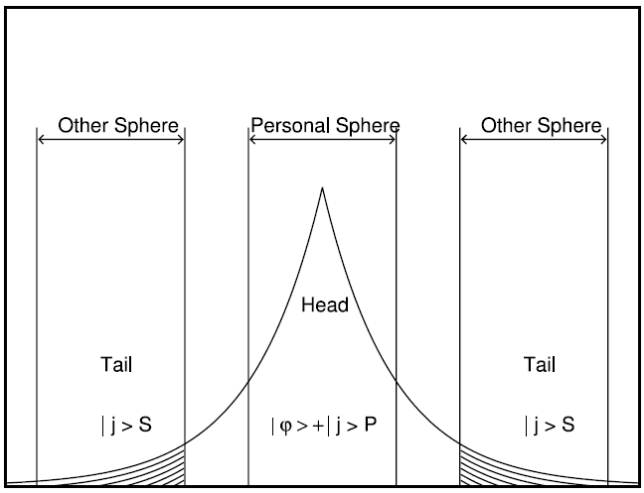

Figure 2.4 Muffin-tin orbital with its head in its own sphere and tails in other neighboring spheres. Figure adopted from [35].

As shown in Fig.2.4 the muffin-tin orbitals, can then be written as

$$\chi_{RL}(r-R,\varepsilon) = \begin{cases} \left[N^0_{RL}(\varepsilon,\kappa)\phi_{Rl}(r_R,\varepsilon) + P^0_{RL}(\varepsilon,\kappa)\, j_l(\kappa,r_R)\right] Y_L(\hat{r}_R), & \text{if } r_R \le s_R \\ -\sum_{L'} S^0_{RL,R'L'}(\kappa)\, j_{l'}(\kappa,r_{R'}) Y_L(\hat{r}_R), & \text{if } r_{R'} \le s_{R'} \\ -\sum_{L'} S^0_{RL,R''L'}(\kappa)\, j_{l'}(\kappa,r_{R''}) Y_L(\hat{r}_R), & \text{if } r_{R''} \le s_{R''} \\ \ldots\ldots\ldots\ldots & \\ \eta_l(\kappa,r_R) Y_L(\hat{r}_R), & \text{if } r_R \in \text{interstitial} \end{cases} \tag{2.53}$$

Let us define few notations for functions as

$\| \Psi_R\rangle$ represents function defined in all space

$|\Psi_R\rangle$ is zero outside its own sphere, and

$|\Psi_R\rangle^{\ddagger}$ is nonzero only in the interstitial space.

Then we can write a MT orbital defined all over the space as

$$\| \chi_R(\varepsilon)\rangle = N^0_R(\varepsilon)|\phi_R(\varepsilon)\rangle + P^0_R(\varepsilon,\kappa)|j_R(\kappa)\rangle - \sum_{R'} S^0_{R,R'}(\kappa)|j_{R'}(\kappa)\rangle + |\eta_R(\kappa)\rangle^{\ddagger} \tag{2.54}$$

The total wave-function can be written as linear combination of all MT orbitals,

$$\| \Psi_R\rangle = \sum_R C_R^+(\varepsilon) \| \chi_R(\varepsilon)\rangle \tag{2.55}$$

Let us consider a single MT sphere centered at R_0, then solution to Schrödinger's equation within MT sphere $r_{R_0} < s_{R_0}$ is,

$$|\Psi(\varepsilon)\rangle = C_{R_0}^+(\varepsilon) N_{R_0}^0(\varepsilon) |\phi_{R_0}(\varepsilon)\rangle \tag{2.56}$$

Substituting Eq.(2.54) into Eq.(2.55) and after few simplifications we can write

$$|\Psi(\varepsilon)\rangle = \sum_R C_R^+(\varepsilon)[N_{RR_0}^0(\varepsilon)|\phi_R(\varepsilon)\rangle + (P_{RR_0}^0(\varepsilon,\kappa) - S_{RR_0}^0(\kappa))|j_R(\kappa)\rangle] \tag{2.57}$$

Comparing Eq.(2.54) and Eq.(2.57) we see that extra term $P_{R_0}^0|j_{R_0}(\kappa)\rangle$ which was added to partial wave of head of MT orbital is canceled by the contributions of the tails of the MT orbitals from other neighboring spheres. It is called *tail cancellation* condition, given by

$$C^+ N_{RR_0}^0(\varepsilon)^{-1}[P_{RR^0}^0(\varepsilon,\kappa) - S_{RR^0}^0(\kappa)] = 0 \tag{2.58}$$

After solving above set of linear equations we obtain the coefficients $C(\varepsilon)$.

This leads to the *Korringa−Kohn−Rostoker (KKR) equations*,

$$det \parallel P^0(\varepsilon,\kappa) - S^0(\kappa) \parallel = 0 \tag{2.59}$$

Solving the determinantal equation we can obtain the eigenvalues ε.

Main problem with KKR equations is that the basis set is energy dependent. Andersen [41] found the method of linearising the equations. The energy dependent basis can be expanded in Taylor series with respect to some reference energy ε_{RL}^ν as

$$|\Psi_{RL}(\varepsilon)\rangle = |\Psi_{RL}(\varepsilon^\nu)\rangle + (\varepsilon - \varepsilon_{RL}^\nu)|\dot{\Psi}_{RL}(\varepsilon)\rangle + O((\varepsilon - \varepsilon_{RL}^\nu)^2) \tag{2.60}$$

We now can define two wave functions

$$|\Phi(\varepsilon)\rangle = N^0(\varepsilon)(N^0)^{-1}|\phi(\varepsilon)\rangle \tag{2.61}$$

$$|\dot{\Phi}(\varepsilon)\rangle = N^0(\varepsilon)(N^0)^{-1}|\dot{\phi}(\varepsilon)\rangle + \dot{N}^0(\varepsilon)(N^0)^{-1}|\phi(\varepsilon)\rangle \tag{2.62}$$

To linearize the MT orbitals, one need to replace the head by linear combination of $|\phi(\varepsilon)\rangle$ and $|\dot{\phi}(\varepsilon)\rangle$ and consider Neumann function at a fixed value of κ. Also tails of LMTO's are replaced by $|\dot{\phi}_{R'}(\varepsilon)\rangle$

So the LMTO basis function becomes

$$\begin{aligned} \| \chi_R\rangle &= \| \eta_R\rangle + |\phi_R\rangle + \sum_{R'} h_{RR'}|\dot{\phi}_{R'}(\varepsilon)\rangle - |\eta_R\rangle \\ &= |\phi_R\rangle + \sum_{R'} h_{RR'}|\dot{\phi}_{R'}(\varepsilon)\rangle + |\eta_R(\kappa)\rangle^{\ddagger} \end{aligned} \tag{2.63}$$

Then the secular equation to be solved, using variational method, is

$$\| H - \varepsilon I \| = 0 \tag{2.64}$$

Now potential term can be expanded in terms of reference energy as

$$P^0(\varepsilon) = P^0 + (\varepsilon I - \varepsilon^{\nu})\dot{P}^0 \tag{2.65}$$

Using this expansion of potential function we have

$$det[(P^0)^{1/2}] \,\|\, P^0(\dot{P}^0)^{-1} + \varepsilon I - \varepsilon^{\nu} - (\dot{P}^0)^{-1/2} S^0 (\dot{P}^0)^{-1/2} \,\|\, det[(P^0)^{1/2}] \tag{2.66}$$

if $det[(P^0)^{1/2}] \neq 0$, we get

$$det \,\|\, P^0(\dot{P}^0)^{-1} + \varepsilon I - \varepsilon^{\nu} - (\dot{P}^0)^{-1/2} S^0 (\dot{P}^0)^{-1/2} \,\| = 0 \tag{2.67}$$

Comparing Eq.(2.67) with Eq.(2.64) we have

$$H = C + \triangle^{1/2} S \triangle^{1/2} \tag{2.68}$$

with $C = -P^0(\dot{P}^0)^{-1}$ known as *band centre* parameter and $\triangle = (\dot{P}^0)^{-1}$ known as *band width* parameter.

The LMTO method is accurate upto first order in $(\varepsilon - \varepsilon^{\nu})$ within muffin-tin sphere and to zeroth order in the interstitial. Later *Atomic Sphere Approximation (ASA)* has been used with

traditional *LMTO method* [48]. In this approximation MT spheres are blown up until the total volume occupied by the spheres is equal to the volume of unit cell. With the use of ASA it eliminates the interstitial and increases the accuracy. *LMTO-ASA* works very well for close packed structure. But for open structures empty spheres (spheres with no electronic charge) are needed to fill the space.

2.1.5.2 Nth order Muffin-Tin Orbital Downfolding Method

As an input to many-body calculation, we often need to obtain low energy Hamiltonian out of full DFT Hamiltonian. Downfolding procedure [49] is capable of doing this. In this method the basis set is divided into two subsets, (a) $|l\rangle$ lower subset and (b) $|s\rangle$ intermediate subset. The reduction of full Hamiltonian H into lower subset Hamiltonian $\tilde{H_{ll}}$ is done so that lower l eigenvalues of original Hamiltonian H and eigenvalues of $\tilde{H_{ll}}$ are the same. The expression for $\tilde{H_{ll}}$ is given by

$$\tilde{H_{ll}} = H_{ll} - H_{lh}(H_{hh} - \varepsilon)^{-1}H_{hl} \tag{2.69}$$

This expression involves energy and energy dependence is removed by linearization or N-inazation using LMTO or NMTO method [50].

Though downfolding method can be used in TB-LMTO method to obtain real space hopping integrals, LMTO does not give accurate method to obtain *massive downfolding* where one selects very few bands out of all bands. The disadvantages of TB-LMTO method are ,

(i) LMTO basis is complete up to $(\varepsilon - \varepsilon^{\nu})$ (i.e., *first order*) inside the muffin-tin sphere while it is only complete to $(\varepsilon - \varepsilon^{\nu})^0$ (i.e., *zeroth order*) in the interstitial. This inconsistency can be removed by introducing Atomic Sphere Approximation (ASA), but that complicates the formulation.

(ii) The expansion of Hamiltonian in the orthogonal representation as a power series in the

two centered tight-binding Hamiltonian h,

$$< \tilde{\chi}|H - \varepsilon^{v}|\tilde{\chi} >= h - hoh + \cdots \tag{2.70}$$

which is obtained only within ASA and excluding downfolding. [35]

The idea behind the formulation of NMTO method [51] is to develop a more general polynomial MTO scheme of degree N, which allows to use N^{th} order Taylor series or allows to use a mesh of $N+1$ discrete reference energy points so that one can obtain more accurate results over a wider energy range without increasing the size of basis set.

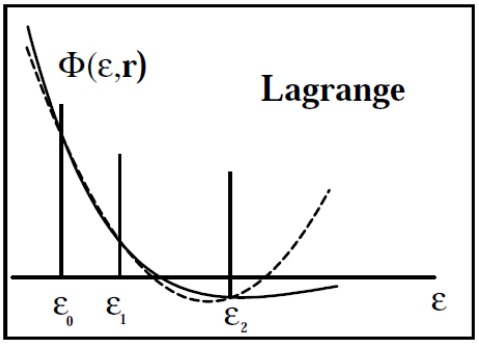

Figure 2.5 Quadratic approximation to energy dependence of a partial wave for discrete energy mesh. Figure taken from [35].

The salient features of the NMTO method are the following. (i) NMTO method still uses MT potential. (ii) NMTO method still uses partial waves $\phi_{RL}(\varepsilon, r_R)$ in atomic sphere. (iii) Instead of Neumann function as in standard LMTO method, it uses screened spherical waves (SSW) in the interstitial region. (iv) NMTO method treats the interstitial region accurately and goes beyond the linear approximation.

The formulation of NMTO basis is described briefly as follows. [35]

We position a spherical wave $Y_L(\theta,\phi)\eta_l(\kappa,r)$ at a site R. We want solution of wave equation which is a spherical wave Y_L in its own sphere and zero at all other spheres and for all other

angular momenta. The solution to this boundary value problem is called *screening transformation* [41]. We now define *hard screening spheres* of radius a_R which is less than the radius of MT spheres s_R . The screening spheres are not allowed to overlap. The MT spheres are *potential spheres* and screening spheres are *charge spheres*. The partial wave ϕ_{RL} is the solution (shown by red line in figure 2.5) of Schrödinger equation inside the MT sphere. ϕ_{RL} is given by numerical integration of Schrödinger equation out to the MT sphere (radius s_R) in the potential $v(r)$. Now integration is done backward to the screening sphere (radius a_R) and using flat interstitial potential v_0 which gives the solution ϕ^0_{RL} (shown by green line in figure 2.5). The solution ψ_{RL} (shown by blue line in figure 2.5) at screening sphere has continuous value but not continuous derivative. Then the total solution, namely the screened spherical wave (SSW), Ψ_{RL} (corresponding to single sphere) is given by

$$\Psi_{RL} = (\phi_{RL} - \phi^0_{RL})Y_L + \psi_{RL} \tag{2.71}$$

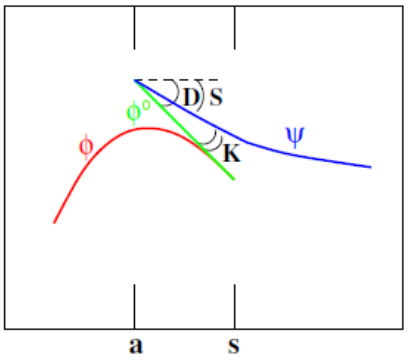

Figure 2.6 The kinked partial waves at screening spheres. Figure taken from [35].

This is the solution to the Schrödinger equation at energy ε corresponding to its own MT potential and for the flat interstitial potential. But the solution has a *kink* (discontinuous spatial derivative) at all screening spheres (cf. Fig. 2.6). Now, the solution in all space at an energy ε

is $\Psi(\varepsilon) = \sum_R \Psi_{RL}(\varepsilon)$ must be differentiable and for that sum of kinks of $\Psi_{RL}(\varepsilon)$ must vanish,

$$K.v = 0$$
$$a[D-S].v = 0 \tag{2.72}$$

where $K = a[D-S]$ is kink matrix with $D = \dfrac{a}{\phi^0_{RL}(a)} \dfrac{d\phi^0_{RL}}{dr}$. Kink matrix contains values of kinks of all the $\Psi_{RL}(\varepsilon)$ at all screening spheres. The above equation is called *kink cancellation* (cf. Fig. 2.7) in comparison to previous *tail cancellation* condition. [35]

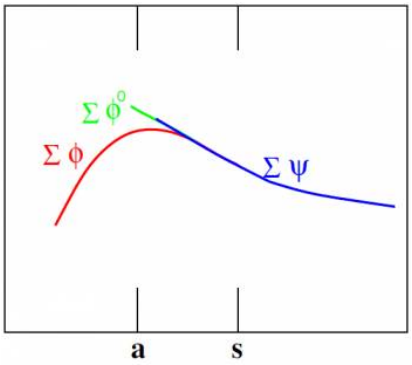

Figure 2.7 The kink cancellation make the solution continuous at the spheres. Figure taken from [35].

Now the members (labeled by R', L') of the NMTO basis set $\chi^{(N)}_{R',L'}(r_R)$ is constructed by Lagrange's interpolation of $\phi_{RL}(\varepsilon_n, r_R)$ evaluated at the energy points $\varepsilon_0, \cdots\cdots, \varepsilon_N$,

$$\chi^{(N)}_{R',L'}(r_R) = \sum_{n=0}^{N} \sum_{RL} \phi_{RL}(\varepsilon_n, r_R) L^{(N)}_{nRL,R',L'} \tag{2.73}$$

Therefore the construction of basis is energy selective and localized in nature. The energy selective and localized nature of NMTO basis makes NMTO basis set *flexible* and may be chosen as *truely minimal* which can span selected bands with as few basis functions as the number of bands. If these bands are isolated NMTO basis set spans the Hilbert space of *Wannier functions* and orthonormalized NMTOs are the *Wannier functions*. Even if the bands overlap

with other bands it is possible to pick those few bands and the corresponding Wannier-like functions with NMTO downfolding method. Therefore NMTO-downfolding method can be used for direct generation of Wannier functions. The real space representation of downfolded Hamiltonian provides information regarding effective hopping interactions, onsite energies etc. which have been used in the present thesis.

2.1.5.3 Linear Augmented Plane Wave Method

Linear Augmented Plane Wave (LAPW) basis set is constructed by partitioning the space into two parts - (a) spheres around each atom where wavefunctions are rapidly varying and atomic like, and (b) the region in between spheres, interstitial, where wavefunctions are varying smoothly and not atomic like. In the interstitial region basis functions are plane waves.

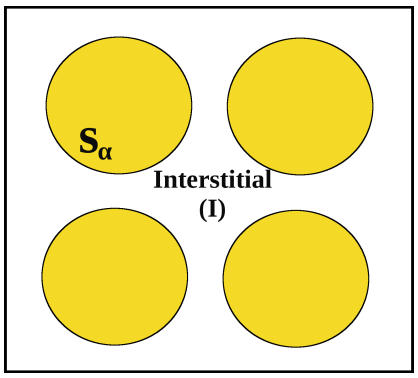

Figure 2.8 The partition of unit cell in LAPW method.

Therefore each basis function is defined as linear combination of atomic like functions inside the sphere which is connected smoothly to the plane wave in the interstitial region. Mathematically it is represented by,

$$\chi_{\mathbf{k},i}(\mathbf{r}) = \begin{cases} \sum_{lm}[a^{\alpha}_{lm}u^{\alpha}_{l}(\varepsilon_{l,1},r_\alpha) + b^{\alpha}_{lm}\dot{u}^{\alpha}_{l}(\varepsilon_{l,1},r_\alpha)]Y_{LM}(\hat{r}_\alpha), & \text{if } \mathbf{r} \in s_\alpha \\ \frac{1}{\sqrt{\Omega}}e^{j(\mathbf{G}_i+\mathbf{k})\cdot\mathbf{r}}, & \text{if } \mathbf{r} \in I \end{cases} \tag{2.74}$$

where $u_l^{\alpha}(\varepsilon_l, r_\alpha)$ is the solution of radial Schrödinger equation for an atom α, azimuthal quantum number l and linearization energy $\varepsilon_{l,1}$ (the meaning of index '1' in energy is representing one linearization energy), with $\mathbf{k}$ being wave vector in the Brillouin zone and $\mathbf{G_i}$ being reciprocal lattice vector. a_{lm} and b_{lm} are determined by the condition that the wave function should be continuous and smooth at the sphere boundary. To satisfy boundary condition plane wave basis in the interstitial is expanded in terms of Bessel functions $j_l(\mathbf{k}, r)$ as $\sum_{lm}^{\infty} 4\pi j^l j_l((k+G), r) Y_{LM}^*(\hat{r}) Y_{LM}(\hat{r})$ which must match the solution within the sphere at the sphere boundary. In principle, large number of partial waves (l values) are required to exactly satisfy the boundary conditions. But in practice the lm series is truncated at a desired value of l_{max}.

The function $Y_{l_{max},m}(\theta, \phi)$ has $2l_{max}$ number of nodes, for a given l_{max}, (where θ is 0 to 2π for fixed value of ϕ) for the α sphere. Then nodes per unit length is $\frac{2l_{max}}{2\pi R_\alpha} = \frac{l_{max}}{\pi R_\alpha}$. To match plane wave with solution inside sphere, the plane wave must have same number of nodes per unit length. The plane wave with the minimum period of $\frac{2\pi}{G_{max}}$ has $\frac{2}{\frac{2\pi}{G_{max}}} = \frac{G_{max}}{\pi}$ number of nodes per unit length. The plane wave cut-off G_{max} and angular momentum cut-off l_{max} are comparable only if the number of nodes per unit length are identical. Therefore we have the condition for cut-off l_{max} to be

$$l_{max} = R_\alpha^{min} \times G_{max} \tag{2.75}$$

where R_α^{min} is the smallest muffin-tin radius. With this condition less number of plane waves are required to describe the smoother part of the wave function. The value of G_{max} can be reduced and the product $R_\alpha^{min} \times G_{max}$ should remain constant to obtain greater accuracy. Compared to a plane wave basis set LAPW basis set can thus be much smaller.

A *core state* is a state which does not participate in the chemical bonding with other atoms rather prefers to stay entirely within the muffin-tin sphere. On the other hand *valence states* participate in the chemical bonding and they leak out of muffin-tin sphere. The problem arises

when the states with the same l but different principal quantum number n both participate in valence states. For example, Fe in BCC structure has finite amount of 4p character in the valence states that are about 0.2 Ryd below Fermi level. But 3p state that are 4.3 Ryd below Fermi level are not entirely confined to its core state. Such *low lying* valence states are called *semi-core states*. This situation has been solved by introducing another kind of basis function to LAPW basis set, called *local orbital* (LO) . LO for a particular l and m, and for a particular atom α is defined as

$$\phi_{lm}^{\alpha,LO}(\mathbf{r}) = \begin{cases} [a_{lm}^{\alpha,LO} u_l^\alpha(\varepsilon_{l,1}, r_\alpha) + b_{lm}^{\alpha,LO} \dot{u}_l^\alpha(\varepsilon_{l,1}, r_\alpha) + c_{lm}^{\alpha,LO} u_l^\alpha(\varepsilon_{l,2}, r_\alpha)] Y_{LM}(\hat{r}_\alpha), & \text{if } \mathbf{r} \in s_\alpha \\ 0, & \text{if } \mathbf{r} \in I \end{cases} \tag{2.76}$$

It is called "*local*" because it is zero in the interstitial and within the spheres of other atoms. Within the sphere of atom α, the solutions u_l^α and $\dot{u}_l^\alpha$, same as in LAPW basis, are used with linearization energy $\varepsilon_{l,1}$. The lower valence state is sharply peaked at energy $\varepsilon_{l,2}$. The single radial solution $u_l^\alpha(\varepsilon_{l,2}, r_\alpha)$ at energy $\varepsilon_{l,2}$ describes lower valence state. The three coefficients are determined by using the condition that LO is normalized and has zero value and zero slope at the muffin-tin boundary. The only problem with LAPW [42] +LO method is that accuracy comes with the cost of increased computational time due to increase in the number of basis per atom.

Later APW+lo [52] method is introduced where the basis set will be energy independent and basis has the same size as in the APW method. In this sense, APW+lo includes the good features of both APW and LAPW+LO. The APW+lo basis contains two kinds of functions. The first kind are APWs,

$$\chi_{\mathbf{k},i}(\mathbf{r}) = \begin{cases} \sum_{lm} a_{lm}^\alpha u_l^\alpha(\varepsilon_{l,1}, r_\alpha) Y_{LM}(\hat{r}_\alpha), & \text{if } \mathbf{r} \in s_\alpha \\ \frac{1}{\sqrt{\Omega}} e^{j(\mathbf{G}_i + \mathbf{k})\cdot\mathbf{r}}, & \text{if } \mathbf{r} \in I \end{cases} \tag{2.77}$$

The basis function is augmented with second type of functions *local orbitals* which is other kind than one used with LAPW basis. So this time they are called 'lo' instead of 'LO' and are defined as,

$$\phi_{lm}^{\alpha,LO}(\mathbf{r}) = \begin{cases} [a_{lm}^{\alpha,lo} u_l^{\alpha}(\varepsilon_{l,1}, r_\alpha) + b_{lm}^{\alpha,lo} \dot{u}_l^{\alpha}(\varepsilon_{l,1}, r_\alpha)] Y_{LM}(\hat{r}_\alpha), & \text{if } \mathbf{r} \in s_\alpha \\ 0, & \text{if } \mathbf{r} \in I \end{cases} \tag{2.78}$$

The two coefficients $a_{lm}^{\alpha,lo}$ and $b_{lm}^{\alpha,lo}$ are determined with the condition that the value of local orbitals (lo) are zero at the sphere boundary, but are not having zero slope. So both APW and lo are continuous at boundary of sphere, but their first derivatives are discontinuous. The required number of plane waves in the APW+lo basis set is less than the number required in LAPW+LO basis set.

2.1.5.4 Pseudopotential Method

To solve the Schrödinger equation the space can be divided into two regions - region near nuclei is core region which contains core electron and remaining region is valence region containing valence electrons. To describe valence electrons in the interstitial wave-function, few plane waves is enough. But near the core region kinetic energy increases leading to higher oscillating wave function which can not be described with few plane waves. In order to solve this problem Herring in 1940 [53] proposed Orthogonalized Plane Wave (OPW) method [54] where valence wave function is linear combination of plane waves and core states so that the resulting wave function is orthogonal to core state wave function. The Pseudopotential method originated from OPW method. Let us denote the core state and valence state as Ψ_k^c and ψ_k^v respectively. The OPW basis is then given by

$$\phi_k = e^{ik.r} + \sum_c b_c \Psi_k^c(r) \tag{2.79}$$

constant b_c is determined by the condition of orthogonality,

$$\int dr\Psi_k^{c*}(r)\phi_k(r) = 0 \tag{2.80}$$

Then wave function for the system can be written as linear combination of OPWs,

$$\Psi_k = \sum_G c_{k+G}\phi_{k+G} \tag{2.81}$$

where G is reciprocal lattice vectors. The wave function is smoothly varying like plane wave in the interstitial region and rapidly oscillating near core region.

With this basic idea of OPW we can now establish the idea of Pseudopotential.

ϕ_k^v can be written as

$$\phi_k^v(r) = \sum_G C_{k+G}e^{(k+G).r} \tag{2.82}$$

Using Eq.(2.79), it can be written

$$\Psi_k^v(r) = \phi_k^v(r) + \sum_c [\int dr'\Psi_k^{c*}(r')\phi_k^v(r')]\Psi_k^c(r) \tag{2.83}$$

Being exact valence wave function $\Psi_k^v(r)$ satisfies Schorödinger equation

$$H\Psi_k^v(r) = \varepsilon_k^v\Psi_k^v(r) \tag{2.84}$$

Using Eq.(2.83) into Eq.(2.84) and using Schorödinger equation for $\Psi_k^c(r)$

$$H\Psi_k^c(r) = \varepsilon_k^c\Psi_k^c(r) \tag{2.85}$$

along with the potential function

$$V^R\Psi = \sum_c(\varepsilon_k^c - \varepsilon_k^v)(\int dr'\Psi_k^{c*}\Psi)\Psi_k^c \tag{2.86}$$

we have

$$(H + V^R)\phi_k^v = \varepsilon_k^v\phi_k^v \tag{2.87}$$

that is nothing but Schorödinger equation satisfied by ϕ_k^v. The pseudopotential is defined by

$$H + V^R = -\frac{\hbar^2}{2m}V^2 + V^{pseudo} \tag{2.88}$$

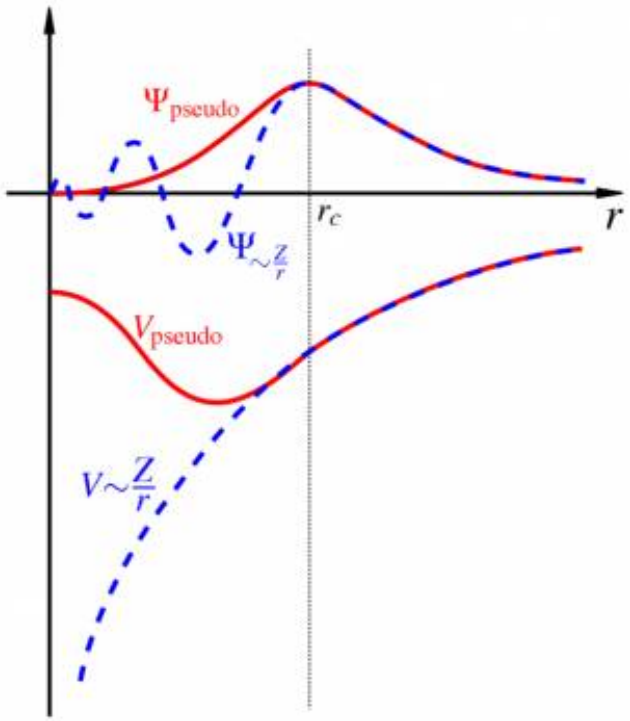

Figure 2.9 The all-electron wave-function and the all-electronic (true) potential(solid lines) plotted against distance r, from the atomic nucleus. The corresponding pseudo-wavefunction and the pseudo-potential are plotted in dotted lines. Outside a given radius r_c , the all-electron and the pseudo-electron wavefunctions match. This figure is adapted from http://en.wikipedia.org/wiki/Pseudopotential.

The main idea of pseudopotential is *replacing strong coulomb potential of the nuclei by an effective ionic potential acting on the valence elctrons*. So, the pseudopotential is an effective potential which represents the balance between attractive potential and repulsive potential V^R as shown in figure[2.8]. The most important point to notice that new valence states ϕ^v, pseudo wave-functions, with the pseudopotential have eigenvalues same as that of original valence

states Φ^v. We have found a new set of valence states that is under a weaker potential close to the nucleus and true ionic potential away from nucleus, beyond cut-off radius r_c . As is known, the region beyond r_c is where electrons interact to form chemical bonds.

After the introduction of initial theory, several attempts have been taken to develop more efficient and accurate pseudopotential method. In norm-conserving pseudopotential method [55], the all-electron (AE) wave-function is replaced by a soft nodeless pseudo (PS) wave-function with the condition that the norm of PS wave function should be same as that of AE wave-function within the chosen core radius and outside the core radius both wave functions are identical. The pseudopotential constructed in this way requires a core radius around the outermost maximum of AE wave function so that charge distribution and moments of AE wave functions are well reproduced by PS wave function. The situation gets complicated when one deals with strongly localized orbitals, e.g., 3d transition metal elements because pseudopotential requires large number of plane waves. Later Vanderbilt improved the formalism by introducing ultra-soft pseudopotential [56] and in this new scheme the norm-conservation constraint was relaxed and localized atom centered augmentation charges were introduced to make up for the charge deficit. These augmentation charges are defined as the charge density difference between the AE and the PS wavefunction, For convenience they allow an efficient treatment of the augmentation charges on a regular grid. Only for the augmentation charges, a small cutoff radius must be used to restore the moments and the charge distribution of the AE wavefunction accurately. Later Blöchl [57] developed the projector-augmented- wave (PAW) method which turns out to be computationally elegant, transferable and accurate method for electronic structure calculation of transition metals and oxides.

2.1.5.5 Projector Augmented Wave Method

In 1994 P. E. Blöchle introduced the projector augmented wave (PAW) method [57] which combines idea from the LAPW method with the plane wave pseudopotential approach. For electronic structure calculation of transition metals and oxides, PAW method turns out to be computationally elegant and accurate. Kresse and Joubert [58] improved the PAW method and implemented in plane wave based code of Vienna Ab initio Simulation Package (VASP). In this formalism all electron wave function Ψ_n is derived from the PS wave function $\tilde{\Psi}_n$ as

$$|\Psi_n\rangle = |\tilde{\Psi}_n\rangle + \sum_i (|\phi_i\rangle - |\tilde{\phi}_i\rangle)\langle \tilde{p}_i|\tilde{\Psi}_n\rangle \tag{2.89}$$

The index i represents the atomic position $\mathbf{R}_i$. The function ϕ_i represents the all electron partial wave and $\tilde{\phi}_i$ represents PS partial wave. These two wave functions match in both value and slope at the boundary r_c. The function $\tilde{p}_i$ is the projector function that satisfies the relation $\langle \tilde{p}_i|\tilde{\phi}_j\rangle = \delta_{ij}$. The all-electron density can be derived using PAW method as

$$n = \tilde{n} + \sum_a (n^a - \tilde{n}^a) \tag{2.90}$$

where the pseudo-charge density $\tilde{n}$ is calculated from PS wave function on plane wave grid. The charge densities n^a and $\tilde{n}^a$ are calculated, for atom a, on logarithmic radial grid. The difference $(n^a - \tilde{n}^a)$ vanishes within the augmentation spheres. In PAW method an additional charge, called compensation charge, is added to the auxiliary charges n^a and $\tilde{n}^a$ to make multipole moments of $(n^a - \tilde{n}^a)$ zero. Similarly the various energy terms can also be expressed as functional of $(n^a, \tilde{n}^a)$ and $\tilde{n}$. In this way we can derive Kohn-Sham equations.

The main advantage of PAW method is that it does not have to deal with inert core electrons. Also valence PS wave functions are smooth and no nodes exist inside the augmentation spheres. Using PAW approach one can access full all-electron density which is very useful for orbital dependent exchange correlation functional.

2.1.6 LDA + U Method

Most well known failure of DFT method is description of Mott insulators. The insulating ground state solution in such materials arises due to the strong Coulomb repulsion between electrons which forces them to localize on atomic-like orbitals (Mott localization) [59]. If the electrons are strongly localized their motions become *correlated* and their wave functions posses marked many-body character. The insulating nature of such materials needs description beyond standard band theory. These materials are called "**strongly-correlated**" materials. The exchange-correlation functional like local density approximation (LDA) or generalized gradient approximation (GGA) fails to predict the insulating character of these materials. Even it predicts unsatisfactory results regarding equilibrium crystal structure, magnetic moments etc.

One of the simplest model developed to justify physics of correlated materials is the Hubbard model [60, 61, 62]. The one band Hubbard model defined on localized orbital basis is given by

$$H_{Hub} = t \sum_{<i,j>,\sigma} (c^{\dagger}_{i,\sigma} c_{j,\sigma} + h.c.) + U \sum_{i} n_{i,\uparrow} n_{i,\downarrow} \tag{2.91}$$

with $< i, j >$ represents nearest-neighbor atoms and $c^{\dagger}_{i,\sigma}$, $c_{j,\sigma}$ and $n_{i,\sigma}$ are the electronic creation operator, electronic annihilation operator and number operators for electrons of spin σ on the i^{th} site. As the electrons are strongly localized the electronic motion is described by the hopping process from one site to nearest-neighbor site whose amplitude t is proportional to the bandwidth of valence electronic states and represents the single-particle term of the total energy. Due to strong localization, Coulomb interaction is taken into account only at the same atomic site through the term proportional to the product of the occupation numbers of atomic states on the same site, whose strength is U. These two parameters t and U are the minimum parameters to describe the Mott insulating physics. In the Mott insulting system the insulating

ground state arises due to dominance of U over t ($U >> t$). The situation when $t >> U$ DFT method is capable of predicting ground state properties of such systems.

To describe the insulating ground state when $U >> t$, the "LDA + U" method was introduced. This method is correction to DFT method for the missing correlation. In the LDA+U formalism the total energy can be expressed as

$$E_{LDA+U}[\rho] = E_{LDA}[\rho] + E_{Hub}[n_{mm'}] - E_{dc}[n] \tag{2.92}$$

where E_{Hub} is the energy due to electron-electron interaction from the Hubbard model. The term E_{dc} is the energy introduced to avoid the *double counting*. Double counting correction is needed because, as we add explicitly the Hubbard term E_{Hub}, we have to remove the energy already included in the LDA. Since the precise localized version of exchange-correlation function within LDA is not available so there are various approximations made to define E_{dc}. The simplest formulation of LDA+U was introduced by Anisimov [63] that can be written as

$$E = E_{LDA} + \sum_I \left[\frac{U^I}{2} \sum_{m,\sigma \neq m',\sigma'} n^I_{m,\sigma} n^I_{m',\sigma'} - \frac{U^I}{2} n^I (n^I - 1) \right] \tag{2.93}$$

In this equation $n^I_{m,\sigma} = n^I_{mm,\sigma}$ and $n^I = \sum_{m,\sigma} n^I_{m,\sigma}$, where n is the occupation number. The index m represents the localized states of site I. The second term in the Eq.(2.93) is the Hubbard term and the third term is the double counting term. Using the definition of occupation number in Eq.(2.93) the Hubbard potential comes out to be non-local.

The orbital energies can be derived from Eq.(2.93) as

$$\varepsilon_m = \frac{\partial E}{\partial n_m} = \varepsilon_{LDA} + U(\frac{1}{2} - n^I_{m,\sigma}) \tag{2.94}$$

This shows that LDA+U formulation shifts the LDA orbital energy by $(-\frac{U}{2})$ for occupied orbital($n_m = 1$) and by $(+\frac{U}{2})$ for unoccupied orbital ($n_m = 0$) (figure[2.8]).

The difference in the energy values of lower and upper Hubbard bands gives the estimate of

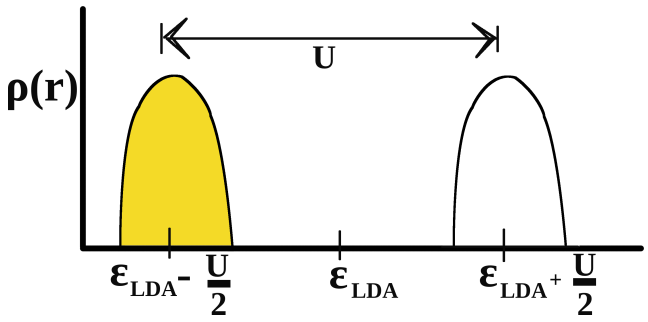

Figure 2.10 Figure is showing splitting of LDA orbital into occupied and unoccupied orbital opening a gap $\sim U$.

energy gap for the system, as shown in Fig. 2.10

2.1.6.1 Rotationally-invariant formulation

The main drawback of the LDA+U formalism, introduced by Anisimov is that the Eq.(2.93) is not invariant under rotation of atomic orbital basis set used to define the occupation of d states. As a consequence the results obtained from this formalism depends on the choice of the localized basis set.

The Lichtenstein method

To solve this drawback A. Liechtenstein and coworkers [64] developed a basis set independent formulation of LDA+U in which the Hubbard term E_{Hub} is given an expression using Hartree-Fock method,

$$E_{Hub}[\left\{n^I_{m,m'}\right\}] = \frac{1}{2}\sum_{m,\sigma,I}[\langle m,m''|V_{ee}|m',m'''\rangle n^{I\sigma}_{m,m'}n^{I-\sigma}_{m'',m'''} + (\langle m,m''|V_{ee}|m',m'''\rangle - \langle m,m''|V_{ee}|m''',m'\rangle)n^{I\sigma}_{m,m'}n^{I-\sigma}_{m'',m'''}] \quad (2.95)$$

where V_{ee} are the screened Coulomb interactions among the nl electrons computed on the wave functions of the localized basis set (e.g., d atomic wave functions) that are labeled by the

index m. The double-counting term E_{dc} is given by

$$E_{dc}[\left\{n^I_{m,m'}\right\}] = \sum_{m,\sigma,I} \left\{ \frac{U^I}{2} n^I(n^I-1) - \frac{J^I}{2}[n^{I,\uparrow}(n^{I,\uparrow}-1) - n^{I,\downarrow}(n^{I,\downarrow}-1)] \right\} \tag{2.96}$$

The atomic (e.g., d or f) states are chosen as localized basis so that the energies can be computed using the expansion of the $\frac{e^2}{|r-r'|}$ Coulomb kernel in terms of spherical harmonics [65].

$$\langle m,m''|V_{ee}|m',m'''\rangle = \sum_k a_k(m,m',m'',m''')F^k \tag{2.97}$$

where k is between 0 and $2l$ (l being angular momentum quantum number). a_k coefficients are derived from products of Clebsh-Gordan coefficients:

$$a_k(m,m',m'',m''') = \frac{4\pi}{(2k+1)} \sum_{q=-k}^{k} \langle lm|Y_{kq}|lm'\rangle \langle lm''|Y^*_{kq}|lm'''\rangle \tag{2.98}$$

where the coefficients F^k are the radial Slater integrals can be obtained from the Coulomb kernel [65]. For d electrons only F^0 , F^2 , and F^4 are required to compute the V_{ee} matrix elements while for f electrons F^6 is required .

The effective Coulomb and exchange interactions, U and J, can be obtained as :

$$U = \frac{1}{(2l+1)^2} \sum_{m,m'} \langle m,m'|V_{ee}|m,m'\rangle = F^0 \tag{2.99}$$

$$J = \frac{1}{2l(2l+1)} \sum_{m,m'} \langle m,m'|V_{ee}|m',m\rangle = \frac{F^2+F^4}{14} \tag{2.100}$$

These equations are often used for the evaluation of Slater integrals using the values of U and J.

The Dudarev method

The LDA+U method introduced by Lichtenstein is based on multi-band Hubbard model. Later a much simpler expression for E_{Hub} is presented by Dudarev et. al. [66]. This simplified expression can be obtained from complete Lichtenstein LDA+U formulation by retaining only

lower order Slater integral F^0 and neglecting other terms: $F^2 = F^4 = J = 0$. Therefore we neglect the non-sphericity of the electronic interactions and also neglect the exchange interaction (J).

The energy functional then can be calculated using the Eq.(2.96) and Eq.(2.97),

$$\begin{aligned} E_U[\{n^{I\sigma}_{mm'}\}] &= E_{Hub}[\{n^{I}_{mm'}\}] - E_{dc}[\{n^{I}\}] \\ &= \sum_{I,\sigma} \frac{U^I}{2} Tr[\mathbf{n}^{I\sigma}(1-\mathbf{n}^{I\sigma})] \end{aligned} \tag{2.101}$$

In the above equation the expression depends on the trace of occupation matrices and of their products which signifies that in the simper formalism the rotational invariance still exist. This simplified version of LDA+U method has been successfully used for most materials where it shows similar results as obtained from the fully rotationally invariant one [cf. Eq.(2.96) and Eq.(2.97)]. Because of the spin-diagonal form of this simplified LDA+U approach, it is customary to attribute the Coulomb interaction U an effective value that accounts for the exchange correction: $U_{eff} = U - J$. [67]

2.2 First Principles Method for Phonons

Phonons are the fundamental particles describing vibrations in solid state materials. They define the properties of solids at finite temperature. Phonons are driving forces for quite a number of phenomena e.g., the thermal expansion, heat conductivity, temperature dependence of mechanical, electric properties, phase transitions. Phonons play a crucial role in a number of microscopic and bulk phenomena such as inelastic coherent and incoherent neutron scattering, coherent inelastic x-ray scattering, inelastic nuclear absorption, infrared absorption, raman scattering etc. So studying phonons is very important for understanding new materials. The theory of the lattice dynamics originates from Born and Huang [68]. It assumes that the

interatomic potential energy is a function of instantaneous position of atomic nuclei.

At T=0, the ground state energy E as a function of atomic positions $\mathbf{R}(\mathbf{n},\mu)$, where $\mathbf{n}$ is the index of primitive unit cell and μ is the atomic index, can be expanded over small displacements $u(\mathbf{n},\mu)$ up to harmonic term. Let us assume that an atom displaces by $u(\mathbf{m},\mu)$. Then the Hellmann-Feynman force on all the other surrounding atoms of the supercell can be expressed as

$$F_i(\mathbf{n},\mu) = -\sum_{\mathbf{m},\nu,j} \Phi_{i,j}(\mathbf{n},\mu,\mathbf{m},\nu)u_j(\mathbf{m},\nu) \tag{2.102}$$

This relation connects the forces on atoms with the force constant matrices, $\Phi_{i,j}(\mathbf{n},\mu,\mathbf{m},\nu)$ and atomic displacement. If we have information regarding forces and atomic displacements we can compute force constant matrix elements $\Phi_{i,j}(\mathbf{n},\mu,\mathbf{m},\nu)$. Subsequently, the dynamical matrix can be defined as

$$\mathbf{D}(\mathbf{k};\mu,\nu) = \frac{1}{\sqrt{m_\mu m_\nu}} \sum_{\mathbf{m}} \Phi_{i,j}(0,\mu;\mathbf{m},\nu) exp(-2\pi i \mathbf{k}\cdot[\mathbf{R}(0,\mu) - \mathbf{R}(\mathbf{m},\nu)]) \tag{2.103}$$

where m_μ and m_ν are the masses of atoms and $\mathbf{k}$ is the wave vector. The summation runs over all primitive cells. The equation of motion of vibrating atoms can be solved by solving eigen-value equation

$$\mathbf{D}(\mathbf{k})\phi(\mathbf{k},j) = \omega^2(\mathbf{k},j)\phi(\mathbf{k},j) \tag{2.104}$$

which gives the phonon frequencies ω and eigenvectors ϕ.

Solution of the eigenvalue equation, using first-principles based method, can be done either by using (a) finite displacements method or (b) density functional perturbation theory (DFPT) method.

2.2.1 Finite Displacement Method

Following this method, first we need to construct a supercell according to our need of high-symmetry $\mathbf{k}$-points for which phonon modes are to be calculated. Phonons are calculated by

diagonalizing the dynamical matrix Eq.(2.103), which contains force constant $\Phi_{i,j}$ which can be obtained, as shown in Fig. 2.11, as

$$\Phi_{i,j}(\mathbf{n},\mu,\mathbf{m},\nu) = -\frac{F_i(\mathbf{n},\mu,u_j(\mathbf{m},\nu))}{u_j(\mathbf{m},\nu))} \tag{2.105}$$

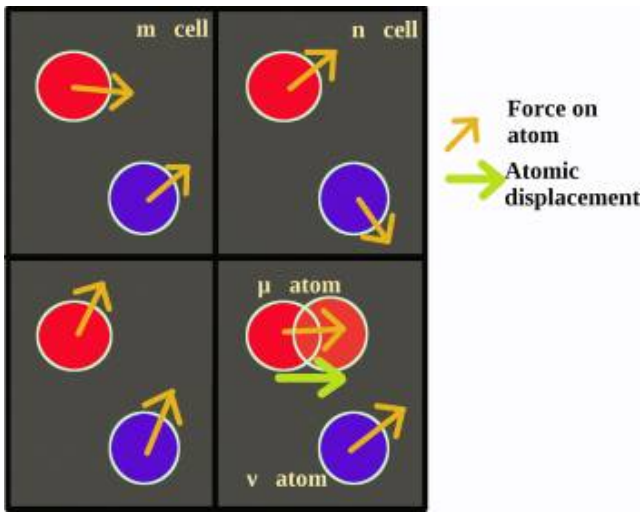

Figure 2.11 Figure is showing supercell containing many primitive cells along with atoms which are displaced by finite amount from their equilibrium position.

In principle, interactions between pairs of atoms at any separations up to the infinite are required. But in practice the non-Coulombic contribution decays rapidly with distance. Furthermore, it can be shown that for a supercell calculations of a dynamical matrix for all atom pairs within one supercell is sufficient to give phonons at all wavevectors commensurate with the supercell. The forces are calculated to include all long-range contributions over other supercells. The calculation of phonons at Γ point (*infrared-active (IR) phonons*) in the Brillouin zone is done with only a single primitive cell.

The dynamical matrix $\mathbf{D}(\mathbf{k})\phi(\mathbf{k},j)$ for the supercell can be determined by making small displacements of one atom at a time, and calculating the Hellmann-Feynman (HF) forces exerted

on all other atoms in the cell. The force constants $\Phi_{i,j}$ then can be calculated using Eq.(2.105). One can use the symmetry elements of the structure to minimize the number of simulation needed for ab initio calculations. Ab initio calculations of phonon frequencies and phonon modes are very useful in predicting macroscopic properties and phase transitions.

2.2.2 Density Functional Perturbation Theory (DFPT)

There are many physical properties which depend on system response to a perturbation. Phonon is one of such properties which depend on the response of the system to a perturbation. Density functional perturbation theory (DFPT) [69, 70] is very powerful and flexible theoretical method that can do calculation of such properties within the density functional framework. Eq.(2.105) can also be written in terms of energy as

$$\Phi_{i,j}(\mathbf{n},\mu,\mathbf{m},\nu) = \frac{\partial^2 E[\{\mathbf{R}\}]}{\partial R_n^\mu \partial R_m^\nu} \tag{2.106}$$

Within the framework of Kohn-Sham DFT the energy functional can be written as

$$E[\{\mathbf{R}\}] = T_0[\rho] + E_{Hartree}[\rho] + E_{xc}[\rho] + E_{ext}[\rho] + E_N(\{\mathbf{R}\}) \tag{2.107}$$

with the constraint that the integral of $\rho(\mathbf{r})$ equals the number of electrons N_e. The first term on right hand side is kinetic energy term, second term is Hartree potential energy, third term is exchange-correlation energy, fourth term is external potential energy due to external potential $V_{ext}(\mathbf{r})$ and the last term is the Madelung energy. The most important consequence of the variational nature of DFT is that the Hellmann-Feynman forces are still valid. The Hellmann-Feynman force in DFT can be expressed as

$$F_I^{DFT} = -\int \rho(\mathbf{r}) \frac{\partial V_{ext}}{\partial R_I} d\mathbf{r} - \frac{\partial E_N}{\partial R_I} - \int \frac{\delta E}{\delta \rho} \frac{\partial \rho}{\partial R_I} \tag{2.108}$$

The last term in the equation vanishes exactly due to the condition that functional derivative of $E[\{\mathbf{R}\}]$ is a constant. Forces in KS-DFT can therefore be calculated from the electron charge-density. The direct calculation of force constant matrix is possible using density functional

perturbation theory (DFPT).

An explicit expression for the force constants can be obtained by differentiating the Hellmann-Feynman forces with respect to atomic coordinates,

$$\frac{\partial^2 E[\{\mathbf{R}\}]}{\partial R_I \partial R_J} = \int \frac{\partial \rho}{\partial R_J} \frac{\partial V_{ext}}{\partial R_I} d\mathbf{r} + \delta_{IJ} \int \rho(\mathbf{r}) \frac{\partial^2 V_{ext}}{\partial R_I \partial R_J} d\mathbf{r} + \frac{\partial^2 E_N[\{\mathbf{R}\}]}{\partial R_I \partial R_J} \tag{2.109}$$

Therefore to calculate the force constant matrix we need to have knowledge of the electronic charge density ρ and its linear response to the distortion of the atomic geometry $\frac{\partial \rho}{\partial R_I}$. The charge density response is calculated by linearizing expression for charge density in terms of Kohn-Sham orbitals, Kohn-Sham eigenvalue equations and the Kohn-Sham effective potential.

$$\frac{\partial \rho}{\partial R_I} = 4Re \sum_{n=1}^{N/2} \psi_n^* \frac{\partial \psi_n}{\partial R_I} \tag{2.110}$$

The index m and n represents quantum numbers.

After linearization we obtain a set of self-consistent linear equations regarding charge-density response and potential response. Efficient iterative algorithms like conjugate gradient or minimal residual methods can be used to obtain solution of the linear system. The first-order perturbation (linear response) theory uses approximation for $\frac{\partial \psi_n}{\partial R_I}$ as given in the following,

$$\frac{\partial \psi_n}{\partial R_I} = \sum_{m \neq n} \psi_m \frac{1}{\varepsilon_n - \varepsilon_m} \left\langle \psi_m | \frac{\partial V_{eff}}{\partial R_I} | \psi_n \right\rangle \tag{2.111}$$

where V_{eff} is the effective Kohn-Sham potential. Using rigorous mathematical treatment the energy functional can be written in terms of perturbing potential and of perturbed Kohn-Sham orbitals. The first-order term gives the Hellmann-Feynman forces. This approach forms the basis for DFPT in which the force constant matrix elements are expressed as minima of suitable functionals.

We have used both finite displacement method and DFPT method for the calculation of phonons in the thesis.

Bibliography

[1] M. Born and J. R. Oppenheimer, Ann. Physik **84,** 457 (1927).

[2] D. R. Hartree, Mathematical Proceedings of the Cambridge Philosophical Society **24,** 89–110 (1928).

[3] D. R. Hartree, Mathematical Proceedings of the Cambridge Philosophical Society **24,** 111–132 (1928).

[4] D. R. Hartree, Mathematical Proceedings of the Cambridge Philosophical Society **24,** 426–437 (1928).

[5] V. Fock, Z. Phys. 61 (1930).

[6] D. MAURICE and M. HEAD-GORDON, Molecular Physics **96,** 1533–1541 (1999).

[7] M. Head-Gordon, R. J. Rico, M. Oumi, and T. J. Lee, Chemical Physics Letters **219,** 21–29 (1994).

[8] J. A. Pople, M. Head-Gordon, and K. Raghavachari, journal of chemical physics **87,** 5968–5975 (1987).

[9] L. H. Thomas, Proceedings of the Cambridge Philosophical Society **23,** 542 (1927).

[10] P. Hohenberg and W. Kohn, Phys. Rev. **136,** B864–B871 (1964).

[11] W. Kohn and L. J. Sham, Phys. Rev. **140,** A1133–A1138 (1965).

[12] http://www.ch.ic.ac.uk/harrison/Teaching/DFT-NATO.pdf .

[13] R. M. Dreizler and E. K. U. Gross, *Density Functional Theory* (Springer, Berlin, 1990).

[14] R. G. Parr and W. Yang, *Density-Functional Theory of Atoms and Molecules* (Oxford University Press, Oxford, 1989).

[15] D. M. Ceperley and B. J. Alder, Phys. Rev. Lett. **45,** 566–569 (1980).

[16] S. H. Vosko, L. Wilk, and M. Nusair, Canadian Journal of Physics **58,** 1200–1211 (1980).

[17] J. P. Perdew and A. Zunger, Phys. Rev. B **23,** 5048–5079 (1981).

[18] J. P. Perdew and W. Yue, Phys. Rev. B **33,** 8800–8802 (1986).

[19] U. v. Barth and L. Hedin, J. Phys. C: Solid State Phys. **5,** 1629–1642 (1972).

[20] S. K. Ma and K. A. Brueckner, Phys. Rev. **18,** 165 (1968).

[21] J. P. Perdew, Phys. Rev. B **33,** 8822 (1968).

[22] J. P. Perdew, Phys. Rev. B **34,** 7406 (1968).

[23] L. D. C. Perdew, John P., , and V. Sahni, Phys. Rev. Lett. **38,** 1030 (1977).

[24] D. J. P. v. O. I. B. Herman, F., Phys. Rev. Lett. **22,** 807 (1969).

[25] D. J. P. v. O. I. B. Herman, F., Phys. Rev. B **28,** 1809 (1983).

[26] J. P. Perdew, Phys. Rev. Lett. **55,** 1665 (1985).

[27] A. D. Becke, Phys. Rev. A **38,** 3098–3100 (1988).

[28] C. Lee, W. Yang, and R. G. Parr, Phys. Rev. B **37,** 785–789 (1988).

[29] C. J. A. M. L. D. Engel, E and V. L. H., Z. Phys. D - Atoms, Molecules and Clusters **23,** 7–14 (1992).

[30] J. P. Perdew, K. Burke, and M. Ernzerhof, Phys. Rev. Lett. **77,** 3865–3868 (1996).

[31] J. C. Slater and G. F. Koster, Phys. Rev. **94,** 1498–1524 (1954).

[32] J. C. Phillips and L. Kleinman, Phys. Rev. **116,** 287–294 (1959).

[33] S. F. Boys, Proc. R. Soc. London Ser. A, Mathematical and Physical **200,** 542–554 (1950).

[34] J. C. Slater, Physical Review **36,** 57–64 (1930).

[35] T. Saha-Dasgupta, , available at `http://www.jncasr.ac.in/cams06/talks/18th_tanusri_mot.pdf`.

[36] E. Wigner and F. Seitz, Phys. Rev. **46,** 509–524 (1934).

[37] T. L. Loucks, *Augmented plane wave method* (W.A. Benjamin, New York, 1967).

[38] J. Korringa, Physica **13,** 392 – 400 (1947).

[39] W. Kohn and N. Rostoker, Phys. Rev. **94,** 1111–1120 (1954).

[40] O. K. Andersen, Phys. Rev. B **12,** 3060–3083 (1975).

[41] O. K. Andersen and O. Jepsen, Phys. Rev. Lett. **53,** 2571–2574 (1984).

[42] O. Jepsen, J. Madsen, and O. K. Andersen, Phys. Rev. B **18,** 605–615 (1978).

[43] P. Blaha, K. Schwarz, G. Madsen, D. Kvasnicka, and J. Luitz, in *WIEN2k, An Augmented Plane Wave + Local Orbitals Program for Calculating Crystal Properties*, K. Schwarz, ed., (Techn. Universität Wien, Austria, 2001).

[44] G. Kresse and J. Hafner, Phys. Rev. B **47,** 558 (1993).

[45] G. Kresse and J. Hafner, Phys. Rev. B **48,** 13115 (1993).

[46] G. Kresse and J. Hafner, Phys. Rev. B **49,** 14251 (1994).

[47] G. Kresse and J. Furthmüller, Phys. Rev. B **54,** 11169 (1996).

[48] O. K. Andersen, O. Jepsen, and M. Sob, , in *Lecture Notes in Physics: Electronic Band Structure and Its Applications* eds.M.Y ussouff (Springer-Verlag, Berlin, 1987).

[49] P. Löwdin, The Journal of Chemical Physics 19 (1951).

[50] O. K. Andersen and T. Saha-Dasgupta, Phys. Rev. B **62,** R16219–R16222 (2000).

[51] O. K. Andersen and T. Saha-Dasgupta, Phys. Rev. B **62,** R16219–R16222 (2000).

[52] D. Singh, Phys. Rev. B **43,** 6388–6392 (1991).

[53] C. Herring, Phys. Rev. **57,** 1169–1177 (1940).

[54] J. Callaway, Phys. Rev. **97,** 933–936 (1955).

[55] D. R. Hamann, M. Schlüter, and C. Chiang, Phys. Rev. Lett. **43,** 1494–1497 (1979).

[56] D. Vanderbilt, Phys. Rev. B **41,** 7892 (1990).

[57] P. E. Blöchl, Phys. Rev. B **50,** 17953 (1994).

[58] G. Kresse and D. Joubert, Phys. Rev. B **59,** 1758–1775 (1999).

[59] I. G. Austin and N. F. Mott, Science **168,** 71–77 (1970).

[60] J. Hubbard, Proc. Roy. Soc. Lond. A **276,** 238–257 (1963).

[61] J. Hubbard, Proc. Roy. Soc. Lond. A **277,** 237–259 (1964).

[62] J. Hubbard, Proc. Roy. Soc. Lond. A **296,** 82 (1966).

[63] V. I. Anisimov, M. A. Korotin, M. Zölfl, T. Pruschke, K. Le Hur, and T. M. Rice, Phys. Rev. Lett. **83,** 364–367 (1999).

[64] V. I. Anisimov, F. Aryasetiawan, and A. I. Lichtenstein, J. Phys.: Condens. Matter **9,** 767–808 (1997).

[65] A. I. Liechtenstein, V. I. Anisimov, and J. Zaanen, Phys. Rev. B **52,** R5467–R5470 (1995).

[66] S. L. Dudarev, G. A. Botton, S. Y. Savrasov, C. J. Humphreys, and A. P. Sutton, Phys. Rev. B **57,** 1505–1509 (1998).

[67] M. Cococcioni and S. de Gironcoli, Phys. Rev. B **71,** 035105 (2005).

[68] I. Waller, Acta Crystallographica **9,** 837–838 (1956).

[69] S. Baroni, P. Giannozzi, and A. Testa, Phys. Rev. Lett. **58,** 1861–1864 (1987).

[70] X. Gonze, Phys. Rev. A **52,** 1086–1095 (1995).

Chapter 3

Study of Spin System YMn_2O_5

3.1 Background

RMn_2O_5[1] (R=Y,Tb,Ho...) series of materials are well-known as improper multiferroic materials due to the coexistence of magnetic as well as ferroelectric order in them [2]. In this class of materials, magnetization acts as primary order parameter and drives the polarization which acts as secondary order parameter, thereby forming the coupling between the two order parameters through magnetoelectric effect. We have focused on a particular compound YMn_2O_5 in this series which is a frustrated spin system. In this chapter we have studied the detailed nature of magnetism of this compound using first-principles based DFT as understanding the magnetism forms a key aspect of this compound. We have computed the magnon dispersion curve using an effective spin Hamiltonian, which is compared with the data obtained from inelastic neutron scattering.

This chapter is based on *Phys. Rev. B 84, 054444 (2011)*

3.2 Introduction

Multiferroic materials attracted attention of scientists for their possible applications like magnetic computer memory which is switchable by electrical field. Transition metal oxide compounds, particularly those with frustrated magnetism [3], often exhibit finite ferroelectric polarization driven by magnetic ordering thereby exhibiting a magnetoelectric coupling. YMn_2O_5 is one such compound in which the primary order parameter is magnetization which drives the polarization. Ferroelectricity in the compound is induced by the frustrated magnetic structures.

It is reported that the compound YMn_2O_5 undergoes a series of magnetic phase transitions upon changing temperature. With the lowering of temperature, at around 44 K temperature, the compound shows transition to an incommensurate antiferromagnetic phase, which is a modulated phase with wave vector $\mathbf{k}$ $(q_x, 0, q_z)$ from the high temperature paramagnetic phase [4]. With further lowering of temperature at around 39 K the incommensurate phase becomes commensurate antiferromagnetic phase with wave vector $\mathbf{k}$ $(\frac{1}{2}, 0, \frac{1}{4})$ with finite ferroelectric polarization along the b-axis [4, 5, 6, 7]. Upon further cooling, at around 19 K, low-temperature incommensurate antiferromagnetic phase with wave vector $\mathbf{k}$ $(0.48, 0, 0.29)$ appears together with reduction in the magnitude of polarization [4, 7, 8].

The set of above mentioned phase transitions appears due to the magnetic frustration of the spins associated with 3d electrons of Mn ions in YMn_2O_5. This also drives ferroelectricity in YMn_2O_5 [9]. Therefore, magnetism is the reason behind almost all the interesting phenomena in this compound. In this context, understanding of magnetic exchange interactions in the Mn sublattice in YMn_2O_5 is important.

$TbMn_2O_5$, another compound in the RMn_2O_5 series, is similar to the YMn_2O_5 compound in terms of crystal structure and magnetic behavior. *Ab initio* total energy method has been used to compute the magnetic exchange interactions in Mn sublattice of the compound $TbMn_2O_5$

by considering few spin configurations [10]. Also, by fitting the experimental inelastic neutron scattering data magnetic exchange interactions have been calculated for YMn_2O_5[11]. However, all these approaches are based on some fitting procedure, either fitting to the energies of spin-configurations or fitting to scattering intensity scanned along specific directions, which may lead to non-uniqueness of fitting parameters. In this study we have employed N^{th} order muffin-tin orbital (NMTO) downfolding method which is capable of estimating effective Mn-Mn hopping integrals and onsite energy values in a first principles way. We have computed the magnetic exchange interactions in YMn_2O_5 from the information of effective Mn-Mn hopping integrals and energy level separations, and employing extended Kugel-Khomskii model[12].

3.3 Crystal Structure

The compound YMn_2O_5 (and $TbMn_2O_5$) has orthorhombic primitive unit cell [see Fig.3.1]. The space group of the compound YMn_2O_5 is Pbam (space group no. 55)[13]. The unit cell contains four formula units, i.e., four Y, eight Mn, twenty O atoms. The compound has complex crystalline structure with two inequivalent Mn sites labeled as Mn1 and Mn2 (four Mn1 and four Mn2 in the unit cell) [Fig.3.1]. There are four inequivalent oxygen atoms labeled as O1, O2, O3 and O4. There are four O1, four O2, four O3 and eight O4 per unit cell [Fig.3.2]. Mn1 ion is surrounded by oxygen atoms which form octahedral coordination environment. On the other hand Mn2 is surrounded by oxygen atoms which form square-pyramidal coordination environment.

To understand the complex crystal structure of the compound we first explain the octahedral and square-pyramidal environment in the following.

$Mn1O_6$ octahedra : There are three inequivalent oxygen atoms O2, O3 and O4 surrounding

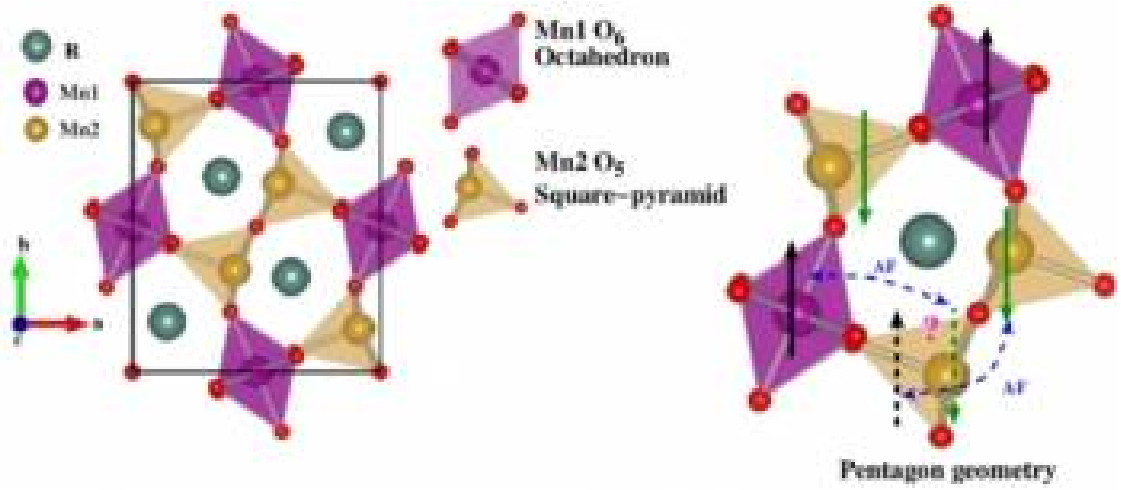

Figure 3.1 The unit cell of YMn_2O_5 projected onto ab-plane is shown on the left panel. The pentagon geometry formed by the connection of Mn1-Mn2-Mn1-Mn2-Mn2 is shown on the right panel. The pentagon geometry gives rise to frustration.

the Mn1 atom. So there are three different bond lengths Mn1-O associated to $Mn1O_6$ octahedra leading to distorted octahedra. The octahedra is connected to the square-pyramid via corner shared oxygen atoms O3 and O4 along approximately a- and b-axis. The octahedra are connected to each other via edge-shared oxygen atoms O2 and O3 along c-axis forming linear chain as shown in Fig.3.2. The edge shared connection of octahedra via O3 is within the unit cell.

$Mn2O_5$ square-pyramid : There are three oxygen atoms O1, O3 and O4 surrounding the Mn2 atom. The square-pyramid is not regular but distorted. The two square-pyramids are connected to each other via edge-shared oxygen atoms O1 at the middle of the unit cell.

Both $Mn1O_6$ and $Mn2O_5$ are linked through edge-sharing and corner-sharing network leading to different magnetic exchange interactions through oxygen mediated super-exchange pathways as shown in Fig. 3.2. The Mn1-Mn2-Mn1-Mn2-Mn2 connection forms a pentagon geometry which gives rise to magnetic frustration due to competitive antiferromagnetic inter-

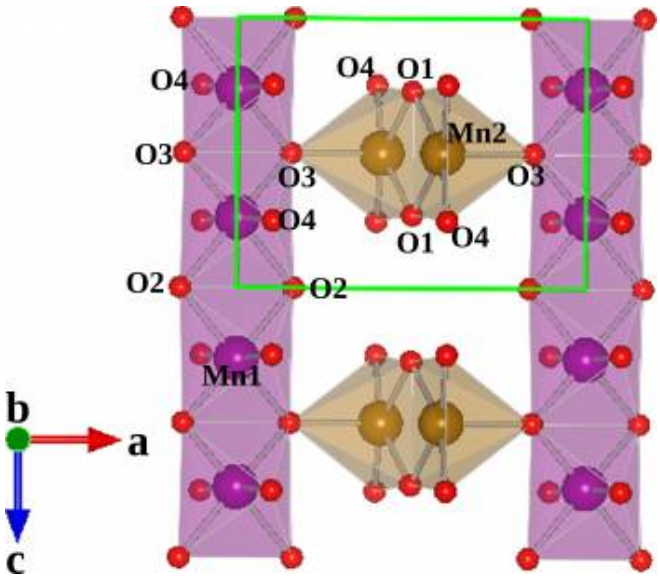

Figure 3.2 $Mn1O_6$ octahedra and $Mn2O_5$ square-pyramids are connected via oxygen atoms. Edge shared octahedra runs along c-axis. The cell is projected onto ac-plane. Various oxygen atoms are labeled according to their positions in the cell surrounding octahedra and square-pyramids.

actions as shown in the right panel of Fig. 3.1. There are two such pentagon geometry in each unit cell as shown in Fig. 3.1. The Y atoms are shown in the Fig. 3.1 by dark-green balls which separate the two Mn1/Mn2 layers.

Experimental data show that the structure of YMn_2O_5 has space group Pbam, which includes spatial inversion (R^{-1}) symmetry. It is surprising that a crystal with inversion symmetry would develop spontaneous polarization. However, sometimes crystal space group can be centrosymmetric but the magnetic space group may not. It might be possible that "electronic" inversion symmetry is broken because of the special magnetic ordering. Then electronic symmetry breaking will further couple to the lattice and lead to lattice distortion. In the ground state spin configuration of YMn_2O_5 due to the spin chain $\cdots$Mn1-Mn2-Mn1$\cdots$ along b-axis the crystal does not possess inversion symmetry (R^{-1}). Therefore, instead of having centrosymmetric structure special magnetic ordering helps to generate large polarization. So, for YMn_2O_5 the actual ground state space-group is suggested to be $Pb2_1m$ [10]. Analysis of phonon modes in

similar compound $TbMn_2O_5$ confirms the spin-configuration to be $Pb2_1m$ [14].

3.4 Results

3.4.1 Basic electronic structure

The electronic structure of the compound YMn_2O_5 is studied by using both LMTO and VASP. In the Fig.3.3 the total density of states (DOS) calculated under spin-polarized situation with GGA approximation is shown. The Fermi energy is set at zero (E_F) of the energy axis. The region near Fermi energy is dominated by Mn1- and Mn2-d orbitals.

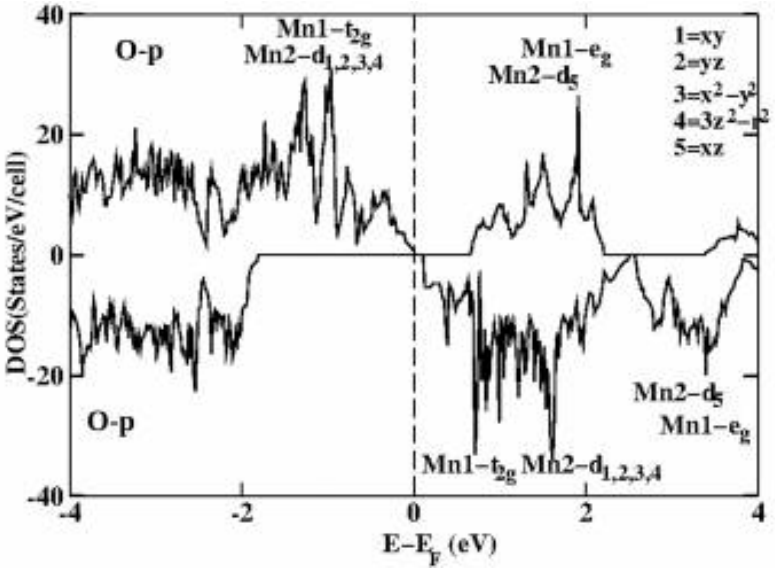

Figure 3.3 Total spin-polarized density of states of YMn_2O_5 calculated under GGA approximation. Dominant contributions of various orbital degrees of freedom are shown in the figure.

Mn-d and O-p hybridized density of states extends from -7.5 eV to 3.5 eV along energy axis. As the Mn1 atom is in the octahedral coordination of oxygens the octahedral crystal field split the Mn1-d into three fold degenerate t_{2g} and two fold degenerate e_g levels. The square-

pyramidal environment split the five Mn2-d levels further as shown in the Fig.3.3. From the DOS we see that in the majority spin channel (upper panel in the Fig.3.3) the Mn1-t_{2g} is completely filled while Mn1-e_g is completely empty. The Mn2-$d_{xy,yz,x^2-y^2,3z^2}$ are completely filled while other are empty. On the other hand, in the minority spin channel in DOS all the Mn1-d and Mn2-d levels are completely empty. There is a finite gap at the fermi level E_F of the order of ~ 0.05 eV resulting an insulating solution. The various orbital contributions are calculated by calculating projected density of states setting local coordinates with z-axis along Mn-O4, y-axis along Mn1-O3 for $Mn1O_6$ octahedra and z-axis along Mn2-O3, y-axis along Mn2-O4 for $Mn2O_5$ square-pyramid.

The spin magnetic moments are also calculated for Mn1 and Mn2 ions under spin-polarized situation which gives $\sim 2.81\ \mu_B$ at Mn1 and $\sim 3.45\ \mu_B$ at Mn2 site.

From both electronic DOS and magnitude of moment values we see the charge disproportionate situation between Mn1 and Mn2 with a nominal valence of Mn^{4+} (d^3) at Mn1 site and Mn^{3+} (d^4) at Mn2 site.

The calculation considering the antiferromagnetic (AF) structure consisting of zigzag AF chains running along the a direction, as described in Ref. [15], further increased the band gap to about 0.7 eV.

3.4.2 Magnetic Model

3.4.2.1 NMTO-downfolding

After the discussion on the basic electronic structure of the compound we move to the study of magnetic exchange interactions in Mn sublattice. To study the magnetic exchange interactions we have used the NMTO-downfolding method as described in the methodology chapter 2.1.5.2. LMTO method is used to do self-consistent calculation to do non-self-consistent elec-

tronic structure. Then starting from self-consistently generated all electron Hamiltonian we construct few band Hamiltonian which involves only Mn-d degrees of freedom employing NMTO-downfolding method. As we already know that NMTO-downfolding method is able to produce few band Hamiltonian by means of energy-selective procedure where it integrates out the degrees of freedom that are not of interest. As we are interested in studying interaction among Mn sites we have kept only Mn-d degrees of freedom in the Hamiltonian and downfolded (integrated out) all other degrees of freedom like O-p, Y-s etc. In this way we construct new basis sets NMTOs which can span only Mn-d dominated states out of all states and nothing else. So effectively NMTOs act as Wannier functions corresponding to Mn-d only Hamiltonian. The tight-binding Hamiltonian defined in the basis of Mn-d Wannier functions provide effective Mn-Mn hopping integrals and onsite energies. As the O-p characters form the tail of downfolded Mn-d only NMTOs, the effective Mn-Mn hopping integrals in the downfolded basis have the chemical information of the hopping path connecting two Mn sites.

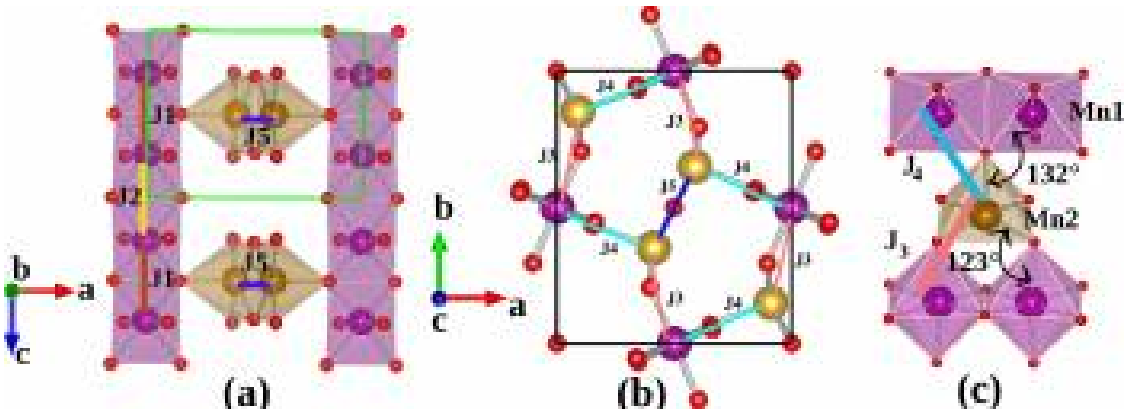

Figure 3.4 (a) The interactions J_1 and J_2 along c-axis. (b) The interactions J_3, J_4 and J_5 in the ab-plane. (c) The difference between J_3 and J_4 interactions comes only due to difference in the angles connecting Mn1 and O and Mn2, which are similar in magnitude.

Direction	O_{Mn1}	Mn1/Mn1	e_{g1}	t_{2g1}	t_{2g2}	e_{g2}	t_{2g3}
		e_{g1}	2.438	0.000	0.000	0.000	0.000
		t_{2g1}	0.000	-0.107	0.000	0.000	0.000
[0.00 0.00 0.00]		t_{2g2}	0.000	0.000	-0.085	0.000	0.000
		e_{g2}	0.000	0.000	0.000	2.534	0.000
		t_{2g3}	0.000	0.000	0.000	0.000	-0.068
Direction	O_{Mn2}	Mn2/Mn2	d_{xy}	d_{yz}	d_{3z^2-1}	d_{xz}	$d_{x^2-y^2}$
		d_{xy}	0.574	0.000	0.000	0.000	0.000
		d_{yz}	0.000	-0.193	0.000	0.000	0.000
[0.00 0.00 0.00]		d_{3z^2-1}	0.000	0.000	0.016	0.000	0.000
		d_{xz}	0.000	0.000	0.000	2.352	0.000
		$d_{x^2-y^2}$	0.000	0.000	0.000	0.000	-0.098

Table 3.1 Onsite energy matrix are represented by O_{Mn1} or O_{Mn2}. The energies are expressed in the unit eV. The directions are given in the unit of lattice constant.

The dominant hopping integrals are estimated to be those connecting Mn1 and Mn2 in the ab-plane, as shown in Fig. 3.4b. The connection of Mn1 and Mn2 is the pentagon as shown in Fig.3.1. The interaction denoted by J_3 (*the pink line in the Fig.3.4b*) is between the Mn1 and Mn2 via corner shared oxygen. The interaction J_4 (*the cyan line in the Fig.3.4b*) is, also, between Mn1 and Mn2 via corner shared oxygen. The only difference between J_3 and J_4 comes from the angle of interaction Mn1$-$O$-$Mn2 which is $\sim 132^\circ$ for J_4 and $\sim 123^\circ$ for J_3 interaction. The interaction J_5 (*blue line in the Fig.3.4b*) involves Mn2 sites only via edge shared oxygen atoms at the middle of the cell. There are out of plane interactions along c-axis J_1 (*brown line in Fig.3.4a*) and J_2 (*yellow line in Fig.3.4a*) connecting $Mn1O_6$ octahedra via edge shared oxygen atoms forming linear chain $\cdots$-J_1-J_2-J_1-J_2-$\cdots$. The Mn1-Mn2 distance differentiates among J_1 and J_2 interactions.

Table 3.1 shows the onsite energies at Mn1 and Mn2 sites as obtained from NMTO-downfolding method. The states at Mn1 site are grouped together into t_{2g}'s and e_g's with tiny energy difference $\sim 0.02-0.1$ eV within themselves. The states at Mn2 site can be arranged according to increasing energies as d_{yz}, $d_{x^2-y^2}$, d_{3z^2-1}, d_{xy} and d_{xz} with small energy difference between d_{yz}, $d_{x^2-y^2}$, d_{3z^2-1}.

Once we have the hopping integral values and onsite energy values we can use them within the extended Kugel-Khomskii-like model. The procedure is explained in the following considering the example of the exchange interaction connecting Mn1 and Mn2. To calculate exchange interaction we employ extended Kugel-Khomskii-like model where we take difference of energy costs for hopping of electrons from Mn1 to Mn2 site for parallel and anti-parallel alignment of spins.

The expression for the energy cost for hopping of electrons corresponding to parallel align-

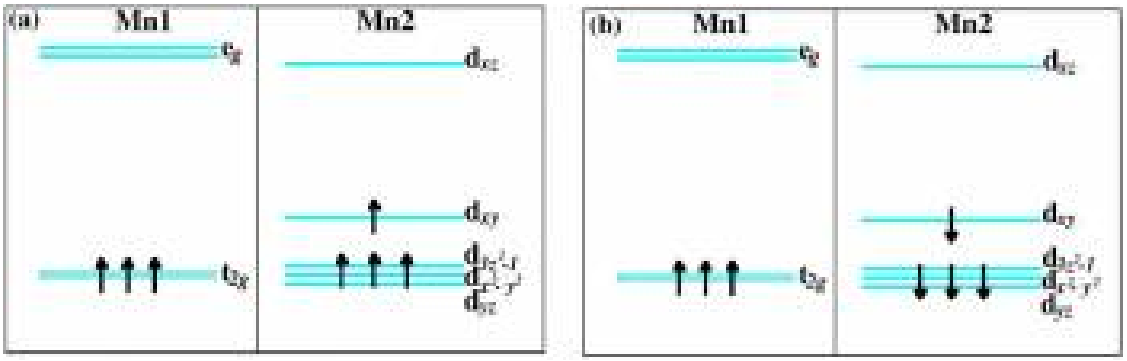

Figure 3.5 Superexchange processes connecting Mn1 and Mn2 [left panel and right panel]. The diagrams represent exchange interactions J_3 and J_4.

ment of spins at Mn1 and Mn2 sites is given by

$$\Delta E^{Mn1-Mn2}_{Ferro} = -\sum_{l=1}^{3}\frac{2t^2_{l,d_{xz}}}{U-J_H+\Delta_{l,d_{xz}}} - \sum_{r=1}^{4}\sum_{eg}\frac{2t^2_{r,e_g}}{U-J_H+\Delta_{r,e_g}} \quad (3.1)$$

$$\Delta E^{Mn1-Mn2}_{Antiferro} = -\sum_{l=1}^{3}\sum_{p=1}^{5}\frac{2t^2_{l,p}}{U+\Delta_{l,p}} - \sum_{r=1}^{4}\sum_{eg}\frac{2t^2_{r,e_g}}{U+\Delta_{r,e_g}} \quad (3.2)$$

where, the summation over l, r and e_g in the first expression runs over three t_{2g} states at Mn1 site, d_{yz}, $d_{x^2-y^2}$, $d_{3z^2-r^2}$, d_{xy} states at Mn2 site, and two e_g states at Mn1 site respectively. Similarly, the summation over l, p, r and e_g in the first expression runs over three t_{2g} states at Mn1 site, five d states at Mn2 site, d_{yz}, $d_{x^2-y^2}$, $d_{3z^2-r^2}$, d_{xy} states at Mn2 site, and two e_g states at Mn1 site respectively. The magnetic exchange interactions calculated using NMTO-downfolding method are compared with the results reported for similar compound $TbMn_2O_5$ in the literature [10] in the Table 3.2. The comparison of the exchange interactions for YMn_2O_5 with those for $TbMn_2O_5$ are well justified because of the fact that the two compounds have the similar crystal structure and magnetic behavior. Use of Kugel-Khoskii model requires knowledge of values of Hubbard U and Hund's coupling J_H. We have used U to be 5 eV and J_H to be 1 eV. All the in-plane exchange interactions are found to be antiferromagnetic. Only in-plane interactions are shown in the Table 3.2 because the dominant interactions are in-plane interactions and the out-of-plane interactions (J_1 and J_2) are very weak in magni-

	J_3	J_4	J_5
NMTO-downfolding	-4.15	-4.61	-1.63
Wang *et al.*	-0.45	-4.92	-1.85

Table 3.2 Magnetic exchange interactions (in meV), J_3, J_4 and J_5 computed using the extended Kugel-Khomskii model and NMTO-downfolding derived on-site energies and hopping matrix elements, as compared to that computed by Wang *et al.*[10] for $TbMn_2O_5$.

tude compared to the in-plane interactions. Furthermore, we need to compare the results with the results already reported in the literature [10] where the out-of-plane interactions are even neglected without calculating their numerical values. Comparing the two parameter sets, as shown in Table 3.2, we find that both approaches give J_4 to be strongest interaction with J_5 about a third of J_4. J_3, on the other hand, is reported to be much weaker compared to J_4 in the reference [10] while NMTO-downfolding approach gives its magnitude to be comparable to J_4. NMTO-downflding method is giving $J_3/J_4 \sim 0.9$ while the reported values in reference [10] gives $J_3/J_4 \sim 0.09$.

3.4.2.2 Total energy calculation

In order to understand the origin of difference in exchange interactions in different approaches, we explored energetics of the spin configurations in more detail. For this we have considered $2\times1\times1$ supercell with 16 Mn atoms which gives rise to 2^{16} possible spin-configurations. The magnetic unit cell together with the atoms labeled with numbers are shown in the figure 3.6. Considering the Heisenberg Hamiltonian description of the spin configurations we found that out of all possible spin-configurations, only 166 spin-configurations are energetically non-degenerate. On the other hand, Wang *et. al* considered only eight spin-configurations to fit their energies to the energies of the Heisenberg Hamiltonian formed out of Mn spins. In this

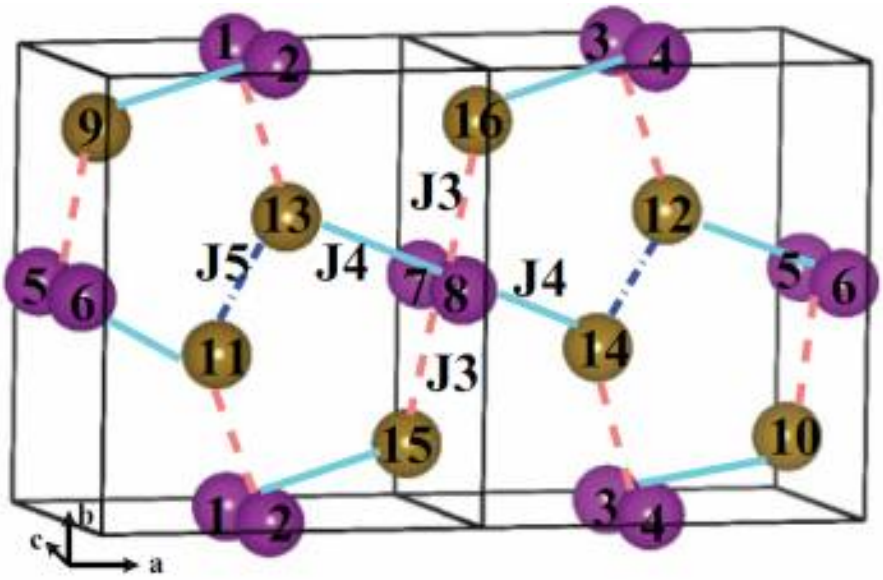

Figure 3.6 The magnetic unit cell considered for total energy calculations of different magnetic configurations. Different Mn atoms have been numbered.

procedure of estimating magnetic exchange interactions, known as *total energy method*, the LDA total energies of various spin-configurations are fitted to the energies of the Heisenberg Hamiltonian made up of Mn spins. A few representative results are presented in the Table 3.3. Considering different sets of spin configurations to extract J's we find the results to depend sensitively on choice of spin configurations. For example, one subset of results (*the first two panels in Table 3.3*) are Wang *et. al.* like giving $J_3 \ll J_4$ while other subsets of results (*the other two panels in Table 3.3*) are NMTO-like giving $J_3 \simeq J_4$. This points to the nonuniqueness of the parameter sets obtained from fitting of total energies.

To check the influence of J's on properties we calculated the magnon spectra as presented in the following subsection.

		1	2	3	4	5	6	7	8	9	10	11	12	13	14	15	16	$\triangle E$
	FM	+	+	+	+	+	+	+	+	+	+	+	+	+	+	+	+	0
Wang *et. al.*	AFM1	-	-	-	-	+	+	+	+	+	+	+	+	+	+	+	+	281
like	AFM2	+	+	+	-	-	-	-	+	+	+	+	-	-	-	-	+	-4
	AFM3	-	+	+	+	+	-	-	-	-	+	+	+	-	-	-	-	62
Exchange Integral (meV)		J_3 =-0.17					J_4 =-3.19					J_5 =-1.16						
		1	2	3	4	5	6	7	8	9	10	11	12	13	14	15	16	$\triangle E$
	FM	+	+	+	+	+	+	+	+	+	+	+	+	+	+	+	+	0
Wang *et. al.*	AFM1	-	-	-	-	+	+	+	+	+	+	+	+	+	+	+	+	281
like	AFM2	+	+	+	-	-	-	-	-	-	+	+	+	+	+	+	-	-151
	AFM3	-	-	+	-	+	-	+	+	-	+	-	+	-	+	+	-	12
Exchange Integral (meV)		J_3 =-0.50					J_4 =-3.40					J_5 =-1.01						
		1	2	3	4	5	6	7	8	9	10	11	12	13	14	15	16	$\triangle E$
	FM	+	+	+	+	+	+	+	+	+	+	+	+	+	+	+	+	0
NMTO like	AFM1	-	-	-	-	+	+	+	+	+	+	+	+	+	+	+	+	281
	AFM2	+	+	+	-	-	-	+	+	+	-	-	-	+	+	+	-	270
	AFM3	+	-	-	-	-	+	+	+	-	-	-	-	+	+	+	-	187
Exchange Integral (meV)		J_3 =-3.92					J_4 =-4.33					J_5 =-1.31						
		1	2	3	4	5	6	7	8	9	10	11	12	13	14	15	16	$\triangle E$
	FM	+	+	+	+	+	+	+	+	+	+	+	+	+	+	+	+	0
NMTO like	AFM1	-	-	-	-	+	+	+	+	+	+	+	+	+	+	+	+	281
	AFM2	-	-	-	-	+	+	+	+	+	+	-	-	-	-	-	-	24
	AFM3	-	+	-	+	+	-	+	-	+	-	+	-	+	-	+	+	23
Exchange Integral (meV)		J_3 =-3.73					J_4 =-4.19					J_5 =-1.44						

Table 3.3 Few representative spin-configurations out of all possible spin-configurations for Mn spins. The upper two panels are representative sets giving results similar to those reported in Wang *et. al.*[10] while lower two panels give results similar to those obtained from NMTO-downfolding method. The numbers $1-16$ in the Table represent 16 Mn ions in the supercell.

3.4.3 Magnon dispersion

To calculate the magnon spectra, we first constructed a spin model corresponding to the ground state spin-configuration as shown in the Fig.3.7.

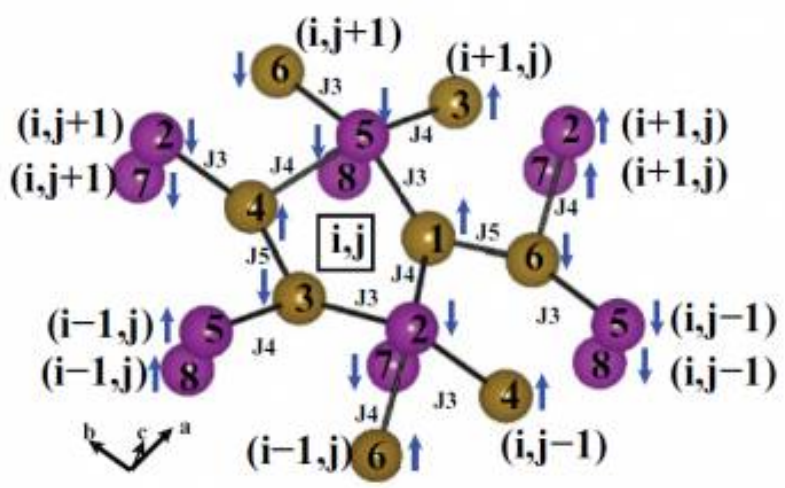

Figure 3.7 The spin model considering the ground state spin configuration for YMn_2O_5.

We used Holstein-Primakoff transformation [16] to convert from spin to boson representation. We diagonalized the constructed matrix using numerical implementation of Bogolubov transformation [17]. In this technique as input we need magnetic exchange parameters. We have considered the magnetic exchange interactions restricted only within the magnetic cell shown in Fig.3.7. There are four interactions J_1, J_3, J_4 and J_5 within the cell. The parameter set calculated by Wang *et. al.* [10] did not consider J_1. However, in order to stabilize the ground state commensurate spin-configuration as reported in reference [6] we have taken into account J_1 only. J_1 comes out to be ferromagnetic in nature with magnitude of $J_1 \approx 0.5\ J_4$ from NMTO-downfolding calculation. The ordering of the magnetic configurations for our case is (1/2,0,0) instead of (1/2,0,1/4) as observed experimentally because we have neglected

out-of-plane interactions beyond J_1.

The spin Hamiltonian defined in the magnetic cell is $H = H_{intra} + H_{inter}$, where

$$\begin{aligned} H_{intra} &= \sum_{ij} J_5(S_{3,i,j}\cdot S_{4,i,j} + S_{1,i,j}\cdot S_{6,i,j}) \\ &+ J_3(S_{2,i,j}\cdot S_{3,i,j} + S_{1,i,j}\cdot S_{5,i,j}) \\ &+ J_4(S_{4,i,j}\cdot S_{5,i,j} + S_{1,i,j}\cdot S_{2,i,j}) \\ &+ J_1(S_{2,i,j}\cdot S_{7,i,j} + S_{5,i,j}\cdot S_{8,i,j}) \\ &+ (J_4 S_{1,i,j}\cdot S_{7,i,j} + J_3 S_{3,i,j}\cdot S_{7,i,j}) \\ &+ (J_3 S_{1,i,j}\cdot S_{8,i,j} + J_4 S_{4,i,j}\cdot S_{8,i,j}) \end{aligned}$$

while

$$\begin{aligned} H_{inter} &= \sum_{ij} J_3(S_{4,i,j}\cdot S_{2,i,j+1} + S_{5,i,j}\cdot S_{6,i,j+1}) \\ &+ J_4(S_{5,i,j}\cdot S_{3,i+1,j} + S_{6,i,j}\cdot S_{2,i+1,j}) \\ &+ J_3(S_{6,i,j}\cdot S_{5,i,j-1} + S_{2,i,j}\cdot S_{4,i,j-1}) \\ &+ J_4(S_{2,i,j}\cdot S_{6,i-1,j} + S_{3,i,j}\cdot S_{5,i-1,j}) \\ &+ (J_4 S_{3,i,j}\cdot S_{8,i-1,j} + J_3 S_{4,i,j}\cdot S_{7,i,j+1}) \\ &+ (J_3 S_{6,i,j}\cdot S_{8,i,j-1} + J_4 S_{6,i,j}\cdot S_{7,i+1,j}) \\ &+ (J_4 S_{7,i,j}\cdot S_{6,i-1,j} + J_3 S_{7,i,j}\cdot S_{4,i,j-1}) \\ &+ (J_3 S_{8,i,j}\cdot S_{6,i,j+1} + J_4 S_{8,i,j}\cdot S_{3,i+1,j}) \end{aligned}$$

where H_{intra} is the Hamiltonian corresponding to the interactions restricted to the central cell i, j, while H_{inter} is the Hamiltonian corresponding to interactions connecting sites within i, j cell to neighboring cells. $S_{n,i,j}$ is the spin at n^{th} Mn site within the cell i, j. The atoms labeled as $1-8$ in the Fig.3.7 are the basis of the cell labeled as i, j. The neighboring unit cells are labeled as $i \pm 1, j$ or $i, j \pm 1$.

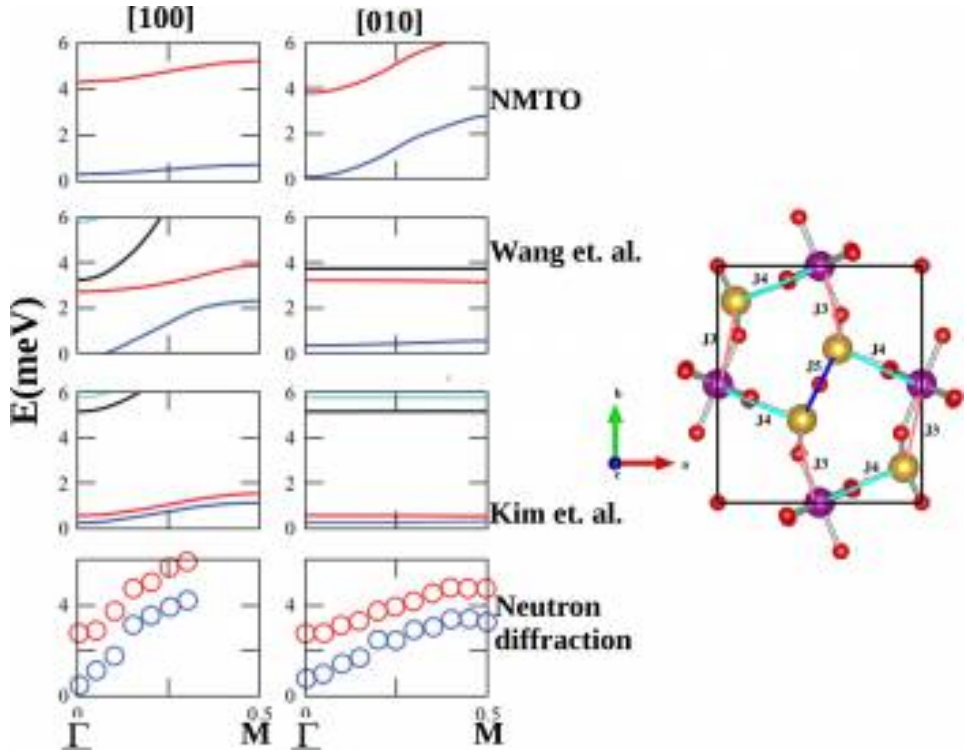

Figure 3.8 The Magnon dispersion curves are shown along [100] and [010] directions. The unit cell along with J's is also shown on right hand side of the figure to show that [100] is approximate direction of J_3 and [010] is approximate direction of J_4.

We have computed the magnon dispersion along the direction [100] and [001]. Magnon dispersion is calculated considering the exchange parameters as obtained from NMTO-downfolding method, as given values of Wang et. al. [10] and also that given by Kim *et. al.* [11]. The computed magnon dispersion is compared with the magnon dispersion measured by inelastic neutron scattering experiment. The comparison is shown in the Fig.3.8.

The top most panels of Fig.3.8 show the magnon curves calculated using J values obtained from NMTO-downfolding method. The second panels from the top show magnon curves calculated from J values reported by Wang *et. al.*. The third panels show magnon curves calculated using J values reported by Kim *et. al.*. The bottom panels show the experimentally

measured dispersions. All of the calculated magnon dispersion curve has eight branches, due to the multi-atom basis in the unit cell [18]. The experimental spectra captures only the lowest two branches, the higher ones are not captured due to the instrumental limitations of the cold triple-axis spectrometer. In Fig. 3.8 we have shown only the lowest branches of calculated magnon curves for the sake of comparison with experimental curves.

Considering Fig. 3.8, we notice that while the theoretically calculated dispersions along [100] differ from experiment for all chosen parameter sets, the theoretical results obtained using NMTO-derived parameter sets, along [010] are in much better agreement with the experiment, compared to other parameter sets. The parameter set of Wang et al.,[10] shows no dispersion at all along the [010] direction, in sharp contrast with the experimentally measured data. We note, that the vector connecting Mn1 and Mn2 sites, corresponding to J_3 interaction is primarily directed along the b direction, while the vector connecting Mn1 and Mn2 sites, corresponding to J_4 interaction is primarily directed along the a direction (cf. Table 3.1). The lack of dispersion of the magnon modes along the [010] direction considering the parameter sets given by Wang et al.'s total energy calculations [10] is therefore expected as the value of the parameter J_3 was rather small in Wang et al.'s parameter set [10]. The value of the parameter J_3 was also small in the parameter set of Kim et al.,[11] producing also dispersionless magnon spectra along [010] direction. We note that the measured magnon spectra of YMn_2O_5 in the low-temperature incommensurate state at higher energies ($10-20$ meV), to which the fit was carried out by Kim et al. [11] did not involve the dispersions along [010] direction. The improvement of the description of dispersion along [010] direction using NMTO-derived parameters, therefore, shows a clear evidence of the superiority of the NMTO-derived parameter sets over the existing parameter sets with small values of J_3. [10, 11] Finally, though the NMTO-downfolding-derived parameter sets capture the behavior of the experimental spectra along [010] direction satisfactorily, the description along [100] direction is still not satisfac-

tory. This may be due to the neglect of magnon-phonon interactions, which are shown to be important in these systems [18] as well as neglect of single-ion anisotropy in the model, responsible for the helicoidal modulation in experimentally observed spin structure. Inclusion of magnon-phonon interaction through phonon calculations for different magnetic configurations is prohibitively difficult and will be taken up at a later date. At the end, it is interesting to note that in spite of the simplistic nature of our spin model, it brings out nicely the importance of the magnetic exchange interaction, J_3.

3.4.4 Chemical point of view : Wannier function

Having established the goodness of the NMTO-derived parameter set with substantially large value of magnetic exchange interaction J_3 in terms of the calculated magnon spectra and its comparison with inelastic-neutron-scattering data, we provide further arguments based on the involved superexchange paths. As found by the NMTO study, the magnitude of J_3 is comparable to that of the largest interaction, J_4, while the previous studies [10, 11] report substantially smaller value of J_3 compared to J_4. We argue in the following that from a chemical point of view, it is logical to have J_3 comparable to J_4. It might be noted that both J3 and J4 interactions connect a pair of Mn1 and Mn2 sites through corner-shared oxygens, with a very similar Mn-O-Mn bond angle (123° for J_3 and 132° for J_4 interaction). One would, therefore, expect the involved superexchange paths to be similar in two cases, giving rise to a similar nature of magnetic exchanges.

This expectation turned out to be true as shown in Fig. 3.9, where the overlap of two representative Mn-d Wannier functions placed at Mn1 and Mn2 sites have been plotted, corresponding to interactions "3" (left panel) and "4" (right panel) respectively. It shows in both cases that the overlap of the Wannier functions centered at Mn1 and Mn2 sites gives rise to equally strong superexchange paths formed by the overlap of weights situated at the connecting oxygen site.

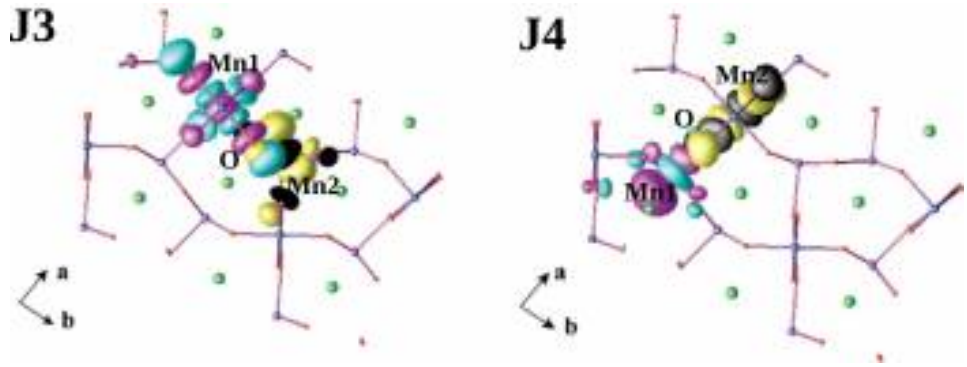

Figure 3.9 The Mn-d Wannier functions are plotted along directions of exchange interactions J3 (left panel) and J4 (*right panel*).

3.5 Conclusion

To understand the magnetic interactions we have employed the first principle based methods along with the model Hamiltonian calculation for the compound YMn_2O_5. Our results highlights few important magnetic exchange interactions which play an important role in the magnetism of the compound. In this respect, our results differ from the results reported earlier [10] for the related compound $TbMn_2O_5$ using total energy calculation and that obtained by fitting the inelastic-neutron-scattering data for the low-temperature incommensurate phase of YMn_2O_5 [11]. Our first-principles derived parameters reproduce the magnon dispersion curves along [010] direction as observed by inelastic-neutron-scattering experiment for commensurate phase. This justifies the importance of the J_3 interaction in the magnetism of the compound as pointed out in our calculation. The agreement of the calculated magnon dispersion along [100] is not in satisfactory agreement with the experimental dispersion. This may further be improved by including lattice contribution through the spin-phonon coupling effect.

Bibliography

[1] S.-W. Cheong and M. Mostovoy, Nature Materials **6,** 13–20 (2007).

[2] W. Eerenstein, N. D. Mathur, and J. F. Scott, Nature **442,** 759–765 (2006).

[3] T. Kimura, T. Goto, H. Shintani, K. Ishizaka, T. Arima, and Y. Tokura, Nature **426,** 55–58 (2003).

[4] I. Kagomiya, H. Kimura, Y. Noda, and K. Kohn, J. Phys. Soc. Jpn. **70,** 145 (2001).

[5] Y. Noda *et al.*, Physica B **119,** 385–386 (2006).

[6] C. Vecchini, L. C. Chapon, P. J. Brown, T. Chatterji, S. Park, S.-W. Cheong, and P. G. Radaelli, Phys. Rev. B **77,** 134434 (2008).

[7] Y. Noda, Y. Fukuda, H. Kimura, I. Kagomiya, S. Matumoto, K. Kohn, T. Shobu, and N. Ikeda, J. Korean Phys. Soc. **42,** 1192 (2003).

[8] P. G. Radaelli, C. Vecchini, L. C. Chapon, P. J. Brown, S. Park, and S.-W. Cheong, Phys. Rev. B **79,** 020404 (2009).

[9] S. Partzsch, S. B. Wilkins, J. P. Hill, E. Schierle, E. Weschke, D. Souptel, B. Büchner, and J. Geck, Phys. Rev. Lett. **107,** 057201 (2011).

[10] C. Wang, G.-C. Guo, and L. He, Phys. Rev. B **77,** 134113 (2008).

[11] J.-H. Kim, M. A. van der Vegte, A. Scaramucci, S. Artyukhin, J.-H. Chung, S. Park, S.-W. Cheong, M. Mostovoy, and S.-H. Lee, Phys. Rev. Lett. **107,** 097401 (2011).

[12] K. I. Kugel and D. I. Khomskii, Soviet Physics Uspekhi **25,** 231 (1982).

[13] G. R. Blake, L. C. Chapon, P. G. Radaelli, S. Park, N. Hur, S. W. Cheong, and J. Rodríguez-Carvajal, Phys. Rev. B **71,** 214402 (2005).

[14] L. C. Chapon, G. R. Blake, M. J. Gutmann, S. Park, N. Hur, P. G. Radaelli, and S.-W. Cheong, Phys. Rev. Lett. **93,** 177402 (2004).

[15] C. Vecchini, L. C. Chapon, P. J. Brown, T. Chatterji, S. Park, S.-W. Cheong, and P. G. Radaelli, Phys. Rev. B **77,** 134434 (2008).

[16] C. Kittel, *Quantum Theory of Solids* (Wiley, New York, 1987).

[17] Y. Watabe, T. Suzuki, and Y. Natsume, Phys. Rev. B **53,** 459–459 (1996).

[18] K. Cao, G.-C. Guo, D. Vanderbilt, and L. He, Phys. Rev. Lett. **103,** 257201 (2009).

Chapter 4

Study of Unusual Insulating Phase in Double Perovskite Compound La_2CoMnO_6

4.1 Background

The perovskite structure ABX_3, where A is non-magnetic cation, B is magnetic cation and X is an anion, have generated long standing interest due to their subtle variations in the crystal structures and its effect on their physical properties. Double perovskites are the derivative of perovskite compounds. Substitution of cation B' for B leads, in general, to the solid solution $AB_{1-x}B_{x'}X_3$. When x=0.5 and B' and B are sufficiently different in charge and/or size, the B-cation ordering may be achieved, with B' and B having rock-salt ordering. The formula for ordered double perovskite structure can be written as $A_2BB'X_6$. In this chapter we have studied electronic structure of a double perovskite compound La_2CoMnO_6, which is reported to

This chapter is based on *Phys. Rev. B 84, 035131 (2011)*

be ferromagnetic insulator with a T_c of 240 K [1]. Ferromagnetic insulators are rare in nature. Even it is very rare to find ferromagnetic insulators with relatively high Curie temperature. There are very few known examples like, EuO ($T_c \sim 77$ K)[2], $CdCr_2S_4$ ($T_c \sim 90$ K)[3] have Curie temperature much below room temperature.

4.2 Introduction

The double perovskite compound La_2CoMnO_6 (LCMO) has been synthesized with ordered arrangement of 3d transition metals Co and Mn [4]. The compound is reported to be ferromagnetic Curie temperature $T_c \sim 240$ K for the perfectly ordered Co/Mn phase [5]. For the disordered Co\Mn phase the Curie temperature is $T_c \sim 150$ K along with spin-glass like behavior. There has been a long debate about the precise valence of Co and Mn ions. X-ray absorption spectroscopy (XAS) as well as X-ray absorption near-edge spectroscopy (XANES) experiments [4, 6] have confirmed that in the ordered phase the precise valence of Co and Mn are 2+ (d^7) and 4+ (d^3) respectively, while for disordered phase valences of Co and Mn are 3+ and 3+ respectively. X-ray photoemission experiment on the thin film of LCMO reported total magnetic moment to be 5.7 μ_B per *f.u.* with high spin states for Co^{2+} and Mn^{4+} [7]. Using Hund's rule arranging spins associated with valence electrons at Co and Mn ions at the 3d-levels it leads to the partially filled situation at Co site, as shown in Fig.4.1. Octahedral surrounding of oxygen atoms around Mn and Co, Fig.4.2, split the Co and Mn 3d states into three fold degenerate t_{2g} and two fold-degenerate e_g level.

The high spin configuration of Co^{2+} is thus given by ($t_{2g}^3(\uparrow)$, $t_{2g}^2(\downarrow)$, $e_g^2(\uparrow)$) and Mn^{4+} is given by ($t_{2g}^3(\uparrow)$). This leads us to the conclusion of metallic state for the compound LCMO which does not agree with the experimental observation of insulating solution. Although, for

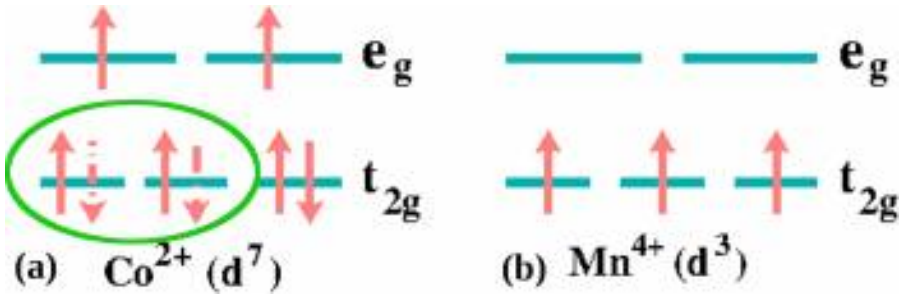

Figure 4.1 (a) Spin arrangement of seven valence electrons at Co site using Hund's rule. The dotted down spin (↓) inside the green circled region is representing the partially filled situation. (b) The spin arrangement of three valence electrons at Mn site using Hund's rule.

Atoms	Wykoff positions	x	y	z
La	2c	0.25019	0.25019	0.25019
Co	1a	0.0	0.0	0.0
Mn	1b	0.5	0.5	0.5
O	6f	0.80604	0.68227	0.25783

Table 4.1 Relaxed atomic coordinates of LCMO obtained keeping the lattice constants fixed at experimental values.

a similar compound La_2NiMnO_6 [8] the insulating phase is obvious because of the spin configuration for Ni^{2+} is $3d^8$ ($t_{2g}^3(\uparrow)$, $t_{2g}^3(\downarrow)$, $e_g^2(\uparrow)$) and for Mn^{4+} is $3d^3$ ($t_{2g}^3(\uparrow)$). This situation generates curiosity to find the origin of insulating phase.

There is, also, report of magnetocapacitive behavior in the ordered phase of LCMO [9, 10, 11]. Therefore, we have carried out first-principles DFT study of the electronic structure and phonon modes to shed light on the curious insulating behavior of the compound as well as the magnetocapacitive behavior.

4.3 Crystal Structure

The rhombohedral unit cell of LCMO having lattice constant of 5.488 Åand 1 f.u. in the unit cell is shown in Fig. 4.2. In view of the fact that the positions of light atoms such as O, may not be well characterized within the experimental technique, we have carried out structural optimization where the internal degrees of freedom associated with La and O atoms have been optimized keeping the lattice parameters fixed at experimentally determined values.[12] The relaxed structural parameters of the rhombohedral phase (see Table 4.1) agree well within less 1% with experimental ones. In the optimized structure, the CoO_6, and MnO_6 octahedra are regular having equal lengths of all Co−O and Mn−O bonds. The CoO_6, and MnO_6 octahedra though exhibit trigonal distortion, with O−Co−O angles and O−Mn−O angles differing from 90°. For CoO_6 octahedra, they differ by 1.31° while for MnO_6 octahedra, they differ by 1.34°. The Co−O−Mn angle is 160.02°, deviating significantly from 180° linear Co−O−Mn situation.

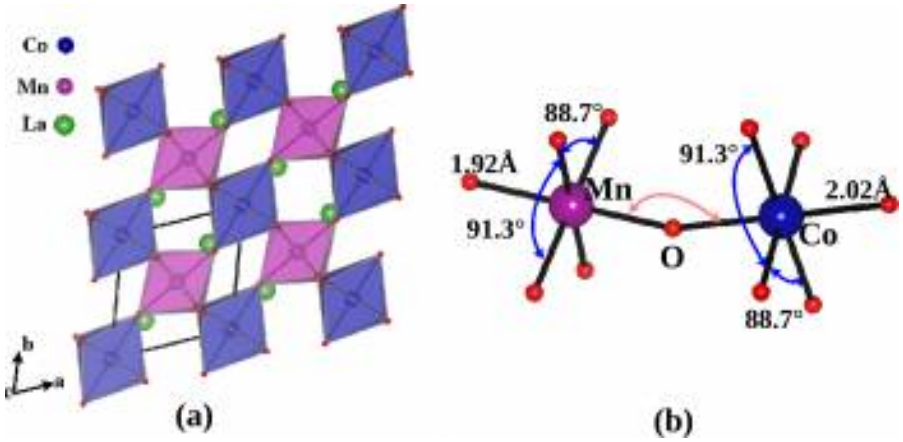

Figure 4.2 (a) The Rhombohedral unit cell of the compound La_2CoMnO_6 is shown by dark solid line. (b) The octahedra of CoO_6 and MnO_6 with trigonal distortion.

4.4 Electronic structure

The spin-polarized density of states (DOS) calculated within GGA approximation in LAPW basis is shown in the left panel of Fig. 4.3. As we see, the electronic structure calculated within GGA approximation gives rise to a half-metallic solution, with a gap in the majority spin channel and finite density of states at the Fermi energy, E_F. In the minority spin channel, the transition metal d-oxygen p hybridized DOS extends from an energy range about -7 eV below E_F to about 4 eV above E_F. While the low lying states occupying an energy range from about -7 eV to about -4 eV or -3 eV are of predominant oxygen character, the states close to E_F are of predominant transition metal d character. The octahedral crystal field split Mn-t_{2g} states are occupied in the majority spin channel, Mn-e_g states being empty while both Mn-t_{2g} and Mn-e_g states are empty in the minority spin channel. Both Co-t_{2g} and Co-e_g states are occupied in the majority spin channel while partially filled Co-t_{2g} states cross E_F in the minority spin channel, minority Co-e_g states being empty. This result is in agreement with nominal valences of Co^{2+} and Mn^{4+} as reported in Refs. [4, 6, 12]. In accordance with the half metallic nature of the solution, the total magnetic moment turned out to be of integer value of 6.0 μ_B/f.u. with 0.01 μ_B at La site, 2.42 μ_B at Co site, 2.74 μ_B at Mn site, 0.09 μ_B at O site, and rest residing in the interstitial.

Fig. 4.4 shows the d-energy level positions at Co and Mn sites, measured with respect to E_F in non-spin-polarized situation. The octahedral crystal field splits the five-fold degenerate d levels into broad grouping of low-lying t_{2g}'s and high-lying $e_g(e_g^\sigma)$'s. The presence of additional trigonal distortion in the CoO_6 and MnO_6 octahedra further splits the t_{2g} states into singly degenerate a_{1g} and doubly degenerate e_g^π's, with e_g^π's being higher in energy compared to a_{1g}. The half metallic solution obtained within the spin-polarized GGA calculation is therefore obvious. The states in the majority spin channel are either fully empty or occupied. In the minority spin channel out of $2e^-$'s at the Co site, one occupies lowest lying a_{1g} state and

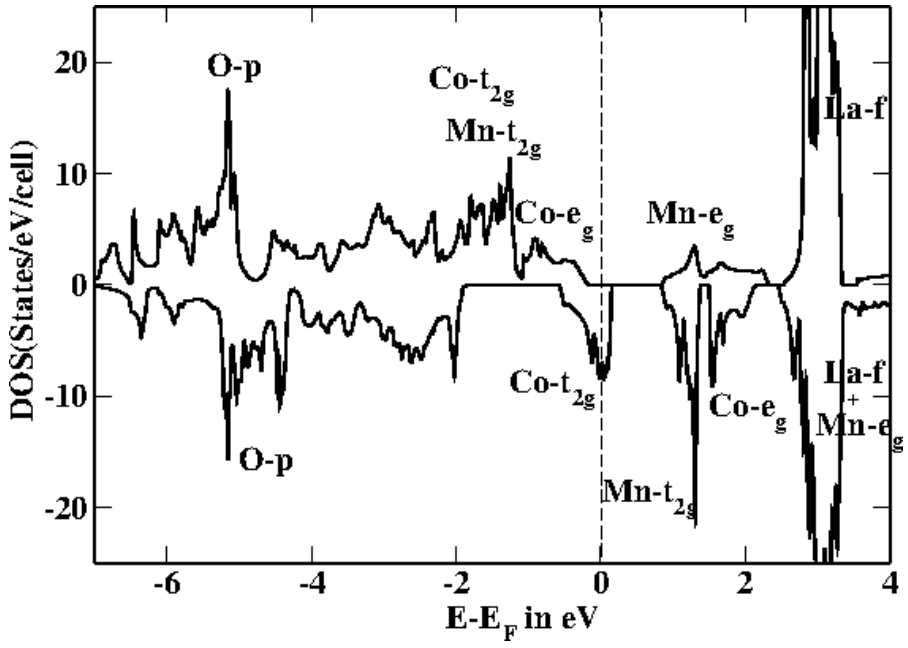

Figure 4.3 GGA density of states with dominant contribution of various orbital degrees of freedom are marked into the figure.

the remaining e^- can occupy either of the any doubly degenerate e_g^π states giving rise to a partially filled situation. While the broad $t_{2g} - e_g$ splittings turn out to be about 2 eV, the $t_{2g} - e_g^\pi$ splittings are much smaller, $\approx 0.04 - 0.05$ eV.

Application of missing correlation effect in the form of GGA+U calculation though increases the splitting between occupied Co-e_g and unoccupied Mn-e_g states in the majority spin channel, and that between occupied Co-t_{2g} and empty Mn-t_{2g}, Co-e_g in the minority spin channel, it cannot lift the degeneracy between degenerate Co-e_g^π states in the minority spin channel, leaving them partially filled with one electron. The left most upper panel of Fig. 4.5 shows the band structure of LCMO calculated within GGA+U (Ref. [13]) for a typical choice of U = 4 eV and J_H = 1 eV applied at Co and Mn sites. Only the minority channel is shown, since the majority channel is already gaped with either completely occupied or empty states. The corresponding DOS for both the spin channels is shown in the left most lower panel.

In order to explore the effect of spin-orbit coupling which is operative in t_{2g} manifold, we

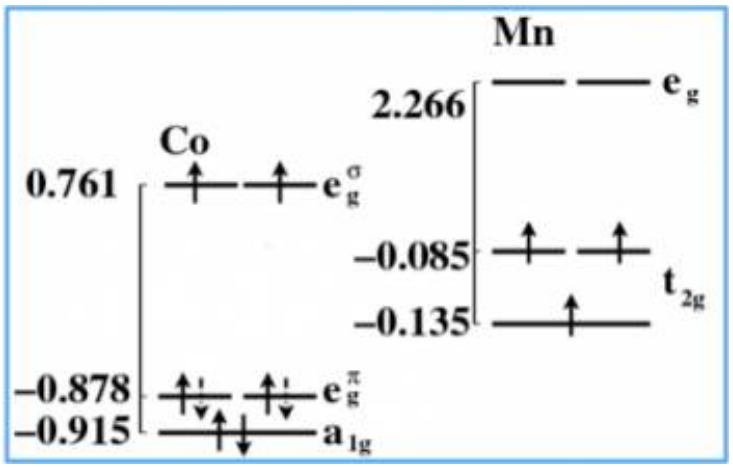

Figure 4.4 Energy level diagram for Co-d (left panel) and Mn-d (right panel) as obtained from NMTO-downfolding method. At Co-e_g^π level we see partially filled situation in the down spin channel.

carried out GGA+SO calculations for LCMO with the magnetization axis chosen along [001] direction. The orbital moment at Co and Mn site turned out to be 0.14 μ_B and -0.01 μ_B, respectively. Co^{2+} being more than half filled, the orbital moment is pointed along the direction of the spin moment, while Mn^{4+} being less than half filled, the orbital moment is pointed opposite to the direction of spin moment as listed in Table 4.2. The orbital moment at Mn site is tiny due to the t_{2g}^3 configuration with no orbital degrees of freedom left. The orbital moment at the Co site, on the other hand, is large due to the orbitally degenerate e_g^π states and introduction of SO coupling lifts the degeneracy of e_g^π as shown in upper middle panel of Fig. 4.5. This lifting of degeneracy gives rise to a pseudogap at E_F in the density of states in the minority spin channel, failing a bit short of opening the gap, as shown in the lower middle panel. The situation changes significantly upon application of GGA+U+SO, as is shown in the last panels of Fig. 4.5. For choices of U=4.0 eV and J_H = 1.0 eV, the orbital moment at Co site was renormalized to a value of 0.17 μ_B. The Mn orbital moment also showed a small renormalization to a value of -0.02 μ_B. This makes Co-$e_g^{\pi,1}$ state completely occupied and Co-$e_g^{\pi,2}$ state completely empty in the minority spin channel, opening up a gap of about 1.7

eV.[14] This clearly exhibits that LCMO is an insulator driven by Coulomb-assisted spin-orbit coupling, as has also been recently found for spinel compound [15] Fe_2CrS_4, and another double perovskite compound [16] Ba_2NaOsO_6.

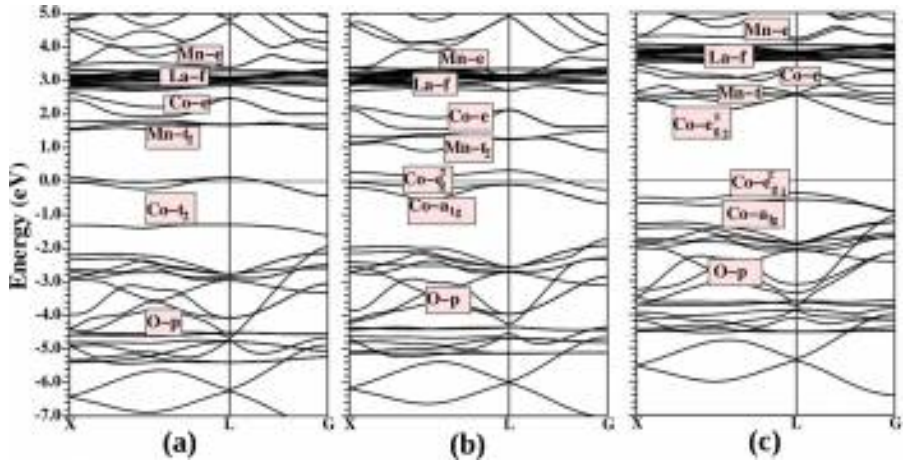

Figure 4.5 (a) The band structure calculated under GGA+U approximation in the minority spin channel. (b) The band structure is calculated under GGA+SO approximation, in the minority spin channel, with a pseudo gap at the Fermi level due to spin-orbit coupling. (c) The band structure calculated under GGA+U+SO approximation with a large gap at the Fermi level. The energy axis is labeled with respect to Fermi energy so that Fermi level has zero energy label on the energy axis.

Within the spin-polarized calculations, the ferromagnetic spin alignment between Co and Mn, was found to be energetically stabler compared to antiferromagnetic spin alignment by about 0.3 eV, in conformity with the observed ferromagnetism in this compound.[4] The antiparallel alignment leads to a total spin of zero, with perfect cancellation of Co and Mn spins. Low-energy Hamiltonian is defined starting from the full DFT band structure by keeping active only the Co-d and Mn-d states and integrating out all the rest, by employing the NMTO-downfolding procedure. The process leads to the renormalization of Co-d and Mn-d wave functions by integrating out the O and La orbital degrees of freedom thereby defining the superexchange paths connecting the Co and Mn ions. Employing the extended Kugel-Khomskii-

Table 4.2 The table is showing spin moments and orbital moments calculated under various approximations.

	Co		Mn	
	spin moment (μ_B)	orbital moment (μ_B)	spin moment (μ_B)	orbital moment (μ_B)
GGA	2.42	···	2.74	···
GGA+U	2.57	···	2.83	···
GGA+SO	2.41	0.14	2.76	-0.012
GGA+U+SO	2.56	0.17	2.88	-0.018

like model, as done for [8] La_2NiMnO_6, the nearest neighbor magnetic exchange interaction between Co and Mn turned out to be of ferromagnetic nature and a value of 4 meV, for a choice of U = 4.0 eV and J_H = 1.0 eV.

4.5 Phonon calculation

LCMO compound has been reported to exhibit magnetodielectric effect.[9] In order to investigate this issue, we studied the response of optimized rhombohedral structure to changes in magnetic ordering, e.g., changes in phonon frequencies with changes in magnetic ordering. For this purpose, we calculated the Γ-point phonons for the rhombohedral structure for the ferromagnetic alignment of Co and Mn spins vis-a-vis the antiparallel alignment of Co and Mn spins. Since the considered rhombohedral structure is the high temperature structure while the ground state structure is of monoclinic symmetry,[12] our T = 0 K calculations carried out on rhombohedral symmetry show presence of unstable modes. We find that frequencies of the

lowest energy infrared (IR)-active phonons soften from 79.1, 137.3, and 201 cm^{-1} in the FM phase to 31.2, 96.9, and 166.3 cm^{-1}, respectively (indicated by arrows in Fig. 4.6), exhibiting a strong coupling with spin. The examination of atomic displacements corresponding to the lowest frequency mode, as shown in the inset of Fig. 4.6, shows that the angle between the Mn−O (at the center of the oxygen-octahedra) and O-Co (rightmost corner of the cell) is affected by this phonon, reflecting the signature of exchange-striction driven spin-phonon coupling. Our observed softening of IR-active phonon modes may be compared with the case of La_2NiMnO_6, where softest phonon was found [8] to soften from 91.3 cm^{-1} in FM phase to 65.5 cm^{-1} for the antiparallel alignment. One would therefore expect a similar nature of magnetodielectric effect in LCMO as observed in case of La_2NiMnO_6. We note that neither of these two double perovskites are ferroelectrics. If they can be made ferroelectric by doping [17] or straining then one would expect a new class of multiferroic material with large magnetoelectric effect.

4.6 Conclusion

In conclusion, using first-principles DFT calculations, we have explored the electronic structure of FM double perovskite compound, LCMO, which to the best of our knowledge has not been taken up earlier. Our study shows that unlike the sister compound, La_2NiMnO_6, the insulating behavior in this compound, is driven by spin-orbit coupling within the Co-e_g^{π} states of the octahedral and trigonal crystal field split Co-d manifold which gets assisted by the presence of Coulomb correlation. We also explored the existence of possible spin-phonon coupling in this material. Our study showed the presence of soft IR-active phonon modes that respond strongly in terms of further softening upon changing the magnetic ordering. This

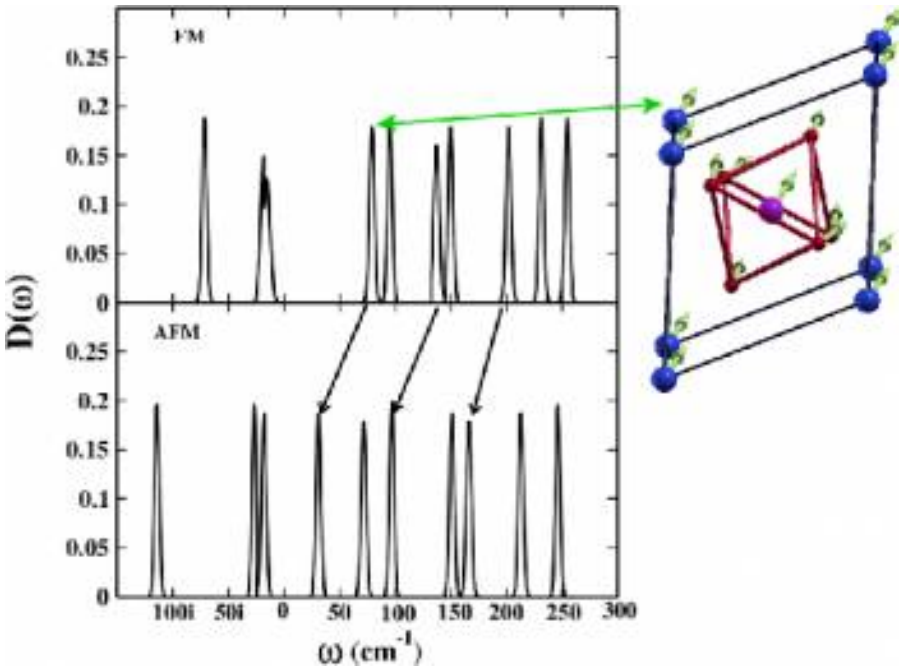

Figure 4.6 Phonon density of states as a function of frequencies calculated at Γ point in the Brillouin zone. The upper panel of the figure shows the IR-active phonons for parallel alignment of Co and Mn spins. The lower panel of the figure shows phonon density of states corresponding to anti-parallel alignment of Co and Mn spins. On the right panel of the figure the atomic displacements corresponding to the lowest energy IR-active phonon mode is shown.

would lead to large magnetodielectric effect, as observed experimentally.

Bibliography

[1] V. I. Belotelov, E. A. Bezus, L. L. Doskolovich, A. N. Kalish, and A. K. Zvezdin, Journal of Physics: Conference Series **200,** 092003 (2010).

[2] B. T. Matthias, R. M. Bozorth, and J. H. Van Vleck, Phys. Rev. Lett. **7,** 160–161 (1961).

[3] P. K. Baltzer, H. W. Lehmann, and M. Robbins, Phys. Rev. Lett. **15,** 493–495 (1965).

[4] V. L. J. Joly, Y. B. Khollam, P. A. Joy, C. S. Gopinath, and S. K. Date, Journal of Physics: Condensed Matter **13,** 11001 (2001).

[5] V. I. Belotelov, E. A. Bezus, L. L. Doskolovich, A. N. Kalish, and A. K. Zvezdin, Journal of Physics: Conference Series **200,** 092003 (2010).

[6] T. Kyomen, R. Yamazaki, and I. M., Chem. Mater. **15,** 4798 (2003).

[7] H. Z. Guo, A. Gupta, T. G. Calvarese, and M. A. Subramanian, Applied Physics Letters **89,** – (2006).

[8] H. Das, U. V. Waghmare, T. Saha-Dasgupta, and D. D. Sarma, Phys. Rev. Lett. **100,** 186402 (2008).

[9] K. D. Truong, J. Laverdiere, M. P. Singh, S. Jandl, and P. Fournier, Phys. Rev. B **76,** 132413 (2007).

[10] S. Yanez-Vilar, A. Castro-Couceiro, B. Rivas-Murias, A. Fondado, J. Mira, J. Rivas, and M. A. Senaris-Rodriguez, Zeitschrift fÃijr anorganische und allgemeine Chemie **631,** 2265–2272 (2005).

[11] Y. Q. Lin and X. M. Chen, Journal of the American Ceramic Society **94,** 782–787 (2011).

[12] C. L. Bull, D. Gleeson, and K. S. Knight, Journal of Physics: Condensed Matter **15,** 4927 (2003).

[13] V. I. Anisimov, I. V. Solovyev, M. A. Korotin, M. T. Czyżyk, and G. A. Sawatzky, Phys. Rev. B **48,** 16929–16934 (1993).

[14] The gap value is found to increase more or less linearly upon increasing U value. To the best of our knowledge, no experimental estimate of gap value exists in literature.While the U value has been chosen to be typical U values for Co and Mn, it may be adjusted following the knowledge of the experimental gap value. .

[15] S. Sarkar, M. De Raychaudhury, I. Dasgupta, and T. Saha-Dasgupta, Phys. Rev. B **80,** 201101 (2009).

[16] H. J. Xiang and M.-H. Whangbo, Phys. Rev. B **75,** 052407 (2007).

[17] D. J. Singh and C. H. Park, Phys. Rev. Lett. **100,** 087601 (2008).

Chapter 5

Study of A-cation Effect in Transition Metal Oxides: Sr_2CrSbO_6 and Ca_2CrSbO_6

5.1 Background

As discussed already, 3d transition metal oxides (TMO's) are fascinating group of materials with intriguing electrical and magnetic properties. Spins associated with the magnetic transition metal ions interact with the neighboring magnetic ion spins either directly or indirectly. This gives rise to the various kinds of magnetic interactions that generate magnetism in TMO's. The alkaline earth or rare-earth cation in the structure (A-cation in perovskites ABO_3 or double perovskites $A_2BB'O_6$) are believed to serve as charge reservoir with any direct influence on magnetism. In this chapter we study two double perovskite compounds Sr_2CrSbO_6 and Ca_2CrSbO_6 that present quite different perspective compared to above.

This chapter is based on *Phys. Rev. B 86, 024440 (2012)*

5.2 Introduction

Recently, the role of rare-earth or alkaline-earth ions, the A-cation in the TMO's in perovskites or perovskite derived double perovskite structure, has been realized and appreciated as beyond the role of spectator [1]. To mention a few examples, $SrRuO_3$ is the only ferromagnetic 4d transition metal oxide, while replacing Sr by Ca, $CaRuO_3$ does not show long-range ferromagnetic order [2]. The observation of varied magnetic ground states upon changing the A-site cation, clearly challenges the idea of nonmagnetic A-cation playing no role in the magnetism of B-cations. Double perovskite compounds Sr_2CrSbO_6 and Ca_2CrSbO_6 provide another example of A-cation playing role in the magnetic interaction. Sr_2CrSbO_6 compound is reported [3] to order with an antiferromagnetic alignment of Cr spins at a Nee'l temperature of 12 K, while Ca_2CrSbO_6 compound is reported [4] to exhibit ferromagnetic long-rage ordering of Cr spins below T_c of 16 K. The ordering temperatures of both Sr_2CrSbO_6 and Ca_2CrSbO_6 are rather low, as due to large Cr-Cr distance separated by nonmagnetic ions Cr-Cr interactions are expected to be low. What is interesting, though, is the switching from antiferromagnetism to ferromagnetism upon substitution of Sr by Ca. It is interesting to find out the microscopic origin of this difference in magnetic behavior. Given the fact that the ordering temperatures are rather low, it is also a challenge for the ab initio theory to capture the effects accurately. Using first-principles density functional theory based calculations, we show that it is not only capable of capturing the ferromagnetic (FM) and antiferromagnetic (AFM) ordering tendencies in Sr_2CrSbO_6 and Ca_2CrSbO_6, respectively, it also provides a microscopic understanding of the contrasting behavior in the two compounds.

5.3 Crystal Structure

Both Sr_2CrSbO_6 (SCSO) and Ca_2CrSbO_6 (CCSO) compounds belonging to the class of double perovskite compounds form in monoclinic structure with $P2_1/n$ space group[3, 5]. The stabilization of monoclinic space group over the orthorhombic one, signals the ordering of CrO_6 and SbO_6 octahedra in a rocksalt fashion [6], as shown in Fig. 5.1. The degree of Cr-Sb ordering has been reported to 97% for the Sr compound and 92% for the Ca compound [3]. The comparison of crystal structure data between SCSO and CCSO shows CCSO structure to be more distorted compared to that of SCSO which is driven by smaller ionic radius of Ca^{2+} compared to that of Sr^{2+} (see Table 5.1). The deviation of average Cr-O-Sb angle from 180° is 16.7° more for Ca compared to that of Sr compound. The average Cr-O bond length shows a small expansion of about 0.5% in Ca compared to that in Sr compound. CrO_6 octahedra is distorted for both SCSO and CCSO in the sense that all three pairs of Cr-O bond lengths are different and all O-Cr-O angles deviate from 90°.

5.4 Results

5.4.1 Basic Electronic Structure

Figure 5.2 shows the non-spin-polarized density of states (DOS) of SCSO and CCSO calculated within GGA in LAPW basis. The states crossing the Fermi level, E_F is of dominant Cr character, as shown in top panel of Fig. 5.2. The octahedral crystal field surrounding Cr ions splits the Cr-d states into two board groups of Cr-t_{2g} and Cr-$_{eg}$, which show small splitting within themselves arising due to distortion in CrO_6 octahedra. This distortion also leads to finite mixing between t_{2g} and e_g degrees of freedom as seen in DOS plot in Fig. 5.2. The

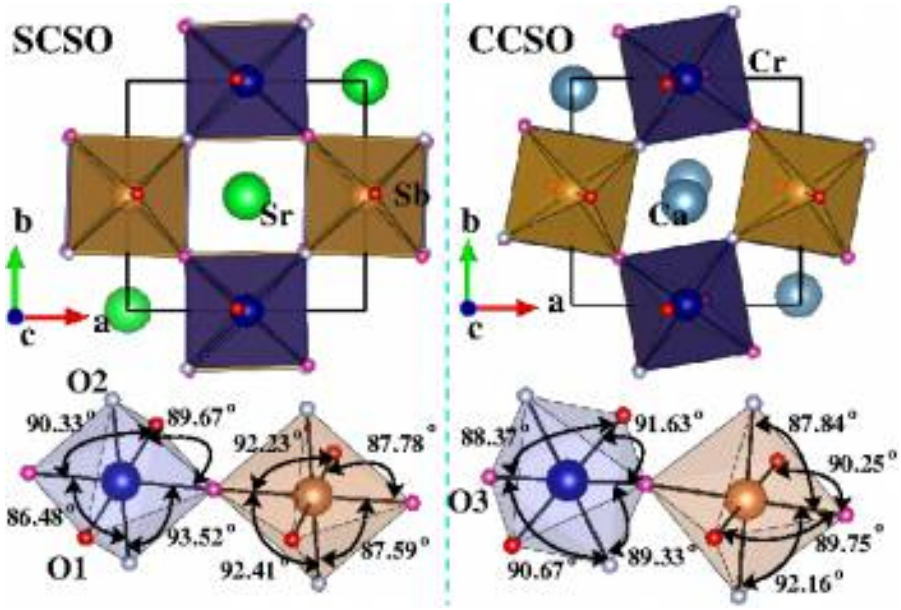

Figure 5.1 Top panels: Crystal structure of Sr_2CrSbO_6 (SCSO) and Ca_2CrSbO_6 (CCSO) projected onto a-b plane. The CrO_6 and SbO_6 octahedra are colored as violet (dark gray) and yellow (light gray), respectively. The Sr/Ca atoms sit in the hollow formed by corner shared CrO_6 and SbO_6 octahedra. The O atoms occupying the corners of the octahedra are shown as small balls, belonging to three different classes, O1, O2, and O3. Bottom panels: The O-Cr-O and O-Sb-O bond angles in two compounds.

relatively narrow Cr-t_{2g} states occupy the range of ≈ 0.5 eV below E_F to ≈ 0.2 eV above E_F , while Cr-e_g states remain empty, occupying an energy window of about $2-2.5$ eV, positioned around 2 eV above E_F. The Cr-e_g band width is relatively wider for SCSO compared to that of CCSO, which almost closes the gap between Cr-t_{2g} and Cr-e_g manifold. The O-p states occupy mostly the energy range below -3 eV or so, though they show finite mixing with Cr-d states, as shown in the middle panel of Fig. 5.2. The last panel in Fig. 5.2 shows the DOS projected onto Sr/Ca states as well as onto Sb states. Both of these (A as well as B') degrees of freedom show finite mixing with Cr-d states, the contribution of Sr states in Cr-d manifold being somewhat larger than that of Ca states.

Table 5.1 Structural comparison between SCSO and CCSO compounds.

	$P2_1/n$	**SCSO**	**CCSO**
		a=5.576 b=5.554 c=7.847	a=5.408 b=5.494 c=7.690
		β=89.98	β=90.101
	wyckoff	x y z	x y z
Sr/Ca	4e	1.000 0.004 0.252	0.990 0.043 0.251
Cr	2d	0.5 0.0 0.0	0.5 0.0 0.0
Sb	2b	0.5 0.0 0.5	0.5 0.0 0.5
O1	4e	0.040 0.510 0.248	0.082 0.477 0.250
O2	4e	0.751 0.250 0.014	0.703 0.297 0.041
O3	4e	0.239 0.236 0.976	0.208 0.211 0.954
∠Sb-O1-Cr		166.63°	153.00°
∠Sb-O2-Cr		173.42°	151.87°
∠Sb-O3-Cr		167.63°	152.59°
<Cr-O>		1.978	1.988
<Sb-O>		1.972	1.977
< ∠Cr-O-Sb>		169.23 °	152.49 °

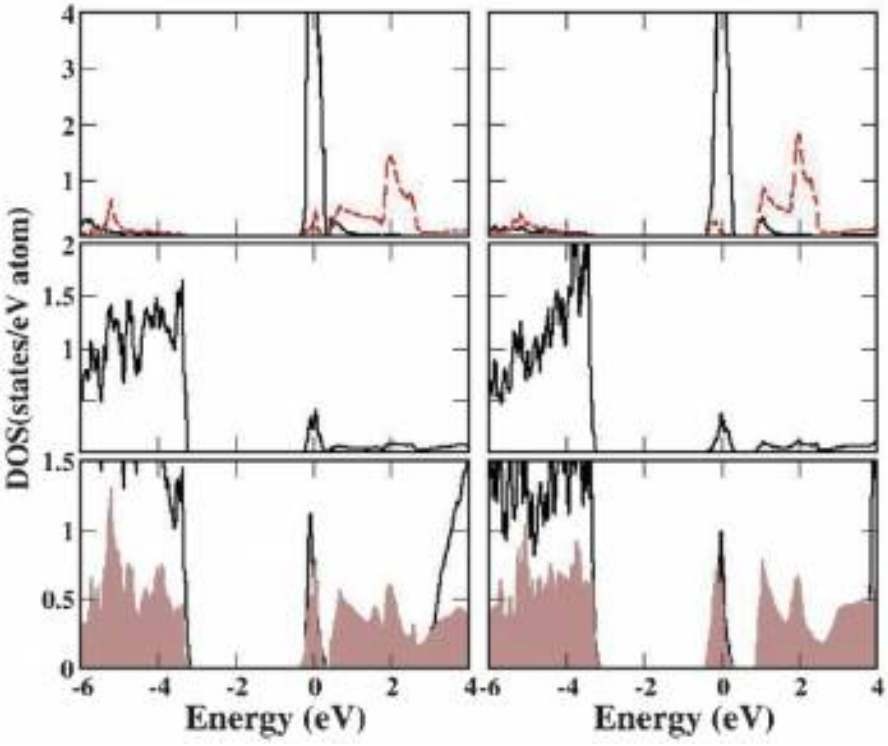

Figure 5.2 Top panels: GGA DOS for SCSO (left) and CCSO (right) projected onto Cr-d states. The t_{2g} and e_g contributions are shown in solid and dashed lines, respectively. Middle panels: O-p DOS for SCSO (left) and CCSO (right). Bottom panels: GGA DOS for SCSO (left) and CCSO (right) projected onto Sr/Ca states (solid lines) and Sb states (shaded area). The zero of the energy is set at GGA Fermi energy, E_F.

5.4.2 Superexchange Interaction

In order to understand the superexchange-driven magnetism in these two compounds, in the next step we define a low energy Hamiltonian starting from the full DFT band structure by keeping active only the Cr-d states and integrating out all the rest, by employing the NMTO-downfolding procedure [7]. The process leads to the renormalization of Cr-d wave functions by integrating out the O-p, Sr/Ca and Sb degrees of freedom thereby defining the superexchange paths connecting the two Cr ions. Figure 5.3 shows the low-energy band structure in comparison to the full band structure, calculated in NMTO basis, for SCSO and CCSO. The nearly perfect agreement between the two, validates the goodness of the procedure. The wave

functions defining the basis for the low-energy, downfolded band-structure are the effective Cr-d wave functions, which serve as the Wannier-like functions for the underlying low-energy band structure. The Fourier transformation of the low-energy Cr-d Hamiltonian, H(k) $\rightarrow$ H(R), provides the effective hopping integrals connecting the neighboring Cr-d levels and the crystal field splitting between various d levels at the Cr site. The Cr ion in its nominal valence of 3+, gives rise to half-filled t_{2g} levels and empty e_g levels, as shown in Fig. 5.4, for SCSO.

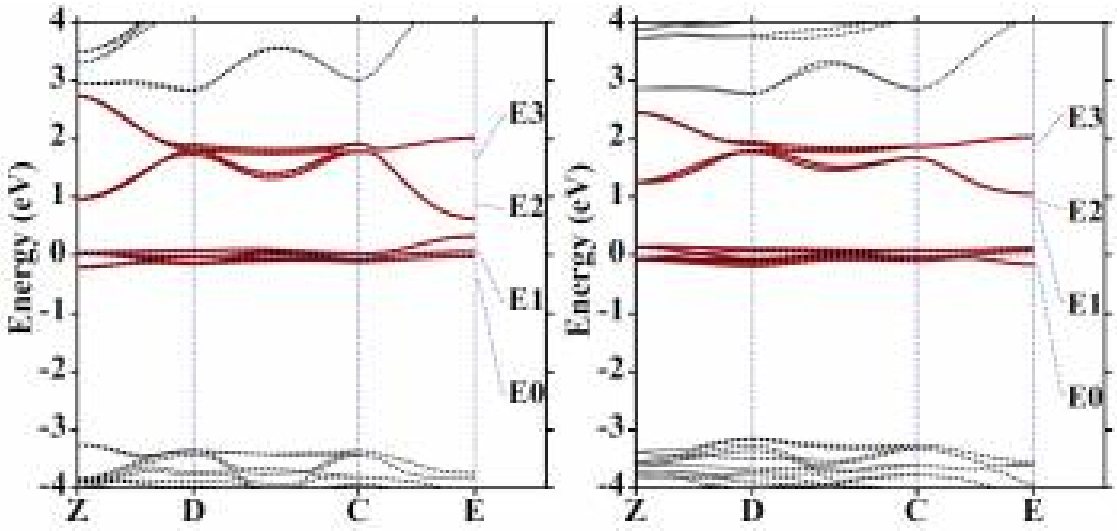

Figure 5.3 The NMTO-downfolded Cr-d only band structure (shown in red, solid lines) in comparison to full GGA band structure (shown in black, dashed lines) for SCSO (left panel) and CCSO (right panel). E0-E3 denote the energy points about which energy expansions have been carried out in NMTO calculation.

Two different hopping processes are involved in the superexchange. The first process involves hopping from half-filled t_{2g} levels at one Cr site to half-filled t_{2g} levels at neighboring Cr site. This superexchange process is of AFM nature [8, 9, 10] and of magnitude $\sum_{ij} \frac{2t_{ij}^2}{(U+\Delta_{ij})}$, where t_{ij} is the hopping interaction connecting i^{th} t_{2g} level at Cr site 1 to j^{th} t_{2g} level at Cr site 2, Δ_{ij} is the difference in energy level position of i^{th} and j^{th} level and U is the Hubbard U, the energy cost in putting two electrons at the same site. The second process involves hopping from half-

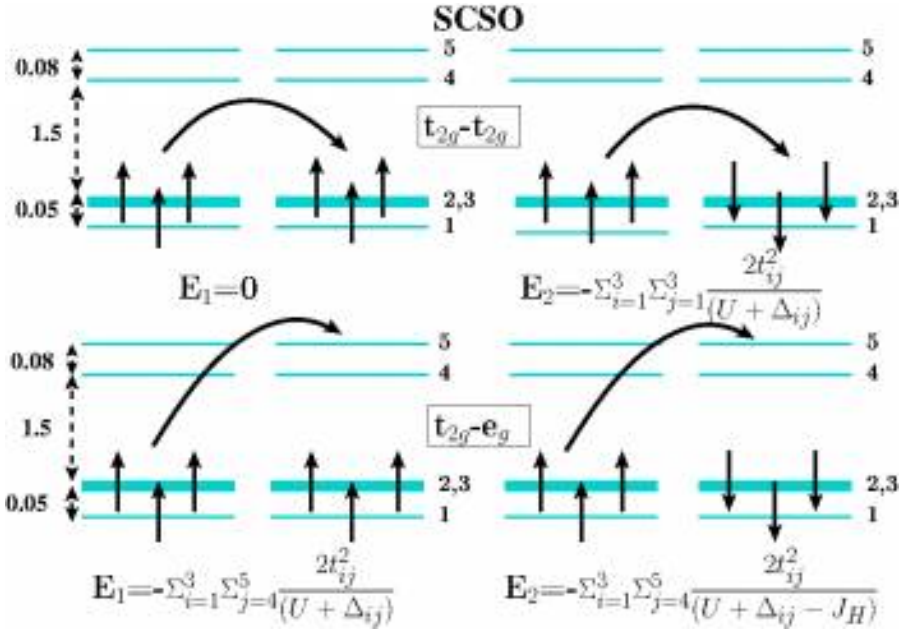

Figure 5.4 The superexchange processes and the corresponding energy costs for virtual hopping between half-filled Cr-t_{2g} states and half-filled Cr-t_{2g} states (top panels), and that between half-filled Cr-t_{2g} states and empty e_g states (bottom panels). The values of crystal field splittings are shown for specific case of SCSO.

filled t_{2g} states at Cr site 1 to empty states at Cr site 2. This superexchange process is of FM nature, favored by Hund's coupling J_H and given by [9, 10], $-\sum_{ij}\frac{2t_{ij}^2 J_H}{(U+\Delta_{ij})(U+\Delta_{ij}-J_H)}$, where t_{ij} is the hopping connecting i^{th} t_{2g} state and the j^{th} e_g state, Δ_{ij} being the corresponding energy level splitting. The net magnetic exchange is given by the sum of the two processes and the balance between the AFM and FM component depends on the precise values of t_{ij} and Δ_{ij} . For the determination of t_{ij} and Δ_{ij} we use the real-space description of the low-energy, Cr-t_{2g}-only Hamiltonian as given by NMTO-downfolding calculation. Figure 5.5 summarizes the results for the first-nearest-neighbor (1NN) Cr-Cr interaction, $J^{(1)}$, for a variation of U values at Cr site. The Hund's coupling J_H is assumed to be fixed at 0.9 eV. We find that in general the AFM component of magnetic exchange, $J^{(1)}_{AFM}$ is larger for the Sr compound to that for the Ca compound while the reverse is true for the FM component of magnetic exchange

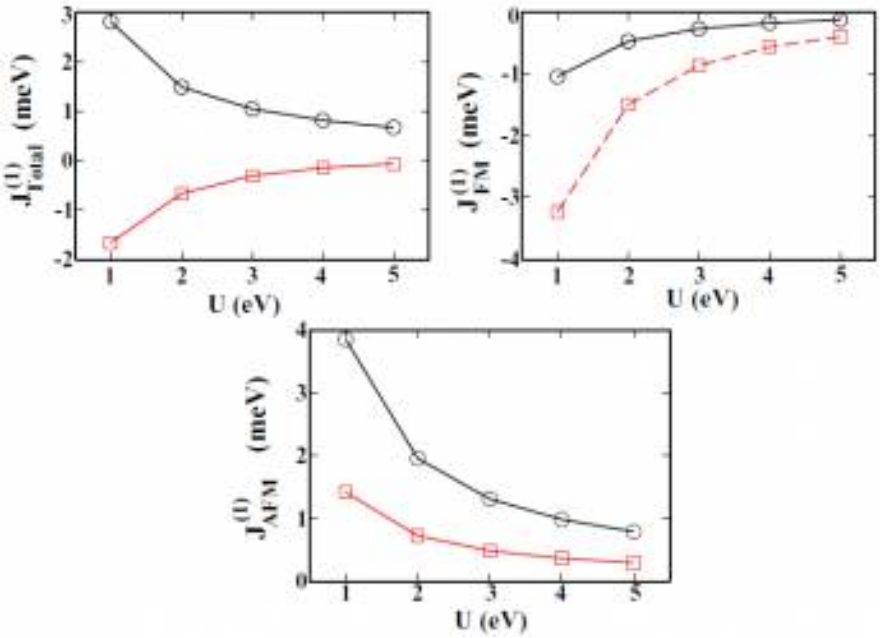

Figure 5.5 The total (left, top panel), ferromagnetic (right, top panel) and antiferromagnetic (bottom panel) components of the first-nearest-neighbor Cr-Cr magnetic exchange, plotted as a function of U for SCSO (circles) and CCSO (squares).

$J^{(1)}_{FM}$. The resulting net magnetic component of magnetic exchange: $J^{(1)}_{Total} = J^{(1)}_{AFM} + J^{(1)}_{FM}$, is of positive sign for SCSO and therefore of AFM nature while it is of negative sign for CCSO and therefore of FM nature. As expected with increase of U value, the magnitude of $J^{(1)}$ decreases. We repeated this exercise for the second nearest neighbors Cr-Cr interaction, $J^{(2)}$, as well. Figure 5.6 shows the comparison of $J^{(1)}$ to that of $J^{(2)}$ for SCSO and CCSO. The 1NN and 2NN superexchange paths are shown in the inset. While in literature, attention has been focused [3] on 2NN interaction given by the superexchange path Cr-O-Sb-O-Cr, we find it is the 1NN interaction, which involves the hopping through Sr/Ca site, dominates and is the relevant one to be considered. We further note the 2NN interactions which are significantly smaller in magnitude compared to 1NN interactions, are of same sign for both SCSO and CCSO. Therefore, the switching from net AFM to FM behavior of SCSO to CCSO is governed by the 1NN superexchange path through Sr or Ca ion.

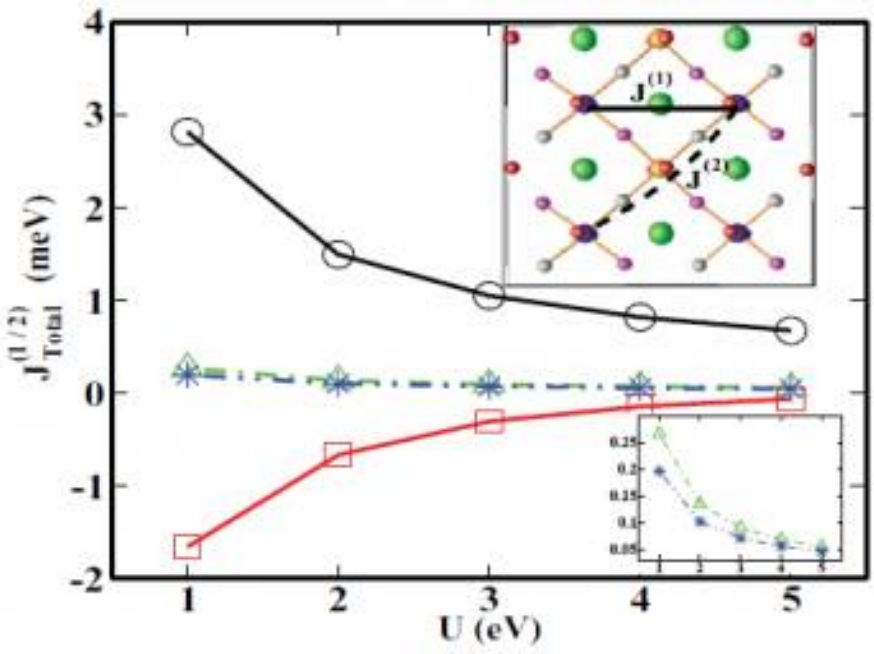

Figure 5.6 The second-nearest-neighbor Cr-Cr magnetic exchange in comparison to first-nearest-neighbor Cr-Cr magnetic exchange plotted as a function of U. The first- and second nearest-neighbor interactions are shown as circles (squares) and triangles (stars) for SCSO (CCSO), respectively. The top inset show the superexchange paths for the first-nearest-neighbor interaction, $J^{(1)}$ and second-nearest-neighbor interaction, $J^{(2)}$, considering the case of SCSO. The bottom inset shows the zoomed plot showing the second-nearest-neighbor interaction, $J^{(2)}$.

5.4.3 Wannier Function

To understand the dominance of 1NN superexchange path over the 2NN, we show in the top panel of Fig. 5.7 the plot of effective Cr t_{2g} (d_{xy}) Wannier function placed at two Cr sites of SCSO, one at 1NN positions and another at 2NN positions. While the central part of the functions are shaped according to t_{2g} symmetry, the tails are shaped according to integrated out O-p symmetry. We find that O-p-like tails are deformed in the sense O-p_x/p_y tails are bend towards Sr atom, which highlights the importance of hybridization effect from Sr. This in

turn facilitates the 1NN Cr-Cr interaction significantly, forming an overlapping path between Wannier functions at two Cr sites. The 2NN Cr-Cr interaction on the other hand, does not benefit from this bending of tails; the two Wannier functions remain more or less decoupled, though tiny overlap is noticed at 2NN O sites. Having understood that the 1NN interaction being stronger than 2NN, we show in the bottom panel of Fig. 5.7 a plot of Cr-t_{2g} Wannier functions at 1NN and 2NN positions of CCSO. Comparing with the case of SCSO, we notice two differences. First, the bending of O p_x/p_y tails is somewhat less pronounced for CCSO compared to that of SCSO. Second, due to larger distortion in the structure in case of CCSO the tails are misaligned, weakening the AFM superexchange path. The increased distortion in the structure in case of CCSO compared SCSO, on the other hand, causes greater t_{2g}-e_g mixing and therefore, relatively stronger t_{2g} to e_g hopping than that of SCSO, making $J^{(1)}$ FM stronger for CCSO. The combined effect of weakening of the AFM superexchange and strengthening of the FM superexchange, leads to a net FM Cr-Cr interaction for the Ca compound, as opposed to an AFM Cr-Cr interaction in the Sr compound. We note that such effects are rather subtle and the result depends on the reliable estimate of t and Δ, which the NMTO-downfolding method is clearly capable of providing. Finally, in order to appreciate the effect of the structural distortion on the sign and values of $J^{(1)}$, we repeated the calculation of $J^{(1)}$ for CCSO assuming the same crystal structure as that of SCSO. The resulting $J^{(1)}$ is found to be of AFM type, slightly smaller in magnitude compared to that of SCSO. This happens as the AFM component is increased compared to that of real CCSO, due to the prevention of misalignment of tails, and the FM component is reduced compared to that of real CCSO, due to reduced t_{2g}-e_g mixing. This in turn, emphasizes the role of lattice distortion.

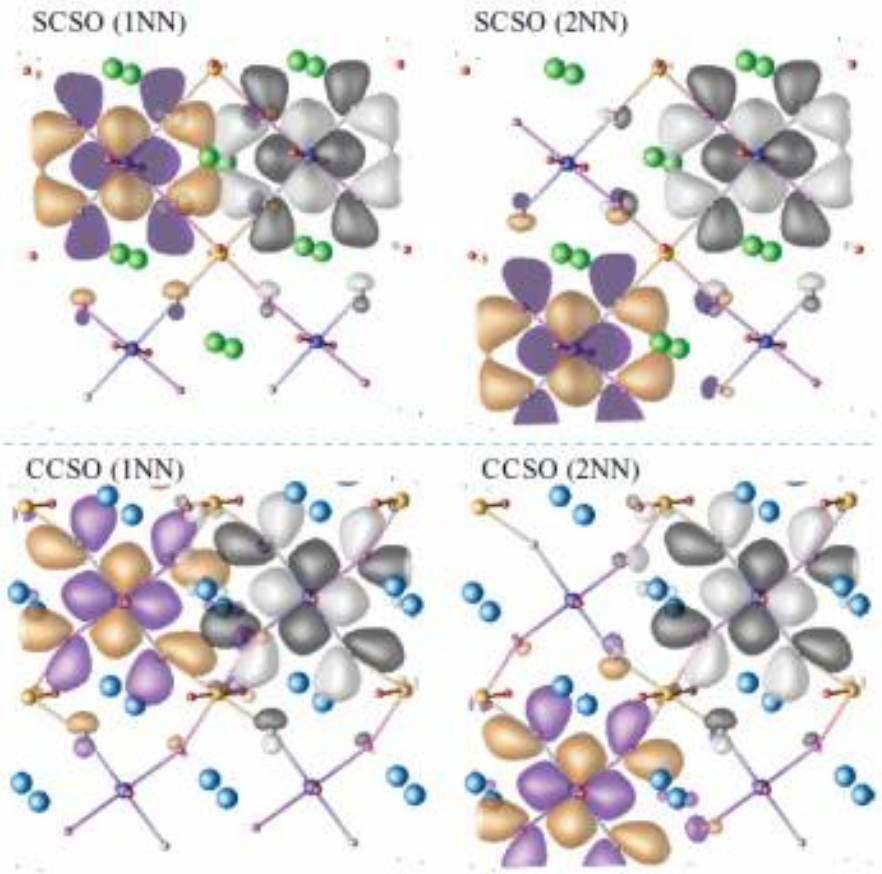

Figure 5.7 Effective orbitals corresponding to the downfolded Cr d_{xy} NMTOs, placed at two Cr sites situated at first nearest- neighbor (left panels) and second-nearest-neighbor (right panels) positions for SCSO (top panels) and CCSO (bottom panels). Lobes of the orbitals placed at different Cr sites are colored differently.

5.5 Antiferromagnetic Ordering in Sr_2CrSbO_6

The FCC lattice of Cr spins in SCSO, consisting of edge-shared Cr_4 tetrahedra with AFM 1NN coupling is known to be geometrically frustrated Fig. 5.8, as in the case of Ba_2LnSbO_6 or Sr_2LnSbO_6 (Ln = Dy, Ho, Gd), in which case no magnetic ordering is observed down to a temperature scale of 2 K or so [11]. While frustrated triangular, kagome, pyrochlore, and square-lattice systems have been extensively studied,[12] there have been relatively few studies of frustrated FCC lattice. The few studies carried out on frustrated FCC lattice in

the context of double perovskite compounds [13, 14, 15] indicate that weak 2NN coupling or small anisotropy can, however, give rise to stabilization of the AFM order. The experimentally observed AFM structure of SCSO [3] is an A-type AFM structure (cf. Fig. 5.9) with ferromagnetic layers of Cr moments in the ab plane, coupled antiferromagnetically along the c-axis. This leads to a high degree of frustration with each Cr spin surrounded by four in-plane Cr spins ferromagnetically coupled and eight out-of-plane Cr spins antiferromagnetically coupled. The spin wave theory of frustrated AFM on FCC lattice predicts [13, 15] that FM 2NN coupling stabilizes the AFM-A structure, while AFM 2NN coupling leads to stabilization of the AFM-G structure with all neighboring Cr spins being antiferromagnetically coupled. Since the observed AFM structure for SCSO is of AFM-A type, the tiny but AFM nature of 2NN coupling cannot explain this. The alternative explanation could be the stabilization through anisotropy. In order to probe this, we carried out GGA+U+SOC calculations in LAPW basis,

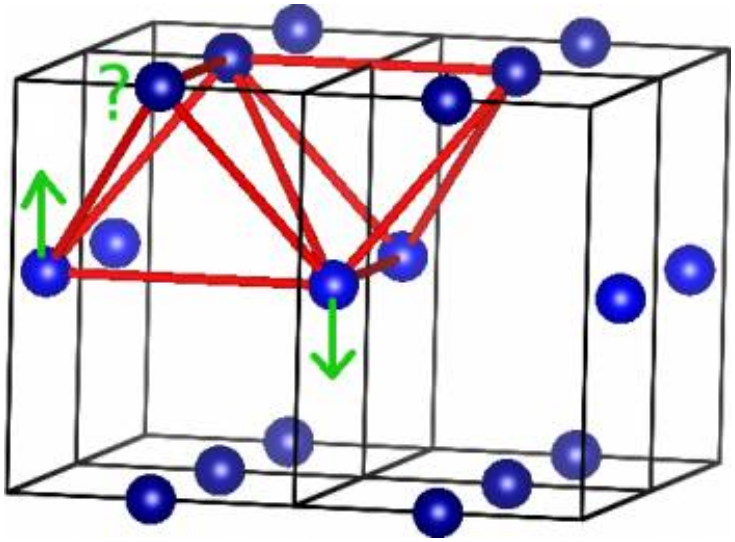

Figure 5.8 Frustrated Cr sublattice in SCSO. Edge-shared Cr_4 tetrahedra gives rise to magnetic frustration due to competitive AFM interaction. Blue balls represent Cr atoms.

considering the spin quantization axis pointed along the [001] direction as well as the [110] direction with choice of U = 5 eV and J_H = 0.9 eV. The [110] direction is found to be favored

energetically compared to that of the [001] direction by about 1.8 meV/f.u. The preference of the [110] magnetization direction is in conformity with the experimental observations [3]. The orbital moment at Cr site is expected to be vanishingly small due to t_{2g}^3 configuration, but finite covalency with oxygen [16] gives rise to an orbital moment of -0.05 μ_B. For the magnetocrystalline anisotropy of positive sign with E_{110} being favorable compared to E_{001} leads to stabilization of AFM-A structure, as discussed in Ref. [14].

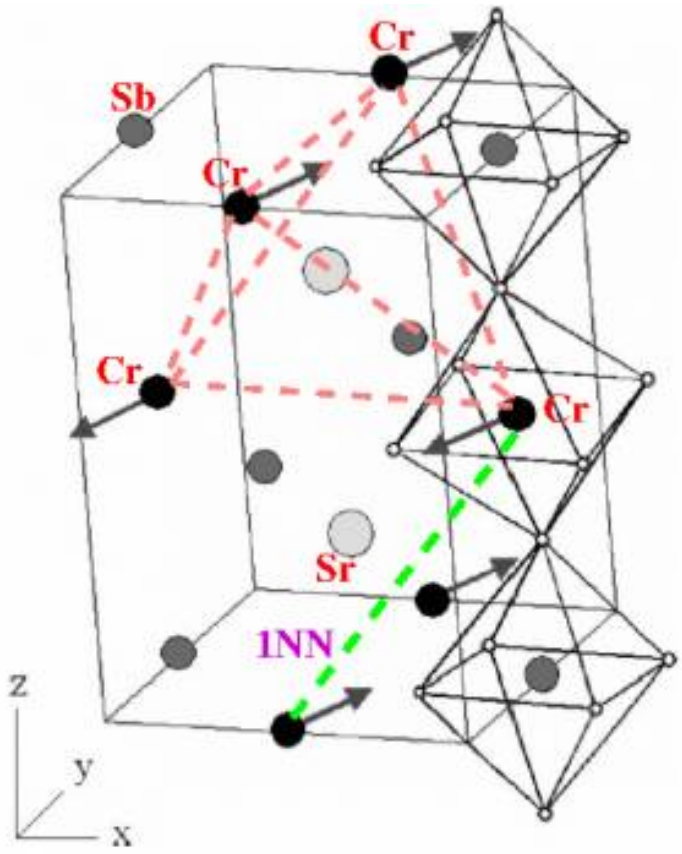

Figure 5.9 A-type AFM configuration with canted spin of Cr ions. The Cr spins are parallel in ab plane and antiparallel along c-axis. Red dotted lines connecting Cr ions represent the Cr_4 tetrahedra. Canted Cr spins within the Cr_4 tetrahedra removes magnetic frustration in the Cr sublattice. (reproduced from [3])

5.6 Total Energy Calculations

The above analysis though provides immense microscopic insight is based on the second order perturbative treatment. Therefore, in order to check the accuracy of the above analysis, we carried out total energy calculations within the GGA+U+SOC scheme in LAPW basis for SCSO and CCSO compounds, considering two different spin alignments, the FM and A-type AFM as observed for SCSO [3]. From our experience on the U dependence of J values as given by the superexchange formula, described above, we choose U = 5 eV and J_H = 0.9 eV. With this choice, E(AFM) - E(FM) turned out to be -2.72 meV for SCSO and +1.63 meV for CCSO. Mapping the total energy differences to spin model, the J values turn to be -0.08 meV for SCSO and 0.05 meV for CCSO. This leads to mean-field estimates of T_N = 14 K for SCSO and T_C = 8 K for CCSO, in rather good agreement with the experimental estimates.

5.7 Conclusion

To conclude, we have carried out first-principles calculations in order to gain microscopic understanding of the switching from AFM to FM long-range order in double perovskite compound SCSO, in replacing Sr by Ca. Our study reveals that the first-neighbor magnetic interaction mediated by the superexchange path involving Sr/Ca dominates over the the second-neighbor magnetic interaction. While in the literature, importance has been placed on second-neighbor magnetic interaction,[4] our study shows that it is the first nearest-neighbor interaction that dictates the physical behavior. Plugging in the NMTO-downfolding-derived estimates of effective Cr-Cr hopping and the crystal field splitting in the superexchange formula could successfully reproduce the ferromagnetic and antiferromagnetic nature of magnetic interactions in Ca_2CrSbO_6 and Sr_2CrSbO_6 compounds respectively. The differences in the hybridization effect between Sr and Cr to that of Ca and Cr, together with differences in the

distortion of the crystal structure driven by size difference of Sr^{2+} and Ca^{2+} ions, drive this interesting switching of magnetic properties at Cr sublattice. Finally, the magnetocrystalline anisotropy at Cr site drives the A-type AFM ordering in case of SCSO. Similar behavior has been reported for A_2MnRuO_6 (A=Sr,Ca). While Sr_2MnRuO_6 is observed to be an AFM insulator, Ca_2MnRuO_6 is found to be a metallic ferromagnet [17]. It will be worthwhile to explore these compounds in a further study.

Bibliography

[1] E. Pavarini, A. Yamasaki, J. Nuss, and O. K. Andersen, New Journal of Physics **7,** 188 (2005).

[2] I. I. Mazin and D. J. Singh, Phys. Rev. B **56,** 2556–2571 (1997).

[3] M. Retuerto, M. Garcia-Hernandez, M. J. Martinez-Lope, M. T. Fernandez-Diaz, J. P. Attfield, and J. A. Alonso, J. Mater. Chem. **17,** 3555–3561 (2007).

[4] M. Retuerto, J. Alonso, M. Garcia-Hernandez, and M. Martinez-Lope, Solid State Communications **139,** 19 – 22 (2006).

[5] A. Faik, J. Igartua, M. Gateshki, and G. Cuello, Journal of Solid State Chemistry **182,** 1717 – 1725 (2009).

[6] M. T. Anderson, K. B. Greenwood, G. A. Taylor, and K. R. Poeppelmeier, Progress in Solid State Chemistry **22,** 197 – 233 (1993).

[7] O. K. Andersen and T. Saha-Dasgupta, Phys. Rev. B **62,** R16219–R16222 (2000).

[8] K. I. Kugel and D. I. Khoskii, Sov. Phys. JETP **37,** 725 (1973).

[9] K. I. Kugel and D. I. Khomskii, Soviet Physics Uspekhi **25,** 231 (1982).

[10] V. V. Mazurenko, F. Mila, and V. I. Anisimov, Phys. Rev. B **73,** 014418 (2006).

[11] H. Karunadasa, Q. Huang, B. G. Ueland, P. Schiffer, and R. J. Cava, Proceedings of the National Academy of Sciences **100,** 8097–8102 (2003).

[12] A. P. Ramirez, Annual Review of Materials Science **24,** 453–480 (1994).

[13] J. E. Greedan, J. Mater. Chem. **11,** 37–53 (2001).

[14] M. E. Lines, Proc. R. Soc. London **271,** 105 (1963).

[15] R. Moessner, Canadian Journal of Physics **79,** 1283–1294 (2001).

[16] M. E. Lines, Phys. Rev. **135,** A1336–A1346 (1964).

[17] R. Mishra, J. R. Soliz, P. M. Woodward, and W. Windl, Chemistry of Materials **24,** 2757–2763 (2012).

Chapter 6

Electronic Structure Study of $Hg_2Ru_2O_7$ in Comparison to $Tl_2Ru_2O_7$

6.1 Background

The 4d transition metal oxides, characterized by extended nature of the 4d orbitals, exhibit comparable energy scales of kinetic and coulomb energies which are competitive in nature. This drives the system at the verge of localized to itinerant behavior with a possibility of crossover from one to another depending on the details. In the present chapter we discuss this interesting issue in the context of ruthenate pyrochlores. Pyrochlore oxides are of interest because of their catalytic activity for a variety of processes and high temperature stability [1]. Many of the pyrochlore compounds like zirconate pyrochlores are important because of their potential use as high temperature gas sensors or fast ion conductors. Pyrochlore lattice naturally gives rise to geometric frustration and well known for providing spin-ice problem [2]. In this chapter we will focus on two pyrochlore ruthenates namely $Tl_2Ru_2O_7$ and $Hg_2Ru_2O_7$.

This chapter is based on *Phys. Rev. B 86, 125117 (2012)*

6.2 Introduction

Ruthenates in pyrochlore structure [Ref. [3]] of general formula $A_2B_2O_6O'$, e.g., $Tl_2Ru_2O_7$, $Bi_2Ru_2O_7$, or $Y_2Ru_2O_7$ [Ref. [4, 5, 6]] have been synthesized in which Ru ions are in Ru^{4+} oxidation state. There are other ruthenate pyrochlores like $Cd_2Ru_2O_7$, $Ca_2Ru_2O_7$ [Ref. [7, 8]] and recently synthesized $Hg_2Ru_2O_7$ [Ref. [9]], in which Ru ions are in the less common [Ref. [10]] highly oxidized state of Ru^{5+}. Among these compounds, $Tl_2Ru_2O_7$ (TRO) is reported [Ref. [11]] to exhibit a metal-insulator transition (MIT) at 120 K. The low temperature insulating phase of TRO has been interpreted [Ref. [12]] as an orbital ordering driven formation of one dimensional Haldane chain opening a spin gap suggesting the importance of correlation effect. The recently synthesized $Hg_2Ru_2O_7$ (HRO) has been also reported [13, 14] to exhibit a first order MIT at 107 K, similar to TRO. The apparent similarity in behavior of TRO and HRO is puzzling. While Ru^{4+} in TRO in low spin d^4 occupation of octahedral crystal field d states has orbital degrees of freedom left justifying the formation of orbital order driven formation of Haldane chain,[12] Ru^{5+} in HRO in low spin d^3 occupation has three t_{2g} electrons and should give rise to an S = 3/2 spin moment without any orbital degrees of freedom in the ionic limit. Local density approximation coupled with dynamical mean field theory (LDA+DMFT) calculation [15], carried out assuming a two channel model of HRO and ignoring the hybridization effect between Ru-O and Hg-O', showed signature of non-Fermi liquid behavior. The recent nuclear magnetic resonance (NMR) experiment [16] on HRO, on the other hand, reports observation of Ru-NMR signals at zero field at low temperature, providing evidence for an antiferromagnetic (AFM) order in the insulating phase, instead of the initial suggestion of formation of spin singlet states [14]. The NMR data adds onto further puzzle in the sense that the ordered moments are estimated to be about $1\mu_B$ per Ru, significantly smaller compared to the expected value of $3\mu_B$ for Ru^{5+} (S = 3/2). This leads to the question whether the observed behavior in HRO is driven by the same cause as in TRO, which relies on the

strongly correlated picture [13], and therefore assumes the localized character of Ru-d electrons. The situation is rather curious since it is the same Ru electrons in a similar structural environment that play the central role in both compounds. We investigate this issue employing first principles calculations.

6.3 Crystal Structure

In our study, we focused primarily on the high temperature phase. We shall be discussing some of the preliminary results on the low temperature phase at the end of the chapter. The high temperature phase of both TRO and HRO form in a cubic pyrochlore structure with space group $Fd\bar{3}m$ [9, 12]. The slightly larger ionic radius of Hg^{2+} compared to Tl^{3+} makes

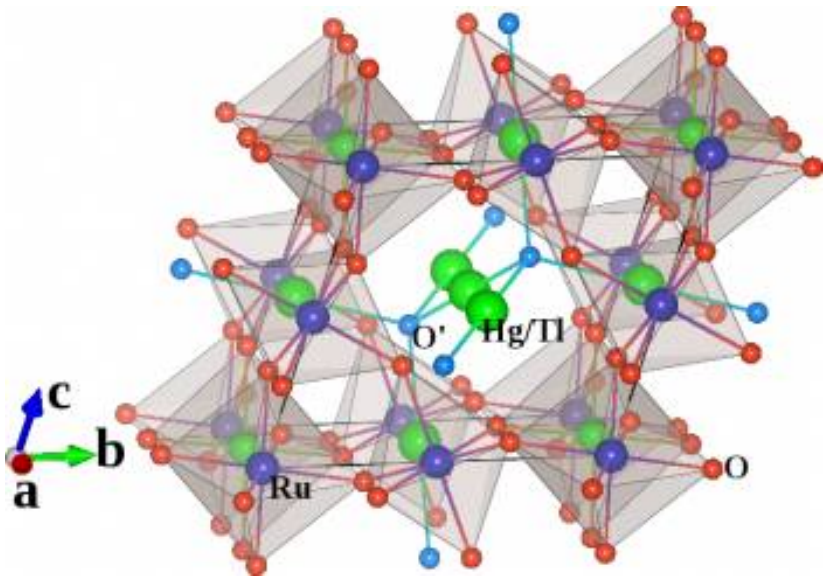

Figure 6.1 Primitive unit cell of cubic HRO (TRO). The Hg-O' (Tl-O') chain passes through the cage formed out of the connection of corner shared RuO_6 octahedra.

the lattice constant of HRO a bit larger (10.20 Å) compared to that of TRO (10.18 Å). The free parameter associated with x coordinate of O atoms is 0.317 (0.326) for HRO (TRO). The RuO_6 octahedra show trigonal distortion resulting in O-Ru-O deviating from 90° by δ. The

value of δ is 1.8° (5.2°) for HRO (TRO). The RuO_6 octahedra corner share with each other to give rise to a cage like structure through which the Tl/Hg-O' chain passes (cf. Fig. 6.1).

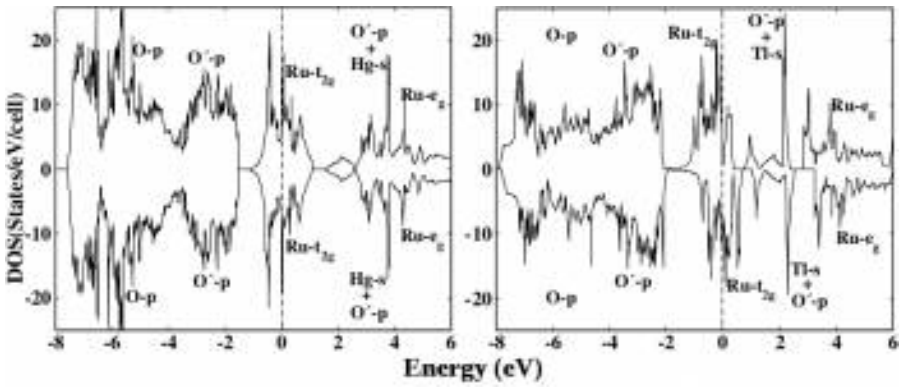

Figure 6.2 Spin-polarized GGA DOS for HRO (left) and TRO (right). The dominant contributions of various degrees of freedoms have been marked. The zero of the energy is set at E_F.

6.4 Basic Electronic Structure

To understand the comparison of basic electronic structure, the spin splitting, and the hybridization of different orbital degrees of freedom we carried out spin-polarized DFT calculations within GGA. The spin-polarized GGA density of states (DOS) is shown in Fig. 6.2. The Ru d-O/O' p hybridized band structure extends from an energy range 8 eV below Fermi energy (E_F) to about 6 eV above E_F. The states close to E_F are of predominant Ru-d character, while the states below -2 eV or so are dominantly of O and O'-p character. In accordance with low spin configuration of Ru, the octahedral crystal field split Ru-t_{2g} states form the low energy sates spanning the energy window from about -1 eV to 1 eV, Ru-e_g (e_g^σ) states being empty and situated at an energy position about 4 eV above E_F . Comparing the density of states of HRO and TRO, we find that the spin splitting of Ru-t_{2g} dominated states crossing E_F is much larger for TRO compared to that of HRO, although by simple counting of electrons, one

Table 6.1 Spin magnetic moments (in μ_B) calculated under GGA and GGA+U calculations, considering the FM as well as AFM (Ru: ↑, ↑, ↓, ↓) alignment of Ru spins

	HRO		**TRO**	
FM	GGA	GGA+U	GGA	GGA+U
Total Moment/Ru	0.13	1.79	1.45	2.00
Ru	0.11	1.23	1.03	1.49
O	0.02	0.19	0.10	0.12
O′	0.01	0.06	0.13	0.15
AFM	GGA	GGA+U	GGA	GGA+U
Total Moment/Ru	0.01	0.00	0.00	0.00
Ru	0.14	1.57	1.09	1.40
O	0.00	0.12	0.06	0.05
O′	0.00	0.00	0.00	0.00

would have expected the opposite. This is also reflected in the computed magnetic moment of 1.45 μ_B/Ru for TRO and a small moment of 0.13 μ_B/Ru for HRO. The moment at Ru site is found to be 1.03 μ_B for TRO and 0.11 μ_B for HRO with the rest of the moments sitting at the O site due to the covalency effect. Note that the rather small moment of Ru for HRO and an appreciable one for TRO happens irrespective of the chosen alignment of neighboring Ru spins. Considering the antiferromagnetic (AFM) arrangement with two of the Ru spins pointing up and two down, out of four Ru ions in the unit cell, one arrives at the same conclusion (as shown in Table 6.1).

In order to check the influence of the missing correlation in GGA, calculations were carried within GGA+U, with a choice of modest U values in conformity with the wide bandwidth of Ru-O hybridized bands. Calculations have been carried out varying U value between 1 and

3 eV and choices of both LMTO and plane wave basis. As discussed in Ref. [17], U_{dd} is expected to change by $\sim$1 eV per d electron change for the same element. The U value is expected not to be very different between Ru^{4+} and Ru^{5+}, since the charge occupancies for these two formal valence states are found not to differ by full one electron. Considering the DFT calculated Ru d occupancies of HRO (Ru^{5+}) and TRO (Ru^{4+}), we find the change in U value is as small as 0.2 eV. Repeating the calculation taking into account this change produces negligible effect. In order to keep the comparison between the two compounds direct, we kept the U value the same between TRO and HRO for a given set of calculations. The basic conclusions were found to remain unchanged irrespective of the choice of basis set and U values. The GGA+U density of states is shown in Fig. 6.3 for a choice of U = 2 eV and J_H = 0.8 eV. The inclusion of U increases the spin-splitting for both TRO and HRO, giving rise to a magnetic moment of $2.0\mu_B$ /Ru for TRO and $1.79\mu_B$ /Ru for HRO, with $1.49\mu_B$ and $1.23\mu_B$ of moments at Ru sites, respectively. Note that although the sizes of magnetic moments at Ru sites, $1.49\mu_B$ (TRO) and $1.23\mu_B$ (HRO), may sound comparable, they are $\sim$75% and $\sim$40% of the fully polarized moments of $2\mu_B$ and $3\mu_B$, respectively. Considering the calculated moments for AFM also, we find $50\%-60\%$ reduction of magnetic moment at Ru site compared to the fully localized ionic limit, for the Hg compound, in comparison to only $25\%-30\%$ reduction of magnetic moment at Ru site compared to the fully localized ionic limit, for the Tl compound.

In order to understand the significantly reduced magnetic moment compared to the ionic value in HRO as against TRO, we plot the Ru-t_{2g} density of states for HRO and TRO in the bottom panels of Fig. 6.3. The trigonal distortion present in RuO_6 octahedra for both HRO and TRO, in addition to octahedral crystal field splitting, further splits t_{2g} states into a singly degenerate a_{1g} state and doubly degenerate e_g^{π} states. We, therefore, project the Ru-t_{2g} density of states onto a_{1g} and e_g^{π} states. As is evident from the plots, e_g projected bandwidth is systemati-

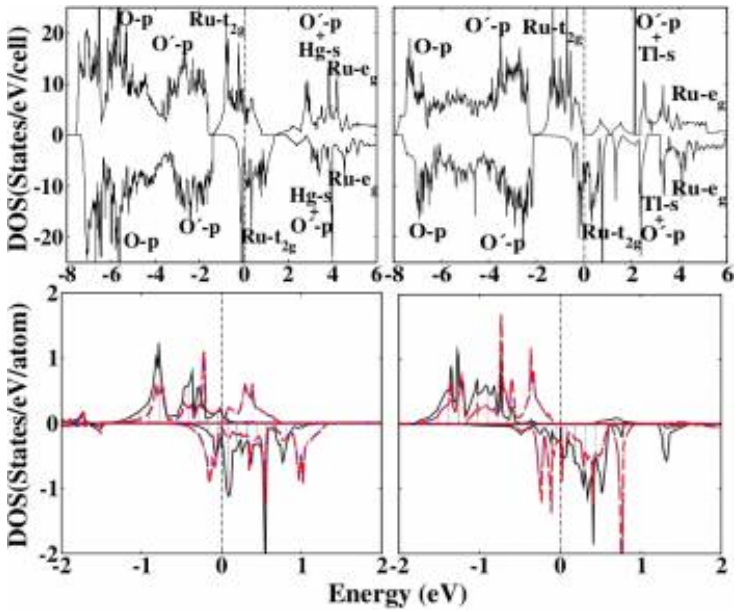

Figure 6.3 Top panels: GGA+U DOS for HRO (left) and TRO (right). Bottom panels: Ru-t_{2g} DOS for HRO (left) and TRO (right) projected onto a_{1g} (shaded area) and e_g^π (dashed lines). The zero of the energy is set at E_F.

cally larger than that of a_{1g} projected states by $0.3-0.4$ eV, which comes from the specific shape of the wave function associated with e_g compared to a_{1g} that allows for the increased hybridization with O-p for e_g . The individual a_{1g} and e_g^π bandwidths for HRO are larger than that of TRO by $0.3-0.4$ eV. To gain an understanding on this issue, we replot in Fig. 6.4 the schematic a_{1g} and e_g^π partial DOS for HRO and TRO as rectangular density of states, omitting the detail structure of the DOS and the small tailing, which makes the comparison of HRO and TRO more evident. Focusing on TRO, we find a_{1g} bandwidth ($W_{a_{1g}}$) ~ 1 eV and e_g^π bandwidth ($W_{e_g^\pi}$) ~ 1.4 eV. The spin splitting between the band centers is such that it makes a_{1g} band edges in majority and minority spin channels fall short of overlap, while the e_g^π majority and minority bands overlap over an energy window of only ≈ 0.5 eV. Moving to HRO, the increase of $0.3-0.4$ eV bandwidth of a_{1g} and e_g^π's makes both a_{1g} and e_g^π bands in majority and minority spin channel overlap, the overlap being substantial for e_g^π bands. Once the overlap between majority and minority spin channel bands happens, the electron flows from one

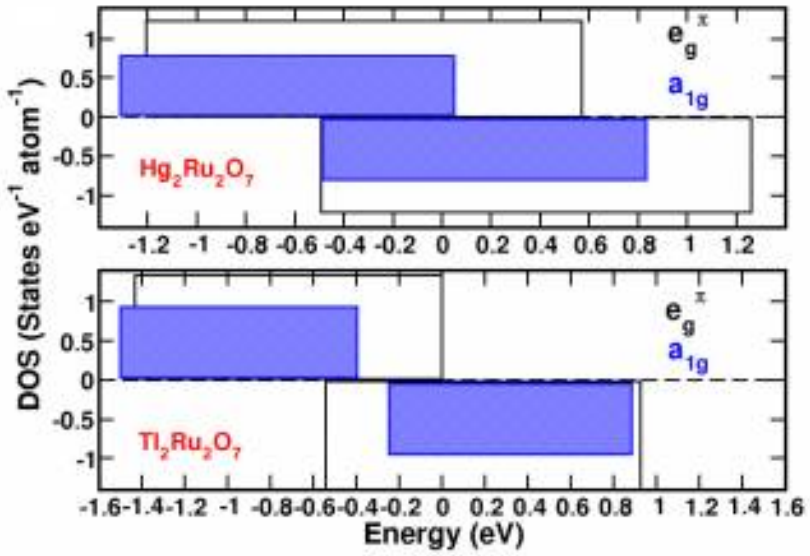

Figure 6.4 Schematic DOS corresponding to a_{1g} (shaded region) and e_g^π (unshaded region) states for HRO (top panel) and TRO (bottom panel).

spin channel to other, making the effective spin splitting further reduced. The above analysis is found to be true, considering Ru-t_{2g} projected partial DOS for other spin arrangements as well. We have also carried out GGA+U+spin-orbit (SO) calculations. The basic conclusion concerning the difference of TRO and HRO electronic structure is found to remain the same. The orbital moment at Ru site is found to be vanishingly small for HRO and that of TRO is found to $\approx 0.07\ \mu_B$. Nominal Tl^{3+} and Hg^{2+} valences lead to filled d-shell configurations with tiny orbital moment at Tl/Hg site. The analysis of the non-spin-polarized partial DOS shows a similar (0.3−0.4 eV) bandwidth expansion in HRO compared to TRO, indicating this to be driven by the change in the nature of the hybridization.

6.5 A-d Ru-d Hybridization

Since the lattice constant and Ru-O bond lengths and bond angles are rather similar between HRO and TRO compounds, one may expect the chemical effect of Hg versus that of Tl to play a role in the bandwidth expansion. In Fig. 6.5, we plot the Hg/Tl d- and s-projected DOS in comparison to that of O-p. We find a large shift (≈5 eV) in energy level position of Hg-5d in comparison to Tl-5d, which causes larger hybridization between Hg-5d and O-2p compared to that between Tl-5d and O-2p, which in turn hybridizes stronger with Ru-t_{2g}-O-p derived states. This is demonstrated nicely in the so-called fat band plots shown in insets of Fig. 6.5, where we projected out the Tl and Hg-d characters onto the manifold of Ru-t_{2g} bands, the fatness associated with each band being proportional to Tl or Hg-d characters. As is clearly seen, the weight, shown as fatness associated with the bands, is far more significant for Hg-d compared to Tl-d. While normally attention is focused onto empty s states of Hg or Tl [18], the above analysis shows that it is the mixing with d characters of Hg or Tl that plays the crucial role to decide the Ru-t_{2g} bandwidth difference between HRO and TRO.

In order to quantify the above discussed hybridization effect, we define the hybridization index, H_{dd} . We use two alternative approaches to define H_{dd} . In the first approach [19, 20], H^{I}_{dd} is defined as $\sum_i w^{A}_{i,d} w^{Ru}_{i,d}$, where $w^{A}_{i,d}$ and $w^{Ru}_{i,d}$ are the projections of i^{th} Kohn-Sham orbital at Γ point onto d spherical harmonic centered at Hg/Tl and Ru atoms, respectively, integrated over a sphere of specific radius. The summation in i runs over the energy range of the Ru-t_{2g} manifold. In the second approach, a k integrated estimate was obtained by defining $H^{II}_{dd} = \int \rho^{A}_{d}(\varepsilon)\rho^{Ru}_{d}(\varepsilon)d\varepsilon$, where ρ^{A}_{d} (ρ^{Ru}_{d}) is the projected d DOS on Hg/Tl (Ru) site and the energy integration is carried out over the energy range of Ru-t_{2g} manifold. Computations of H_{dd} have been carried out for both non-spin-polarized as well as spin-polarized calculations within GGA+U. The estimates for HRO and TRO were found as $H^{I}_{dd}|_{nonspin} = 0.02$ (TRO) and 0.10 (HRO), $H^{I}_{dd}|_{GGA+U} = 0.01$ (TRO) and 0.30 (HRO), $H^{II}_{dd}|_{nonspin} = 0.03$ (TRO) and

0.18 (HRO), and $H_{dd}^{II}|_{GGA+U} = 0.03$ (TRO) and 0.25 (HRO). Irrespective of the definition, and spin-polarized or non-spin-polarized calculations, HRO shows A-d−Ru-d hybridization which is about an order of magnitude larger compared to that of TRO. This change in the extent of A-Ru hybridization causes the 0.3−0.4 eV increase in Ru-t_{2g} bandwidth for HRO compared to TRO, which is of the order of inherent spin splitting of Ru.

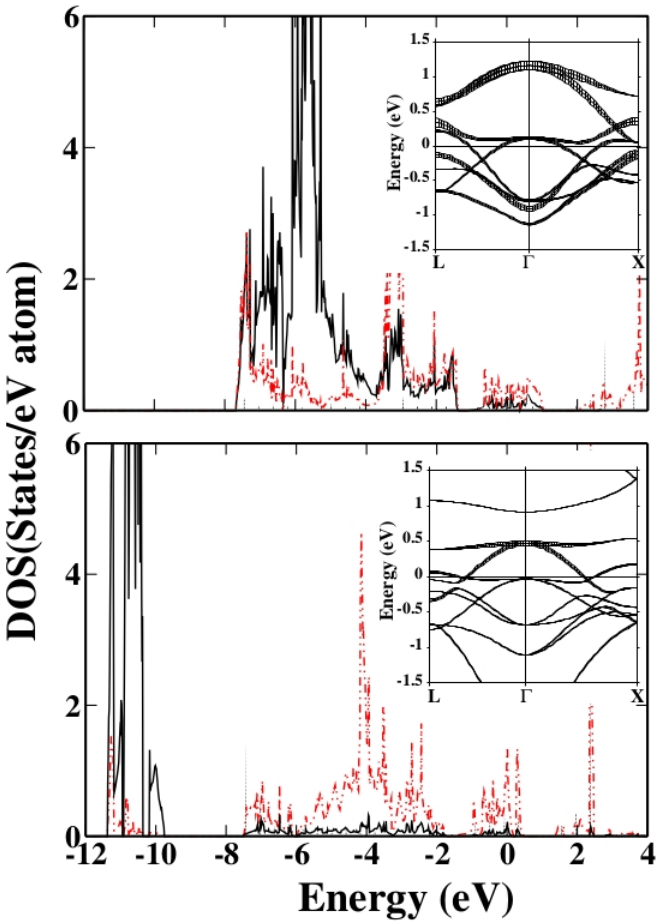

Figure 6.5 Non-spin-polarized DOS projected onto Hg/Tl-d (solid line), Hg/Tl-s (shaded region), and O'-p (dashed line) for HRO (upper panel) and TRO (lower panel). Insets: projection of Hg/Tl-d character (marked by fatness) in Ru-t_{2g} bands.

6.6 Wannier Function and Localizattion Properties

In order to probe the localization properties of electrons, attempts have been made based on constraint total energy calculations in the context of f -electron systems, as in Ref. [21] and in the context of d-electron systems, as in Ref. [22]. Since the Ru-d electrons are expected to be on the borderline of localized and itinerant character, here we followed an alternative approach. We carried out NMTO-downfolding calculation to construct effective Ru-a_{1g} and e_g^{π} Wannier functions. In the NMTO-downfolding calculation, starting from a non-spin-polarized self-consistent GGA calculation, all the degrees of freedom other than Ru-t_{2g}'s have been integrated out to construct a Ru t_{2g} only low-energy Hamiltonian. This leads to construction of Wannier functions, which span only the Ru-t_{2g} projected bands and nothing else. The constructed Wannier functions have a central part that is shaped according to a_{1g} or e_g^{π} symmetries, while the tails are shaped according to integrated out degrees of freedom, namely O-p, O'-p, and Hg/Tl degrees of freedom as shown in Fig. 6.6, for $e_g^{\pi,2}$. We find that while the constructed Wannier functions have a central part that is shaped according to e_g^{π} symmetry and the predominant tails are of p character sitting at O sites, there are finite weights at O' and Hg/Tl sites of the Hg/Tl-O' chains surrounding the RuO_6 central octahedra. This indicates finite mixing between A-O' and Ru-O degrees of freedom, a fact which has been stressed also in literature [23, 24] and has been neglected in the LDA+DMFT treatment of HRO [15]. We further find the weight sitting at Hg or Tl site is of Hg/Tl d character mixed with s character and the weight at Hg is much stronger compared to that at Tl (encircled region in the Wannier function plots in Fig. 6.6). To underline the different extent of spatial extents of the two wave functions, we also plot the difference between the two $e_g^{\pi,2}$ Wannier functions of HRO and TRO in the bottom panel. While the differences are seen for weights sitting at Ru and O sites, the difference weight sitting at the A site is appreciable, which dictates the range of the Wannier function.

To put the above observations in quantitative footing, we calculated the spreads of the

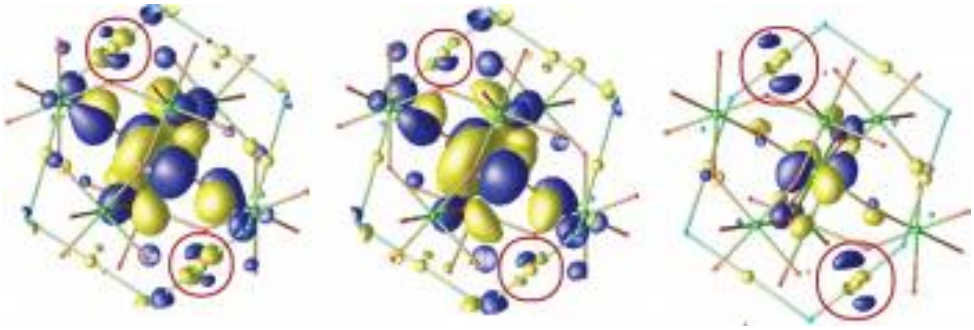

Figure 6.6 Effective Ru-$e_g^{\pi,2}$ Wannier functions for HRO (left panel), TRO (middle panel), and their difference (rightmost panel) obtained from the NMTO-downfolding calculation. The lobes of opposite signs are colored as blue (dark gray) and yellow (light gray). The weights sitting at A sites have been encircled.

Ru-t_{2g} Wannier functions for HRO and TRO, as defined in [Ref. [25]] $\langle r^2\rangle_n - \langle r\rangle_n^2$, where $\langle r\rangle_n = \langle 0n|\overrightarrow{r}|0n\rangle$ and $\langle r^2\rangle_n = \langle 0n|r^2|0n\rangle$, $|Rn\rangle$ being the Wannier function in cell R for nth (a_{1g}, $e_g^{\pi,1}$, and $e_g^{\pi,2}$) orbital. The spread provides the measure of the localization properties of a given wave function. The calculated spreads for a_{1g}, $e_g^{\pi,1}$, and $e_g^{\pi,2}$, for HRO, were obtained as 3.52 Å^2, 3.61 Å^2, and 3.65 Å^2, respectively, which were about 30%−35% larger than the spreads obtained from TRO (2.45 Å^2, 2.34 Å^2, and 2.38 Å^2, respectively). This, in turn, establishes the relatively delocalized character of Ru-d states in HRO, compared to that of TRO, and validates the observation of significant reduction of Ru moment for HRO compound compared to TRO. The magnetism is associated with the localized character and is maximum at isolated atomic limit.

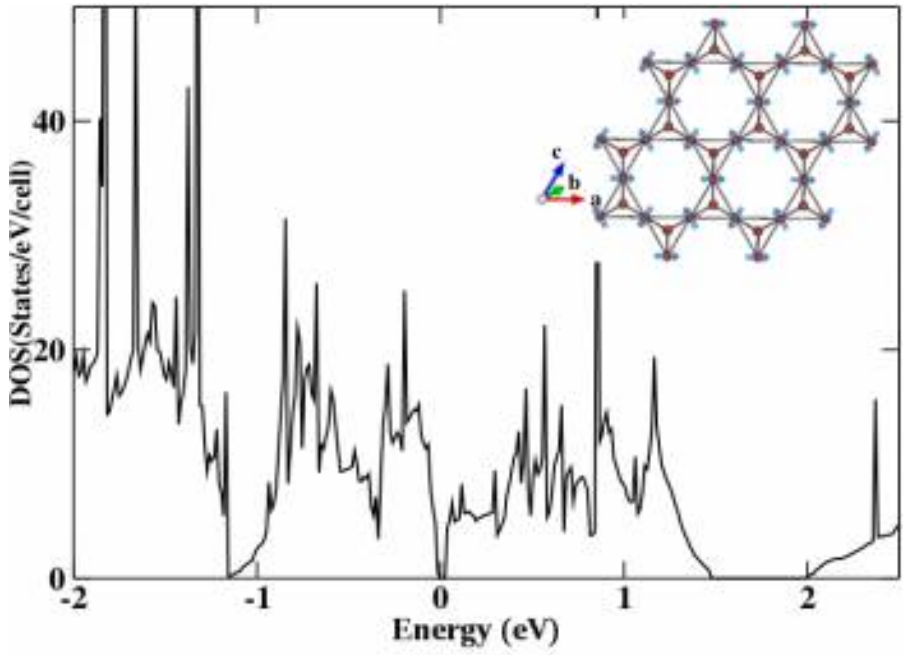

Figure 6.7 GGA+U density of states, corresponding to Conf.c (see text for details). The inset shows the arrangements of Ru spins corresponding to Conf.c, shown in the kagome layer of the Ru pyrochlore lattice.

6.7 Total Energy Calculations and Magnetic Structure of HRO

As is seen from Figs. 6.2 and 6.3, the spin-polarized DFT calculation gives rise to a metallic solution for HRO in both GGA as well as GGA+U calculation. The relatively delocalized nature of Ru-d orbitals in HRO makes the scenario of formation of spin singlets, as in case of TRO [12], less plausible. The behavior of magnetic susceptibility below T_{MIT}, alternatively, can be interpreted as development of AFM long range order [9], as proposed in Ref. [16]. AFM interaction defined on Ru sublattice being frustrated, one may imagine this to give rise to noncollinearity. The NMR study [16] predicted possible noncollinear magnetic structures which are compatible with the NMR data. We have calculated total energies within GGA+U considering the collinear FM, AFM, and FIM arrangement of Ru spins within a Ru_4 tetrahe-

Table 6.2 Total energies for different magnetic configurations of Ru spins in HRO. Total energies (ΔE) are measured with respect to the ferromagnetic (FM) configuration. The other configurations considered are AFM, ferrimagnetic (FIM), and two noncollinear configurations [Conf.b and Conf.c suggested in Figs. 7(b) and 7(c) of Ref. [16], respectively].

	1	2	3	4	5	ΔE (meV/Ru)
					HRO	TRO
FM	+	+	+	+	0	0
AFM	-	+	+	-	-90	-50
FIM	-	+	-	-	-70	-37
Conf.b					-66	-40
Conf.c					-100	-45

dra, together with possible noncollinear magnetic structures suggested based on NMR data in Ref. [16]. The results are summarized in Table 6.2.

As is evident from the total energies listed in Table 6.2, the noncollinear configuration (referred to as Conf.c), shown in the inset of Fig. 6.7, turned out to be the lowest energy magnetic structure. The GGA+U density of states corresponding to the lowest energy magnetic structure is plotted in Fig. 6.7. The obtained magnetic moments are found to be 1.51 μ_B, 0.07 μ_B, and 0.0 μ_B at Ru, O, and O' sites, respectively, in good agreement with the values obtained for collinear spin arrangements (cf. Table 6.1). The realization of the lowest energy magnetic structure opens up a gap of 0.1 eV. The precise magnitude of gap, of course, depends on the applied U value. The development of long range magnetic order is, therefore, capable of driving the insulating solution. The lowering of crystal symmetry has been indicated in experimental results [16], which may even help increase the gap value. The possible symmetries

Table 6.3 The lattice coordinates and the relaxed ionic positions of trigonal phase structure of HRO.

Space group: R$\bar{3}$m, a=7.1892 Å, c=17.6381 Å		
Atoms	Multiplicity	X Y Z
Hg1	3	0.5 0.0 0.0
Hg2	1	0.0 0.0 0.5
Ru1	3	0.5 0.0 0.5
Ru2	1	0 0 0
O1	2	0.0000 0.0000 0.3743
O2	6	-0.128329 0.128329 0.06119
O3	6	0.13075 -0.13075 0.19263

of the low temperature structure has recently been discussed in the literature, which will be taken up in the following section.

6.8 Low Temperature Phase

Experimental study [Ref. [26]] indicates lowering of crystal symmetry from cubic to some other upon lowering temperature. Recently, Ref. [27] suggested many possible low symmetry structures for $Hg_2Ru_2O_7$ - cubic (Fd$\bar{3}$m), orthorhombic (Imma), and monoclinic (C2/m). The authors concluded the monoclinic structure to be the low temperature phase for $Hg_2Ru_2O_7$. Study carried by group of Takagi et. al. [Ref. [28]] indicated stabilization of trigonal symmetry (R$\bar{3}$m). Starting from the experimental crystal structures, we relaxed atomic positions considering the low symmetry structures of monoclinic as well as trigonal symmetry keeping the lattice parameters as measured experimentally. The lattice parameters and relaxed ionic position coordinates of trigonal phase are given in the Table 6.3 and Table 6.4. The equiv-

Table 6.4 The inequivalent sites with Wyckoff positions for both monoclinic and trigonal phase (for a primitive cell) are given in the table.

Space group: C2/m			Space group: R$\bar{3}$m		
Atoms	Multiplicity	Wyckoff	Atoms	Multiplicity	Wyckoff
Hg1	2	f	Hg1	3	e
Hg2	1	d	Hg2	1	b
Hg3	1	b	Ru1	3	d
Ru1	2	e	Ru2	1	a
Ru2	1	a	O1	2	c
Ru3	1	c	O2	6	h
O1	4	j	O3	6	h
O2	4	j			
O3	2	i			
O4	2	i			
O5	2	i			

alent Hg and Ru positions in high temperature phase split into the ratio 2:1:1 in monolcinic symmetry and in the ratio 3:1 in trigonal symmetry.

There are three inequivalent Ru ions labeled as Ru1, Ru2 and Ru3 in monolinic phase while two inequivalent Ru ions labeled as Ru1 and Ru2. Crystal structure analysis carried on experimentally measured structures, before optimization, shows no volume difference between the $Ru1O_6$, $Ru2O_6$, and $Ru3O_6$ octahedra in monolcinic phase and a large volume difference between $Ru1O_6$ and $Ru2O_6$ of the order of 1.124 $Å^3$ in trigonal symmetry. After optimization in monoclinic phase the volumes of the $Ru1O_6$ and $Ru2O_6$ octahedra become

Table 6.5 The total energy values of optimized structures calculated under GGA+U approximation with the spin-polarized situation where three Ru spins are opposite to the fourth Ru are given with respect to the energy value of high temperature cubic phase ($Fd\bar{3}m$) structure.

Cubic phase ($Fd\bar{3}m$)	Monoclinic phase (C2/m)	Trigonal Phase ($R\bar{3}m$)
0	0.668	-0.101

equal with a volume difference ~ 0.09 Å^3 between $Ru3O_6$ and $Ru1O_6$/$Ru2O_6$ as shown in Fig. 6.8. Very interestingly after ionic relaxation the difference in octahedral volume in monoclinic phase is found to be comparable to that found in optimized trigonal phase. The octahedral volume difference in trigonal phase after optimization is found to be ~ 0.1 Å^3.

The analysis of the optimized structures of two different possible symmetries in low temperature provides evidence of presence of RuO_6 octahedra with different volumes. The results of the T=0 K energy calculations of the optimized structures in the low temperature phase compared with that of high temperature cubic phase is shown in the Table 6.5. It shows trigonal symmtery is preferred as the symmetry of the ground state structure in the low temperature phase of $Hg_2Ru_2O_7$ which is lower in energy compared to the cubic phase which is the high temperature phase. In the following we therefore discuss the electronic structure of $Hg_2Ru_2O_7$ assuming trigonal symmetry of the crystal structure.

Study of the electronic density of states of Ru ions in optimized structure of the trigonal phase, indicates the electronic structure of Ru1 and Ru2 d states to be different, as shown in Fig. 6.9. The density of states are calculated under GGA+U approximation with U(Ru) = 3 eV and J_H = 0.8 eV (cf. Fig. 6.9). The differential electronic structure of Ru1 and Ru2 is anticipated from the difference in volume of $Ru1O_6$ and $Ru2O_6$ octahedra. The magnetic moments at Ru1 and Ru2 are found to be oppositely aligned with moments 1.90 μ_B and -1.63 μ_B.

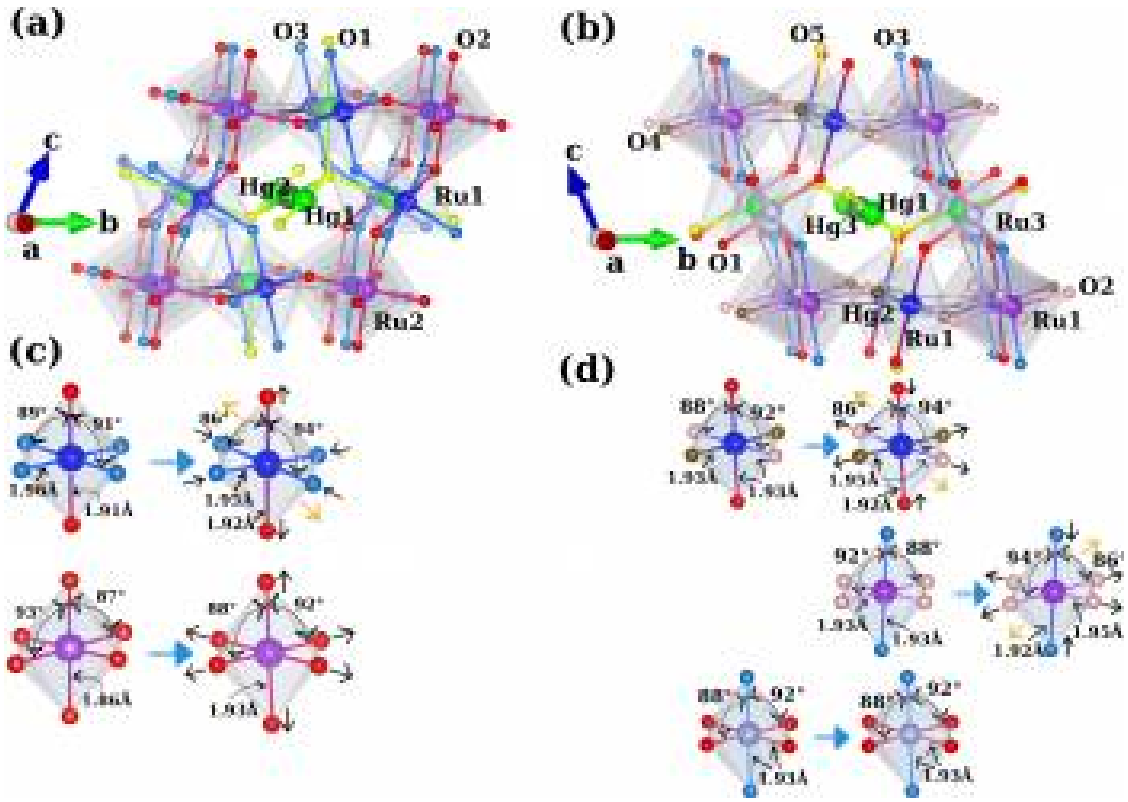

Figure 6.8 (a) The trigonal unit cell ($R\bar{3}m$) for HRO (low temperature) with the ions labeled in the figure. (b) The monoclinic unit cell (C2/m) of HRO (low temperature) with ions labeled in the figure. (c) The left panel shows $Ru1O_6$ and $Ru2O_6$ octahedra of trigonal phase before optimization and right panel shows octahedra after optimization. Before optimization the volume of octahedra $Ru1O_6$ is ~ 9.70 Å^3 and of octahedra $Ru2O_6$ ~ 8.58 Å^3 and after optimization volume of octahedra $Ru1O_6$ is ~ 9.65 Å^3 and of octahedra $Ru2O_6$ is ~ 9.55 Å^3.(d) The left panel shows $Ru1O_6$, $Ru2O_6$ and $Ru3O_6$ octahedra of monoclinic phase before optimization and right panel shows octahedra after optimization. The volume of octahedra $Ru1O_6$, $Ru2O_6$, $Ru3O_6$ before optimization are same ~ 9.54 Å^3 and after optimization volume of octahedra $Ru1O_6$, $Ru2O_6$ (now JT distorted) ~ 9.68 Å^3 and of octahedra $Ru3O_6$ is ~ 9.60 Å^3. The black arrows show the increase and decrease of Ru-O bond lengths due to optimization and yellow arrow show the direction of distortion of the octahedra due to change in bond length.

The difference in magnetic moment values as well as the electronic structure points towards charge disproportionate situation between Ru1 and Ru2. The charge transfer between Ru1 and Ru2 is evident from the energy level diagram of Ru 4d levels calculated using NMTO-

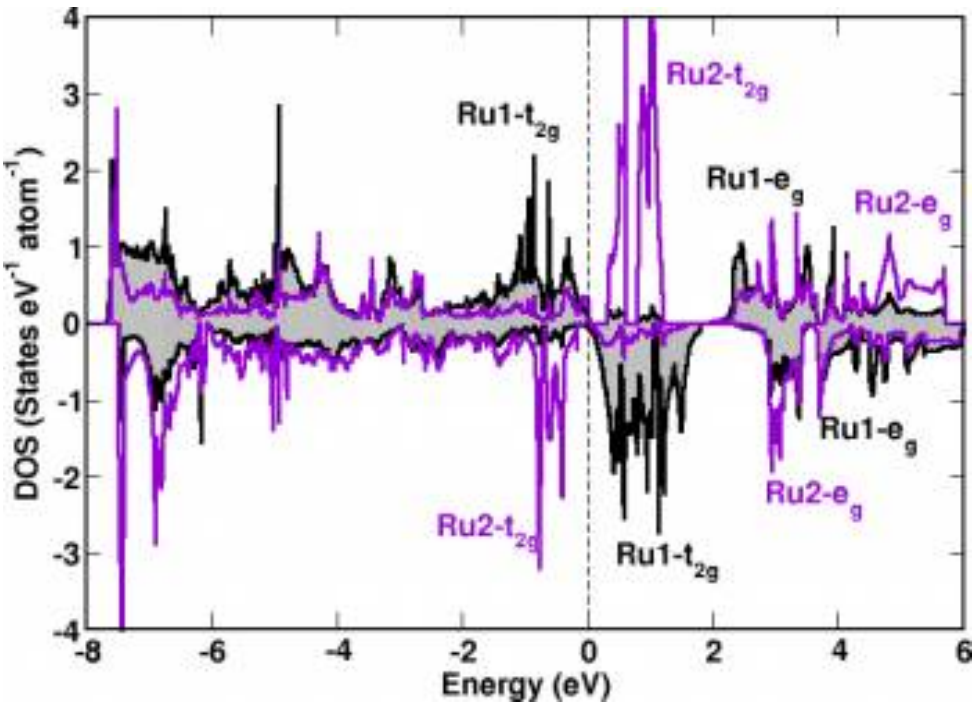

Figure 6.9 Electronic density of states for Ru1 4d states (black shaded region) and for Ru2 4d states (violet colored line) exhibits completely different electronic structure for Ru1 and Ru2 ions indicating the charge disproportionate situation.

downfolding method as shown in Fig. 6.10. From the energy level diagram shown in Fig. 6.10 clearly shows the charge flow from Ru2 to Ru1 d level which confirms the charge disproportionation between Ru1 and Ru2. Further calculations are in progress to have a complete understanding of the low temperature electronic structure [29].

6.9 Conclusion

In conclusion, we have carried out first principles study to investigate the electronic structure of pyrochlore ruthenate HRO in comparison to that of TRO. Our study shows that Ru-d orbitals are much more delocalized for HRO compared to TRO. This indicates that the strongly

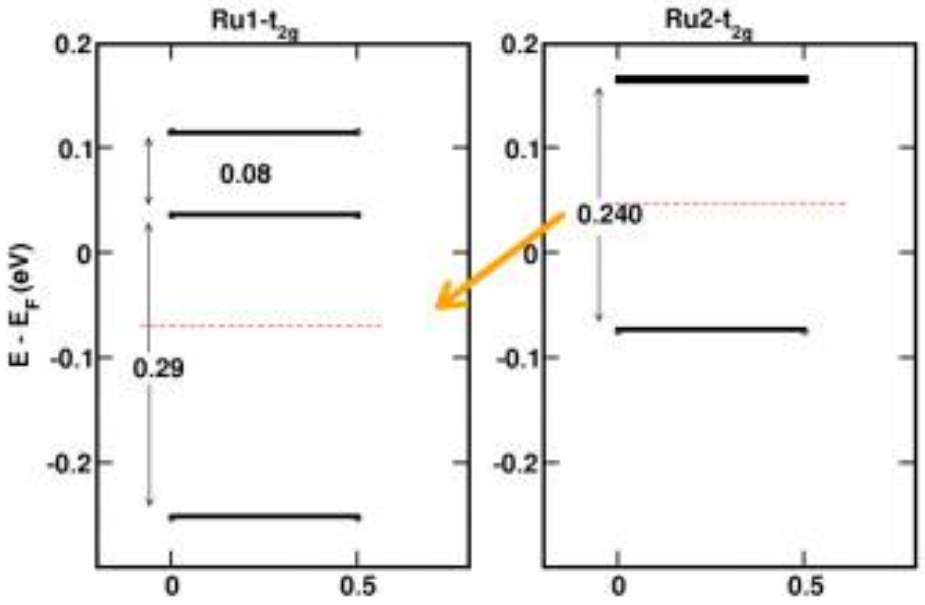

Figure 6.10 The energy levels corresponding to Ru1-t_{2g} state (left panel) and Ru2-t_{2g} state (right panel) are shown here. The red dotted line represents the center of gravity of t_{2g} band. The yellow arrow represents the charge flow from Ru2 site to Ru2 site indicating charge disproportionate situation.

correlated electron picture may not be an appropriate one for HRO. The long range antiferromagnetic order is found to be sufficient to drive the insulating state for HRO, as opposed to formation of a singlet ground state in TRO [12]. This interesting evolution in moving from TRO to HRO happens as Ru-4d states lie at the verge of localized to itinerant character. A modest increase of bandwidth in the case of HRO due to enhanced covalency between Ru-4d and Hg-5d compared to that between Ru-4d and Tl-5d causes Ru-4d electrons in HRO to attend much more itinerant character compared to that in TRO. Considering the probable low temperature crystal structures we find signature of charge disproportionated situation. Our findings justify the results of the NMR experiment [16] carried out on HRO.

Bibliography

[1] M. Subramanian, G. Aravamudan, and G. S. Rao, Progress in Solid State Chemistry **15,** 55 – 143 (1983).

[2] S. T. Bramwell and M. J. P. Gingras, Science **294,** 1495–1501 (2001).

[3] J. S. Gardner, M. J. P. Gingras, and J. E. Greedan, Rev. Mod. Phys. **82,** 53–107 (2010).

[4] T. Takeda, M. Nagata, H. Kobayashi, R. Kanno, Y. Kawamoto, M. Takano, T. Kamiyama, F. Izumi, and A. Sleight, Journal of Solid State Chemistry **140,** 182 – 193 (1998).

[5] F. Ishii and T. Oguchi, Journal of the Physical Society of Japan **69,** 526–531 (2000).

[6] M. Subramanian, G. Aravamudan, and G. S. Rao, Progress in Solid State Chemistry **15,** 55 – 143 (1983).

[7] R. Wang and A. Sleight, Materials Research Bulletin **33,** 1005 – 1007 (1998).

[8] T. Munenaka and H. Sato, Journal of the Physical Society of Japan **75,** 103801 (2006).

[9] W. Klein, R. K. Kremer, and M. Jansen, J. Mater. Chem. **17,** 1356–1360 (2007).

[10] U. Manju, V. P. S. Awana, H. Kishan, and D. D. Sarma, Phys. Rev. B **74,** 245106 (2006).

[11] H. Sakai, M. Kato, K. Yoshimura, and K. Kosuge, Journal of the Physical Society of Japan **71,** 422–424 (2002).

[12] S. Lee *et al.*, Nat. Mater. **5,** 471–476 (2006).

[13] N. Takeshita, C. Terakura, Y. Tokura, A. Yamamoto, and H. Takagi, Journal of the Physical Society of Japan **76,** 063707 (2007).

[14] A. Yamamoto, P. A. Sharma, Y. Okamoto, A. Nakao, H. Aruga Katori, S. Niitaka, D. Hashizume, and H. Takagi, Journal of the Physical Society of Japan **76,** 043703 (2007).

[15] L. Craco, M. S. Laad, S. Leoni, and H. Rosner, Phys. Rev. B **79,** 075125 (2009).

[16] M. Yoshida, M. Takigawa, A. Yamamoto, and H. Takagi, Journal of the Physical Society of Japan **80,** 034705 (2011).

[17] T. Bandyopadhyay and D. D. Sarma, Phys. Rev. B **39,** 3517–3521 (1989).

[18] J. Okamoto, T. Mizokawa, A. Fujimori, T. Takeda, R. Kanno, F. Ishii, and T. Oguchi, Phys. Rev. B **69,** 035115 (2004).

[19] H. Häkkinen, M. Moseler, and U. Landman, Phys. Rev. Lett. **89,** 033401 (2002).

[20] H. Häkkinen, B. Yoon, U. Landman, X. Li, H.-J. Zhai, and L.-S. Wang, The Journal of Physical Chemistry A **107,** 6168–6175 (2003).

[21] O. Eriksson, J. Becker, A. Balatsky, and J. Wills, Journal of Alloys and Compounds **287,** 1 – 5 (1999).

[22] L. Petit, G. M. Stocks, T. Egami, Z. Szotek, and W. M. Temmerman, Phys. Rev. Lett. **97,** 146405 (2006).

[23] T. Saha-Dasgupta, M. De Raychaudhury, and D. D. Sarma, Phys. Rev. Lett. **96,** 087205 (2006).

[24] D. J. Singh, Phys. Rev. B **55,** 313–316 (1997).

[25] N. Marzari and D. Vanderbilt, Phys. Rev. B **56,** 12847–12865 (1997).

[26] M. Yoshida, M. Takigawa, A. Yamamoto, and H. Takagi, Journal of the Physical Society of Japan **80,** 034705 (2011).

[27] J. van Duijn, R. Ruiz-Bustos, and A. Daoud-Aladine, Phys. Rev. B **86,** 214111 (2012).

[28] H. Takagi et. al., Unpublished .

[29] S. Baidya and T. Saha-Dasgupta, unpublished .